THE ANISOTROPIC MICROWAVE ELECTRODYNAMICS OF YBCO

by

AHMAD REZA HOSSEINI-GHEINANI

B.Sc., University of Toronto, 1995
M.Sc., University of British Columbia, 1997

A THESIS SUBMITTED IN PARTIAL FULFILMENT OF
THE REQUIREMENTS FOR THE DEGREE OF

DOCTOR OF PHILOSOPHY

in

The Faculty of Graduate Studies

(Department of Physics and Astronomy)

We accept this thesis as conforming
to the required standard

THE UNIVERSITY OF BRITISH COLUMBIA

December 13, 2002

In presenting this thesis in partial fulfilment of the requirements for an advanced degree at the University of British Columbia, I agree that the Library shall make it freely available for reference and study. I further agree that permission for extensive copying of this thesis for scholarly purposes may be granted by the head of my department or by his or her representatives. It is understood that copying or publication of this thesis for financial gain shall not be allowed without my written permission.

Department of Physics and Astronomy

The University Of British Columbia
Vancouver, Canada

Date December 16, 2002

Abstract

The anisotropic microwave surface impedance of the high temperature superconductor, $YBa_2Cu_3O_{7-\delta}$, has been investigated. Microwave spectroscopy using five microwave cavities has been used to show clearly the development of long lived quasiparticles (QP) in the *ab*-plane of $YBa_2Cu_3O_{6.99}$. Two regimes of transport are found, one below 20 K where the quasiparticle (QP) dynamics is with residual impurities, and above 20 K where umklapp QP-QP interactions dictate the temperature dependence of the transport lifetimes.

The $\hat{c}$-axis microwave surface impedance of $YBa_2Cu_3O_{6.95}$ has been studied into the superconducting state. The long QP lifetimes found in the planes of this material are found to be absent in the conductivity observed along the $\hat{c}$-axis, indicating that the confinement of carriers to the planes is an inherent feature of the cuprates. The highly underdoped superconducting state has also been investigated with microwave techniques. The temperature dependence of the $\hat{c}$-axis superfluid stiffness is found to scale over a range of hole dopings, corresponding to T_c's in the range 9-19 K. We further find that the magnitude of the zero temperature $\hat{c}$-axis superfluid stiffness grows rapidly with doping, initially as fast as T_c^2.

Contents

List of Figures

Acknowledgements

First I would like to thank my research advisor, Professor Doug Bonn, for giving me the opportunity to be a student in his group and grow over the years as a researcher. Without his patience and advice, this project would have not been possible. I would like to thank also Professor Walter Hardy who has been like a co-advisor throughout my education at UBC. He has never failed to inspire me with his deep insight and unique way of doing physics. I would also like to thank Dr Ruixing Liang who contributed greatly to this project with his hard work preparing good quality YBCO crystals for our group to study.

Without the students and postdocs over the years, this work would have not taken place. I have greatly benefited from two individuals whom deserve special mention. First I would like to thank Saeid Kamal for being a great colleague, and helping me understand the intricate details of microwave experiments. Special thanks are also due to Dr David Broun whose suggestions and insight into physics have helped me substantially during the course of my escapades in the UBC superconductivity group. I would also like to thank my present and past friends in the lab, Chris Bidinosti, Jennifer Babiak, Tami Pereg-Barnea, Pinder Dosanjh, Richard Harris, Darren Peets, Patrick Turner, Andre Wong, Geoff Mullins, Robert Knobel, Bruce Gowe, and Marty Kurylowicz, all of whom have made the workplace enjoyable over the years.

I would like to thank my parents, sisters and brother for being there for me at all times. Also I'd like to thank Salah ElHoss, Shiva Mojtabavi, Ziba Bozorgzadeh, and Veronica Cabral for their friendships and support.

Finally I would like to thank the Natural Sciences and Engineering Research Coun-

cil of Canada, the Department of Physics and Astronomy, and the UBC Graduate fellowship program for providing support for this project.

Chapter 1

Introduction

The quest to understand highly correlated electron systems has acquired a new meaning since the discovery of the cuprate superconductors by Bednorz and Muller in 1986 [1]. These materials are the epitome of strong correlation, and continue to challenge experimenters and theoreticians alike with the variety of phenomena found across their phase diagram. These take on the form of insulating, antiferromagnetic, and superconducting order among others which can be present depending on the doping level of the materials.

The high temperature superconductors are also highly two dimensional, with CuO_2 planes being the only common structural feature. The physics leading to superconductivity is believed to be taking place in these planes, with the other structural components separating them functioning either as spacers or as charge reservoirs that regulate the charge density on the planes. Despite the importance of the planes, it is also generally accepted that a strictly two dimensional system cannot sustain long range order at finite temperature, and some level of coupling in the third dimension is necessary to suppress superconducting fluctuations in two dimensions. In light of this, studies of the $\hat{c}$-axis are important in the quest to understand the physics of these materials.

The low dimensionality of these systems has also been taken by several theorists as a prerequisite for the high critical temperatures observed [2]. Central to this point of view again has been the nature of interlayer coupling, and charge transport out of the copper oxygen planes. Efforts to study this have mainly been limited to materials which can be prepared with large faces containing the $\hat{c}$-axis, or to DC transport mea-

surements which are limited to the normal state. However, finite frequency studies are not limited to the normal state, and have long been used to study the superconducting state of elemental superconductors [3, 4, 5]. A simplifying feature of the high temperature superconductors is that their response to applied electromagnetic fields is usually local, and a measure of the microwave surface impedance is a direct measure of two important properties of the superconducting state: the superfluid density and the low energy excitations out of the condensate. In recent times, microwave measurements of the in-plane superfluid density have provided some of the earliest evidence for an unconventional ground state in the cuprates [6].

In this thesis, we have adopted these methods to study the anisotropic transport properties of Yttrium Barium Copper Oxide (YBCO), both parallel and perpendicular to the copper oxygen planes. The measurements were performed on two generations of YBCO crystals. The crystals chosen for measurement have typically been very small, and for some measurements the samples have been reshaped by cutting and polishing. The experimental challenges encountered have been numerous but successfully overcome to obtain a detailed picture of the anisotropic electrodynamics of YBCO.

1.1 Electrodynamic Properties of Superconductors

The superconducting state is characterized by the complete absence of DC electrical resistance. It was thought in the early days that this property defined a superconductor. In 1932 Keeson and Kok observed a discontinuity in the electronic heat capacity of tin [7], to be followed by the work of Meissner and Oschsenfeld [8] which showed that the superconducting state exhibited reversible field exclusion, a phenomenon not expected in a perfect conductor. These two experiments revealed that the superconducting state involves a reordering of electrons into a new quantum mechanical

ground state.

The loss of resistance and the Meissner effect were first united in a phenomenological picture by the brothers, Fritz and Heinz London [9]. Their model proposed the existence of superconducting carriers, with density n_s, whose electromagnetic response is governed by the London equation,

$$\frac{\partial \vec{J}_s}{\partial t} = \frac{n_s e^2}{m^*}\vec{E} \tag{1.1}$$

where e and m^* are the charge and effective mass of the superconducting electrons. It also implies that superconducting carriers respond to an electric field in the same way as Drude free electrons, but with an infinitely long relaxation time. Combined with Maxwell's relations, Eq. 1.1 also implies a frequency independent skin depth, the London Penetration depth,

$$\lambda_L = \left(\frac{m^*}{\mu_0 n_s e^2}\right)^{1/2}. \tag{1.2}$$

λ_L in superconducting metals is of order of microns or less, such that effectively, the magnetic field is completely excluded from a large bulk sample.

1.2 Generalized Two Fluid Model

The generalized two fluid model builds on the London model, leading to a good phenomenological description of the high frequency electrodynamics of superconductors[1], and serves as a good starting point in the interpretation of experiments. The basic assumption is that the electromagnetic response of a superconductor can be divided into two components, that due to normal and to superconducting electron densities n_n and n_s respectively.

If we take harmonic time variations for the fields, i.e $e^{i\omega t}$, Eq. 1.1 can be written

[1]Strictly speaking, the two fluid model is most easily justified in the clean limit where the quasiparticle spectrum has its spectral weight well below the superconducting gap frequency.

as,

$$\vec{J}_s = -\frac{in_s e^2}{m^* \omega}\vec{E} \tag{1.3}$$

and the quantity $-in_s e^2/m^*\omega$ can be identified as an imaginary conductivity due to the inertial response of the superfluid. At DC, the superfluid response can screen all the normal fluid, and there is infinite conductivity. However, at finite frequency the superfluid, which has finite inertia, is unable to oscillate perfectly in phase with the alternating field, and it will not screen the normal fluid perfectly. This means that the normal fluid will also conduct in parallel and give rise to a complex conductivity, σ_n. The electromagnetic response functions, being causal, must obey the Kramers Kronig relations. The superfluid conductivity will then have to have a real part given by a delta function at zero frequency. The total conductivity for a superconductor can then be written as

$$\sigma(\omega) = \frac{\pi n_s e^2}{m^*}\delta(\omega) - \frac{in_s e^2}{m^*\omega} + \sigma_n(\omega) \tag{1.4}$$

This has been derived quite generally, with the only assumption being that the current-field relations are local. Non-local effects become important when the correlation lengths in the system exceed the characteristic length for the penetration of electromagnetic fields into the sample. In the cuprates, the in-plane penetration depth is typically 1000 to 2000 Å. Along the $\hat{c}$-axis there is a considerable range of values due to the wide range of interlayer coupling between different classes of cuprates. For YBCO doped to it's highest T_c the $\hat{c}$-axis penetration depth is about 11000 Å. For less three dimensional materials, λ_c can be more than ten times larger.

For the superfluid response, the relevant correlation length is the coherence length ξ, which is much smaller than λ and one would expect to be safely in the local limit. However, Kostin and Leggett [10] have shown that for an applied H field parallel to the $\hat{c}$-axis of a clean d-wave superconductor, non-local effects in the penetration depth may appear below a crossover temperature of about 1 K, due to the coherence length getting large at the nodes. In this thesis work, this particular geometry has

not been used. Furthermore measurements have not been made below 1 K, so that we are confident to be in the superfluid locality regime. For the normal fluid, the characteristic length scale is the mean free path of quasiparticles. In clean systems at low temperatures it is possible for this length to exceed the in-plane penetration depth. However, in the highly two dimensional cuprates this kind of non-locality is greatly suppressed for driving fields parallel to the *ab* plane, the geometry used in our studies.

As a first step in understanding the microwave response, it is useful to adopt a simple model for the normal fluid conductivity σ_n. An early ansatz by Bonn *et al.* [11] who studied the in-plane microwave properties of YBCO was to assume that the in-plane normal fluid response could be characterized by a phenomenological Drude 2-fluid model. We will assume a Drude spectrum for our discussion here, and write the conductivity as [2]

$$\sigma(\omega) = \frac{ne^2}{m^*}\left(\frac{f_n}{1/\tau + i\omega} + \pi f_s \delta(\omega) - \frac{if_s}{\omega}\right) \tag{1.5}$$

where the quantities, f_n and f_s are the normal and superfluid fractions, and $f_n + f_s = 1$. $1/\tau$ is the quasiparticle transport scattering rate. The superfluid fraction is equal to zero above the critical temperature, and it rises to unity as $T \to 0$. The temperature dependence of the magnetic penetration depth yields a measure of f_s, through the relation $f_s = \lambda^2(0)/\lambda^2(T)$.

Figure 1.1 is a schematic depiction of what a Drude conductivity spectrum would look like for a superconductor for (a) $T > T_c$, (b) $T = 0$, and (c) $0 < T < T_c$. The microwave measurement frequency is shown in the top panel, and is much smaller than the scattering rate in the normal state (usually several thousand GHz). The

[2]The conductivity of a d-wave superconductor has been worked out to have a simple energy-averaged Drude form, with a lifetime dependent on energy and strength of impurity scattering [12]. The energy independent lifetime assumed by Bonn *et al.* nevertheless does capture important in-plane properties of the superconducting state, and we will discuss its strengths and weaknesses in light of our new measurements in chapter 3.

conductivity obeys the Kramers Kronig relations, and the integrated weight under $\sigma(\omega)$ is constant. At zero temperature, a substantial fraction of the area under $\sigma_1(\omega)$ has shifted into a delta function at zero frequency, and represents the strength of the superfluid condensate. Some fraction remains at finite frequency at zero temperature, but this is usually small in good quality samples.[3] At finite temperature in the superconducting state, Fig 1.1c, the normal fluid oscillator strength rises at the expense of superfluid strength in the system, with a correspondingly smaller delta function strength. Experimentally we can use the measured superfluid density, and this sum rule to check for the consistency of the conductivity model which is used to integrate out the measured conductivity. This will be discussed in chapter 3, when we use a Drude model to determine the normal fluid oscillator strengths for the $\hat{a}$-axis conductivity in $YBa_2Cu_3O_{6.99}$.

[3]Strictly speaking, this is only true for the *ab*-plane conductivity. The $\hat{c}$-axis conductivity is characteristic of a very dirty material, and there can be significant weight left at high frequencies.

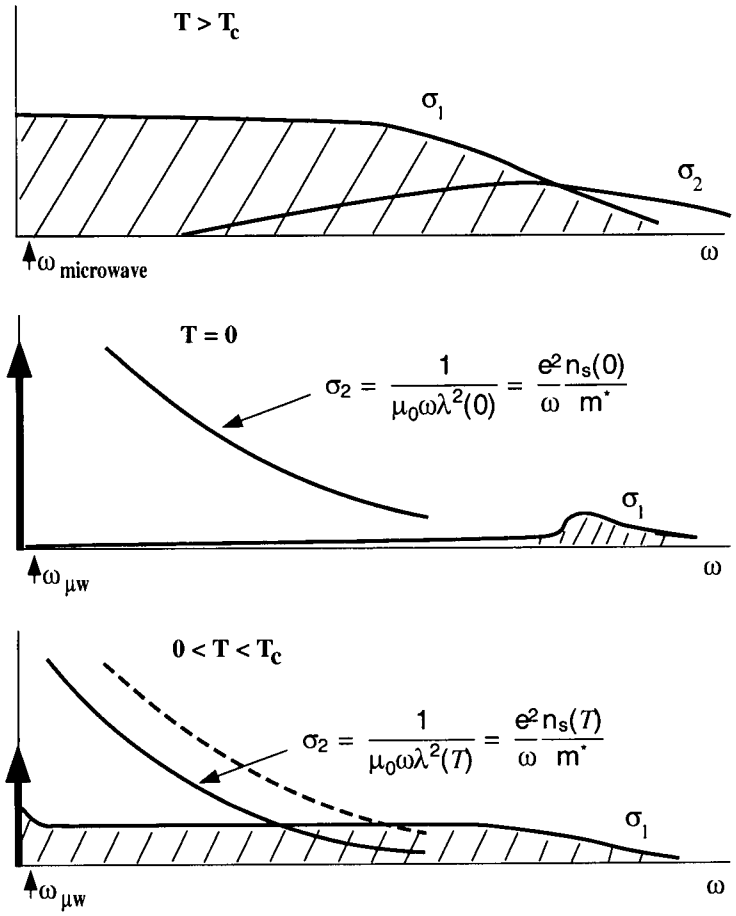

Figure 1.1: Schematic view of the complex conductivity of a d-wave superconductor.

1.3 The unconventional superconductor $YBa_2Cu_3O_{7-\delta}$

Yttrium Barium Copper Oxide (YBCO), was among the first discovered HTSC superconductors, and the one that has created a lot of excitement in the physics community. Its ease of preparation, and the possibility of producing high quality samples, has made it among the most grown and studied member of the cuprate family.

1.3.1 Crystal Structure and Phase Diagram

YBCO has a perovskite-like crystal structure shown in Fig. 1.2, with orthorhombic lattice parameters: a = 3.9198 Å, b = 3.8849 Å, and c = 11.6762 Å. The unit cell is layered and consists of a pair of CuO_2 planes sandwiching a layer of Y atoms, and a pair of BaO layers which sandwich a layer of one dimensional CuO chains that run along the $\hat{b}$-axis. The O(1) and O(5) sites are the chain oxygen sites, and the Cu(1) is a chain copper site. The O(4) is called the apical or interstitial oxygen. In Fig. 1.2 all the O(1) sites are filled and the material is fully oxygenated (the Ortho 1 phase). The oxygens in the $CuO_{1-\delta}$ chain layer are sufficiently weakly bound that even at temperatures well below the melting temperature of YBCO, the system has a finite oxygen pressure, which is a function of temperature and stoichiometry. This allows for oxygen to be inserted and removed from the lattice with ease. At low dopings ($\delta > 0.72$), the probabilities of having either the O(1) or O(5) sites occupied are nearly equal, and the material is in a tetragonal phase with the a and b axis lattice constants equal. For smaller values of δ, the probability of occupying the O(1) site is enhanced and the system undergoes a phase transition to an orthorhombic phase. At this point, the oxygens tend to form 1-d chains along the $\hat{b}$-axis of the crystal. This chain layer acts as a charge reservoir, and controls the oxidation state of the planar coppers. The chains also present another conduction channel making transport properties in the ab-plane anisotropic. The phase diagram is shown in Fig 1.3.

At $\delta = 1$, all the planar coppers are in the Cu^{2+} state with one unpaired spin per site. These favour antiferromagnetic ordering, and neighbouring spins are antiparallel. The high antiferromagnetic ordering temperatures indicates that these spins are coupled very strongly. It is believed that due to the strong onsite Coulomb repulsion, the energy cost for electrons to hop between sites is so large that the system is driven to localized electronic states, and the material is a Mott insulator. Away from $\delta = 1$, the introduction of holes in the planes destabilizes the antiferromagnetic spin

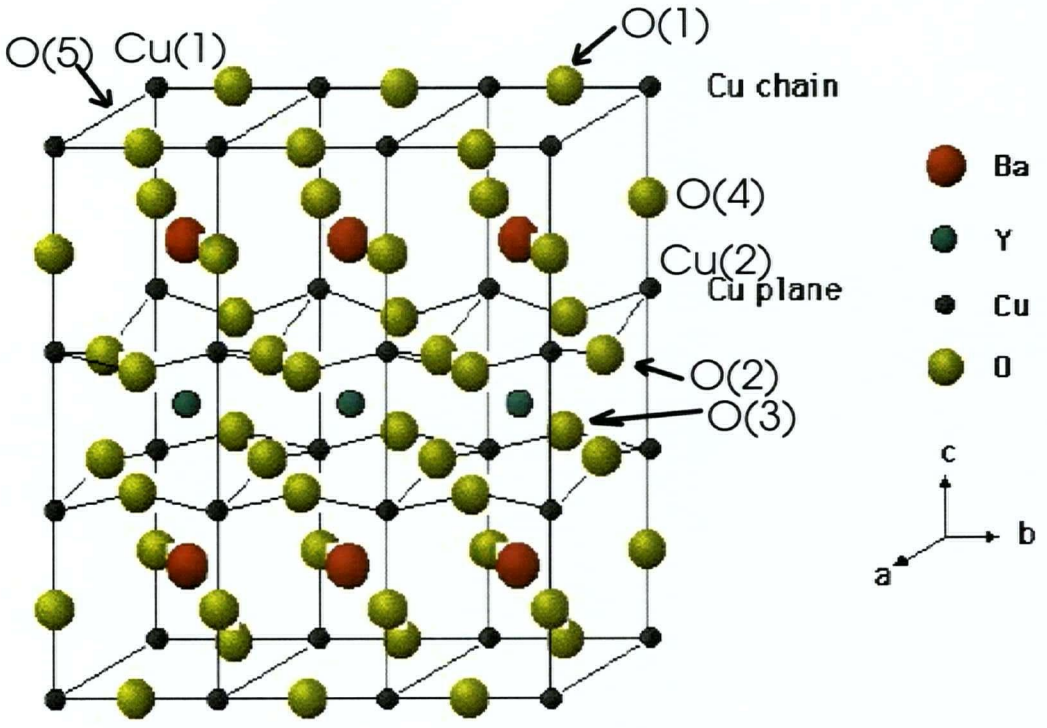

Figure 1.2: Three unit cells of fully oxygenated YBCO.

order, and the material is no longer an insulator. At a doping of $\delta < 0.65$ the hole concentration is sufficient to favour superconductivity. The mechanism which drives the formation of these cooper pairs is still a central question in the field today, and there is no general consensus among researchers.

1.3.2 Normal State Properties

The normal state of the cuprates presents a system where the electronic correlations in the system cannot be ignored, as is the case for weakly interacting Fermi liquids. The difficulties in understanding the physics of this state are firmly rooted in the proximity to the antiferromagnetic phase and the highly correlated electronic degrees of freedom. These strong correlation effects can lead to many interesting properties.

One of the first interesting observations has been the temperature dependence of the in-plane resistivity, which shows a linear T dependence over a significant range

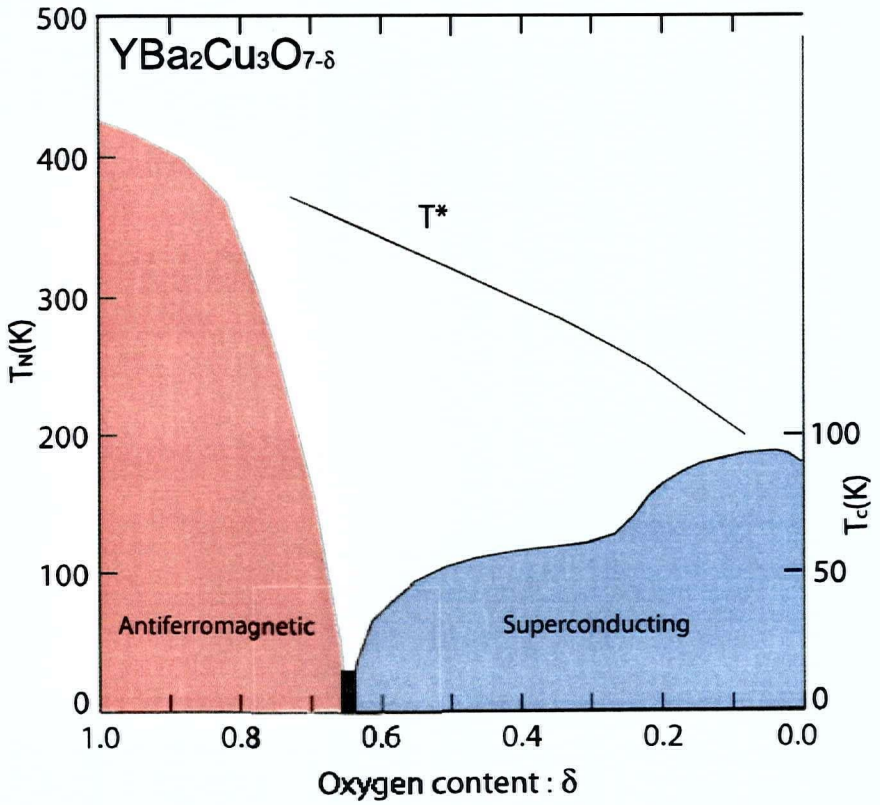

Figure 1.3: Experimentally determined doping phase diagram of $YBa_2Cu_3O_{7-\delta}$ [13]. Note the different scales for T_c and the Néel temperature T_N.

above T_c. The out of plane transport on the other hand shows a diverse range of behaviours, as shown in Fig 1.4, from metallic-like resistivity ($d\rho/dT > 0$) at full doping to semiconducting-like behaviour ($d\rho/dT < 0$) at the lower end of the doping phase diagram [15]. The degree of anisotropy also increases for lower dopings, although YBCO remains one of the least anisotropic members of the HTSC family of cuprate superconductors. At optimal doping the anisotropy ratio (ρ_c/ρ_{ab}) is ~ 50 [15]. The magnitude of the $\hat{c}$-axis resistivity is however much larger than band-structure predicted values, and the optical conductivity is spread over an anomalously broad frequency range. It appears that there is a "confinement" mechanism at play to reduce the intercell hopping rate to the observed values, a possible sign of a non-Fermi liquid ground state [2].

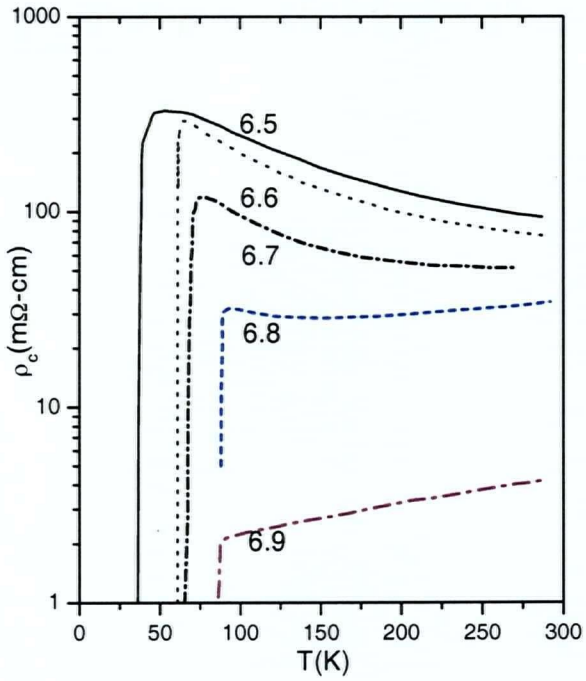

Figure 1.4: Effect of doping on the $\hat{c}$-axis resistivity [14].

The linear in-plane resistivity is also not well understood in the quasiparticle picture of Fermi liquid theory, where quadratic behaviour is expected. Other discrepancies exist with Fermi liquid behaviour, such as a temperature dependent Hall coefficient and non-Korringa behaviour in the NMR relaxation rate. Furthermore, normal state data from angular resolved photoemission (ARPES) measurements lack evidence for a coherent quasiparticle peak in the single particle spectral function, and bring into question the existence of a Fermi surface and a Fermi liquid description.

Other techniques have also been used to study the normal state, and one of the interesting phenomena encountered has been the observation of a pseudogap in the underdoped regime of the cuprates. This was first seen in NMR measurements of the Knight shift that showed a drop at a temperature T^*, which was above T_c. Normally the drop in the spin susceptibility due to the pairing of the carriers into a spin singlet state does not occur until one reaches T_c. Other measurements such as tunnelling, infrared spectroscopy, specific heat, and *ab*-plane resistivity also show features at

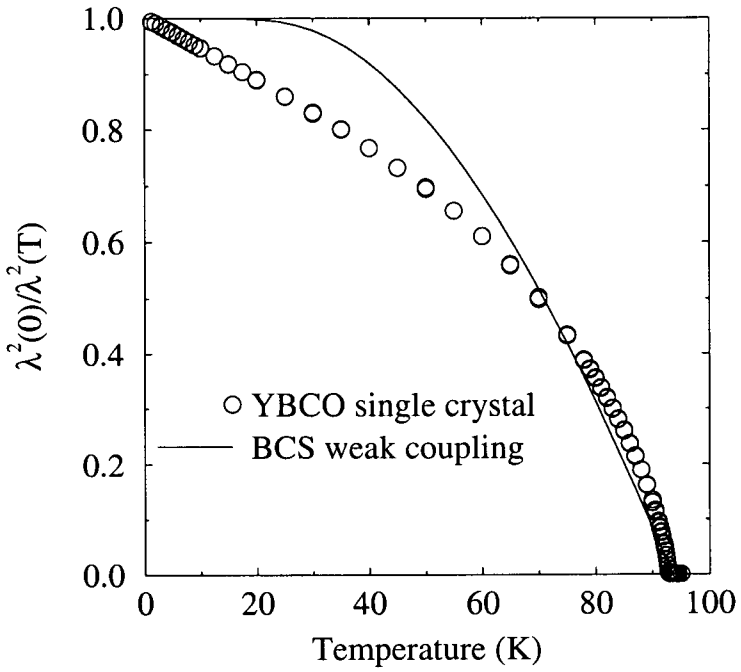

Figure 1.5: Normalized superfluid density plotted as $\lambda^2(0)/\lambda^2(T)$ in $YBa_2Cu_3O_{6.95}$, compared with BCS prediction.

around this temperature scale T^*. The observation of these features tend to occur at a lower temperature with increased carrier doping as shown in Fig 1.3, and at optimal doping there is no observation of T^*. It might be that T^* merges with T_c at the high dopings, or that it enters the superconducting dome.

1.3.3 Superconducting State

In comparison, the superconducting state in the cuprates has some features that are considerably simpler to understand. Early work by Hardy *et al.* on the penetration depth in $YBa_2Cu_3O_{6.99}$ showed a linear T-dependence of the in-plane superfluid density as shown in Fig. 1.5 [6]. This was a direct indication that there were low-lying states at temperatures as low as 1 Kelvin, a clear sign that the density of states differs from that of conventional s-wave superconductors. However, the density of states can in principle be modified by a highly anisotropic s-wave state, which has the same

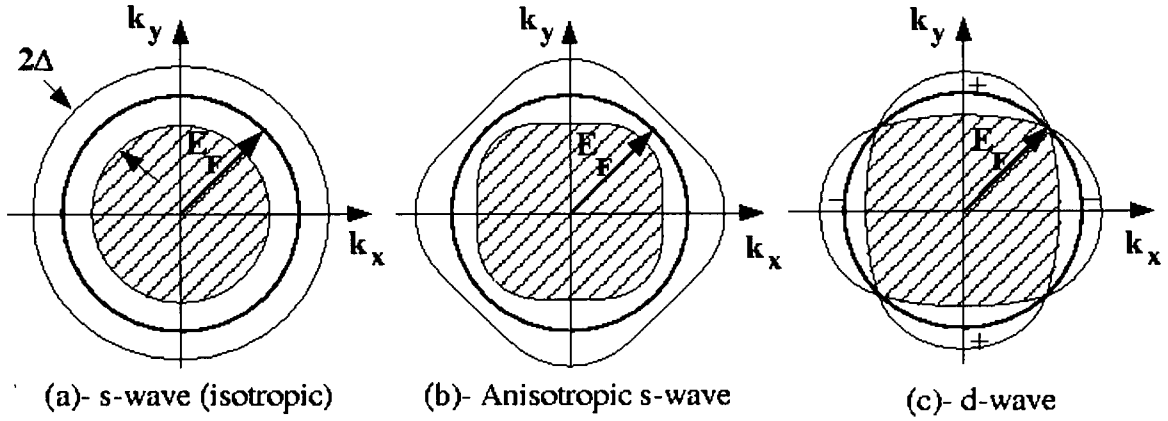

Figure 1.6: Various gap functions for a 2D square lattice.

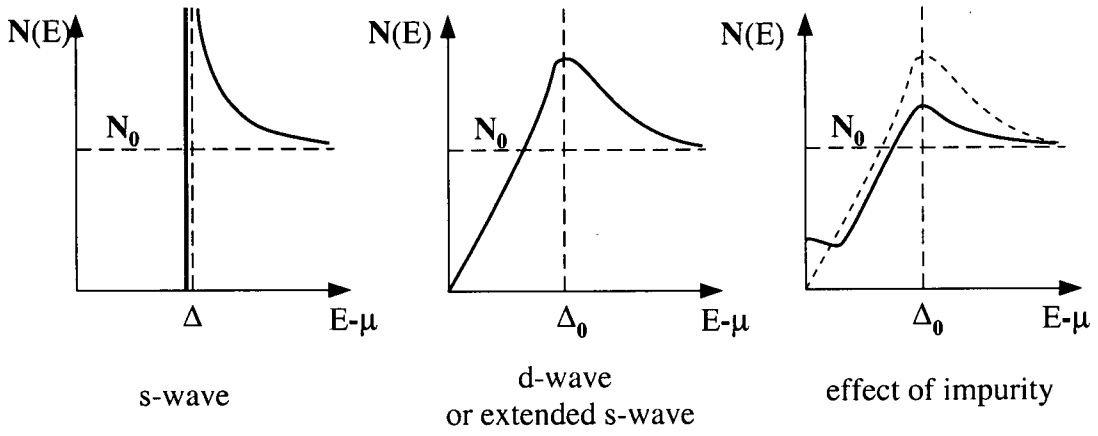

Figure 1.7: Density of states for s-wave, d-wave, and d-wave with impurities.

symmetry as the crystalline point group. Unconventional pairing states breaks this symmetry, and the work of Tsuei *et al.* [16], and Kirtley *et al.* [17] on YBCO junctions has shown the phase of the order parameter to be consistent with a $d_{x^2-y^2}$ state. Other experiments such as nuclear magnetic relaxation, tunnelling conductance, and angular resolved photoemission are also consistent with this pairing state. The d-wave state was hard to observe in the early years of work on these materials, due to the strong influence of disorder on the low-lying states, Fig. 1.7. It was an early result of work in heavy-fermion metals that any superconducting state with gap nodes would have a finite residual density of states at the Fermi level in the presence

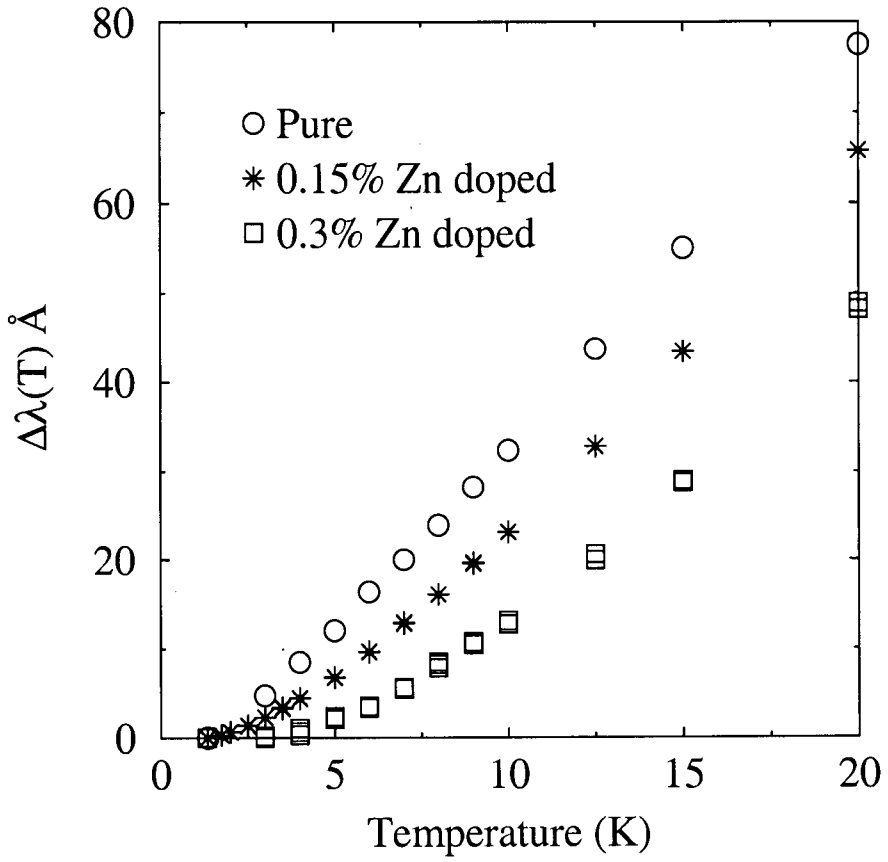

Figure 1.8: Effect of zinc substitution on the penetration depth [19].

of scattering. This was carried over to the d-wave superconductors by Hirschfeld *et al.* who considered the simplest case of isotropic elastic point-like impurity scattering [12, 18]. Their treatment was done self consistently in a t-matrix approximation (SCTMA) developed to account for impurity pair breaking effects which modify $N(E)$ and the electron self-energy. The theory predicts that at low temperatures quasiparticle states interact with impurities to form localized states. The overlap of these states creates an impurity band, whose width is set by an energy scale γ, which is set by the strength of the scattering and the concentration of impurities. Above this scale the density of states follows the d-wave density of states $N(E) \sim E$, and usual clean limit behaviour is expected. These ideas were tested for scattering in the unitary limit where this scale has a simple form given by $\gamma \sim \sqrt{\Delta_0 \Gamma}$, and becomes easily acces-

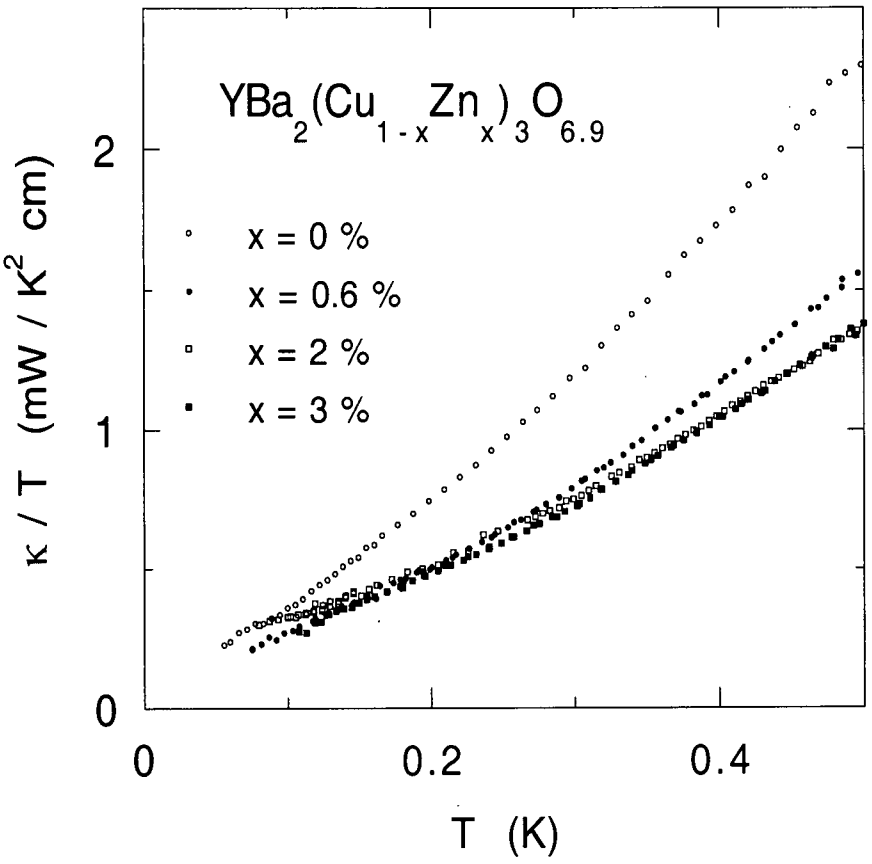

Figure 1.9: Low temperature thermal conductivity of pure and zinc doped YBCO [20].

sible with minimal concentrations of impurities. Γ is the elastic scattering rate that the impurities would contribute to the normal state resistivity. For the penetration depth, it was systematically shown by Bonn *et al.* [19] that zinc impurities, which are believed to scatter strongly, alter the linear temperature dependence away from linearity towards quadratic behaviour, as shown in Fig. 1.8. This crossover is below $\gamma/k_B \approx 7$ K for 0.3% Zn doped $YBa_2Cu_3O_{6.95}$. Another result of the early SCTMA calculations was the appearance of a universal conductance in the limit of zero temperature and frequency. This was initially predicted by Patrick Lee [21], who had studied localized states in a 2D d-wave superconductor. The universal conductivity is a result of a counter effect taking place between the rise of the residual density of

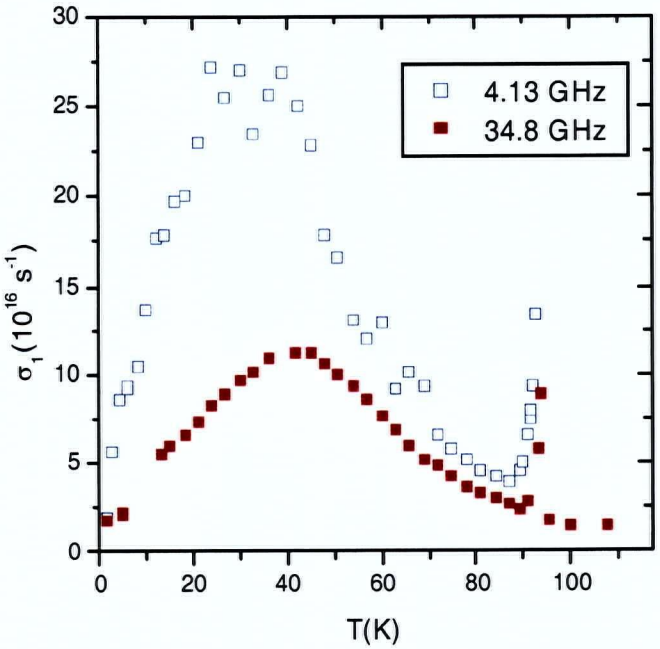

Figure 1.10: Early measurements of the microwave conductivity in YBCO [19].

states, and the decrease in the transport mean free path with impurity concentration, exactly cancelling in 2D. Taillefer *et al.* [20] measured the thermal conductivity in pure samples and ones with varying concentrations of zinc, Fig. 1.9. They found that at temperatures below 0.5 K, the thermal conductivity has an electronic linear term, whose slope is independent of impurity concentration and in agreement with Lee's prediction. On the other hand, measurements of the microwave conductivity have not yielded any limiting behaviour. This has been partially reconciled by Durst and Lee [22], where they show that by relaxing the isotropic scattering assumtion of the early SCTMA calculations, the $\omega \rightarrow 0$ microwave conductivity is enhanced relative to the thermal conductivity, which is unrenormalized.

At higher temperatures, the microwave conductivity has been studied by Bonn *et al.* [11]. The behaviour seen is strikingly different from the BCS superconductors where the conductivity develops a coherence peak immediately below Tc, and is exponentially activated at low temperatures. Instead a large broad peak is found to exist

in the superconducting state. This has been attributed to the collapse of the inelastic scattering of quasiparticles below T_c, and the decrease of their thermal population with decreasing temperature. A similar peak has been seen in the electronic thermal conductivity, [23], as well as in other electromagnetic absorption measurements [24, 25, 26, 27, 28, 29, 30, 31, 32, 33]. Such a lifetime effect is not seen in conventional superconductors because τ is governed by impurities or electron-phonon interactions, neither of which change abruptly at T_c. In the cuprate, the rapid temperature dependence of τ is governed by electron-electron interactions, and we will come back to this in chapter 3.

In the chapters to follow, we present a more detailed study of the in-plane electrodynamics of overdoped YBCO, and explore the evolution of the conductivity with frequency and temperature. The measurements allow one to see the evolution of the microwave conductivity into the superconducting state, and within a Drude formalism, extract self consistently the temperature dependence of the quasiparticle transport lifetime. The work is continued out of the *ab*-planes in chapter 4 where we study the evolution of the $\hat{c}$-axis conductivity and superfluid density in $YBa_2Cu_3O_{6.95}$. In chapter 5, we have studied the $\hat{c}$-axis superfluid density as a function of transition temperature at several doping levels in highly underdoped $YBa_2Cu_3O_{6.35\pm0.01}$.

Chapter 2

Experimental Methods and Theory

Electromagnetic probes of material properties typically involve trying to determine the electromagnetic response functions of the material, such as the complex dielectric function and conductivity. At microwave frequencies, which are typically several orders smaller than the maximum gap energy of the high temperature superconductors, the electromagnetic absorption in the superconducting state is extremely small. The traditional techniques of transmission and reflection spectroscopy which are used at mm-wave and infrared frequencies turn out to be insensitive. In this chapter, a brief review is given of cavity perturbation, a technique of choice at microwave frequencies. The methods developed have been tailored to study the cuprate superconductors, where the limitations of anisotropy and small sample size have been overcome.

In the work described herein, the technique of cavity perturbation was used at five frequencies: 1.14, 2.25, 13.4, 22.7 and 75.3 GHz, with each requiring a separate system. Here we will restrict the discussion to the basics of the 22.7 GHz apparatus, with working details to be found in Hosseini's M.Sc thesis [34]. Details of the implementation of the other systems can be found in theses by Kamal [35], Dosanjh [36], and Harris [37].

2.1 The Surface Impedance

The surface impedance of a metal or superconductor is a measure of the absorption and screening characteristics of the material in the presence of an electromagnetic field. It is the quantity which is directly accessed through experiments and is defined

as the ratio of the complex power flow into the sample to the applied magnetic field at the surface:

$$Z_s = \frac{\int(\vec{E} \times \vec{H}).(-\hat{n})dS}{\int H_{\|}^2 dS} \tag{2.1}$$

$H_{\|}$ is the tangential component of the applied field. In the case of local electrodynamics, where the local current is related to the local electric field, the solution of Maxwell's equations gives

$$Z_s = R_s + iX_s = \sqrt{\frac{i\mu_0\omega}{\sigma + i\omega\epsilon}} \tag{2.2}$$

where the real and imaginary parts, the surface resistance and reactance, control the dissipative and reactive flows of power into the sample. Equation 2.2 shows the direct link between measurements of surface impedance and the conductivity.

For good conductors, the term $i\omega\epsilon$, which arises from the electrical displacement current, is orders of magnitude smaller than σ at frequencies well below the far infrared, and can be safely ignored. Equation 2.2 then has two limiting solutions depending on the relative magnitude of the real and imaginary parts of σ.

Metal: In the normal state of a metal at microwave frequencies, when the carrier scattering rate is much greater than the measurement frequency, we are safely in a Hagens-Rubin limit and $\sigma_2 \ll \sigma_1$. The solution of Eq. 2.2 is then the classical skin effect result,

$$R_s = X_s = \sqrt{\frac{\mu_0\omega}{2\sigma_1}} = \frac{1}{2}\mu_0\omega\delta \tag{2.3}$$

wherein a measurement of R_s or X_s yields the real part of the conductivity, or equivalently the skin depth δ.

Superconductor: In a superconductor, the superfluid screens the electromagnetic field much more effectively, and $\sigma_2 \equiv \frac{1}{\mu_0\omega\lambda^2} \gg \sigma_1$ provided we are not close to T_c. In this limit the surface resistance and reactance take on a rather simple

form,

$$R_s(\omega, T) = \frac{1}{2}\mu_0^2\omega^2\lambda^3(T)\sigma_1(\omega, T) \qquad (2.4)$$
$$X_s(\omega, T) = \mu_0\omega\lambda(T)$$

where we can clearly see that measuring the surface reactance gives the penetration depth directly, and the conductivity can be obtained from the measured surface resistance and penetration depth. For the numerical extraction of these quantities one actually works with the exact formula, Eq. 2.2, which is valid for the data both in the normal and superconducting states, as well as the data right through T_c.

The first step is then to measure the surface impedance Z_s, and this is done by the cavity perturbation method.

2.1.1 Cavity Perturbation: An Overview

The cavity perturbation method relies on structures which support resonant electromagnetic modes. These confined fields, in the form of standing waves, interact with any material present within the field volume. The sensitivity of the technique comes from the repeated interaction of the standing waves with the enclosure, such as the walls of the cavity or external perturbations present in the volume.

Traditionally, the approach used to study elemental superconductors has been to construct the whole resonator from the material under study. However this approach is not satisfactory in the case of high temperature superconductors, where high quality samples are available only in small platelets, typically a few square millimetres. Instead, a cavity constructed from a conventional superconductor is used, and the sample is inserted into the cavity fields. This is accomplished by means of a (dielectric) sapphire plate which also serves as a thermal link to an external thermometer and heater.

The microwave cavity can be thought of as a two port system, where microwaves are sent down transmission lines which couple to the microwave cavity. The sample's

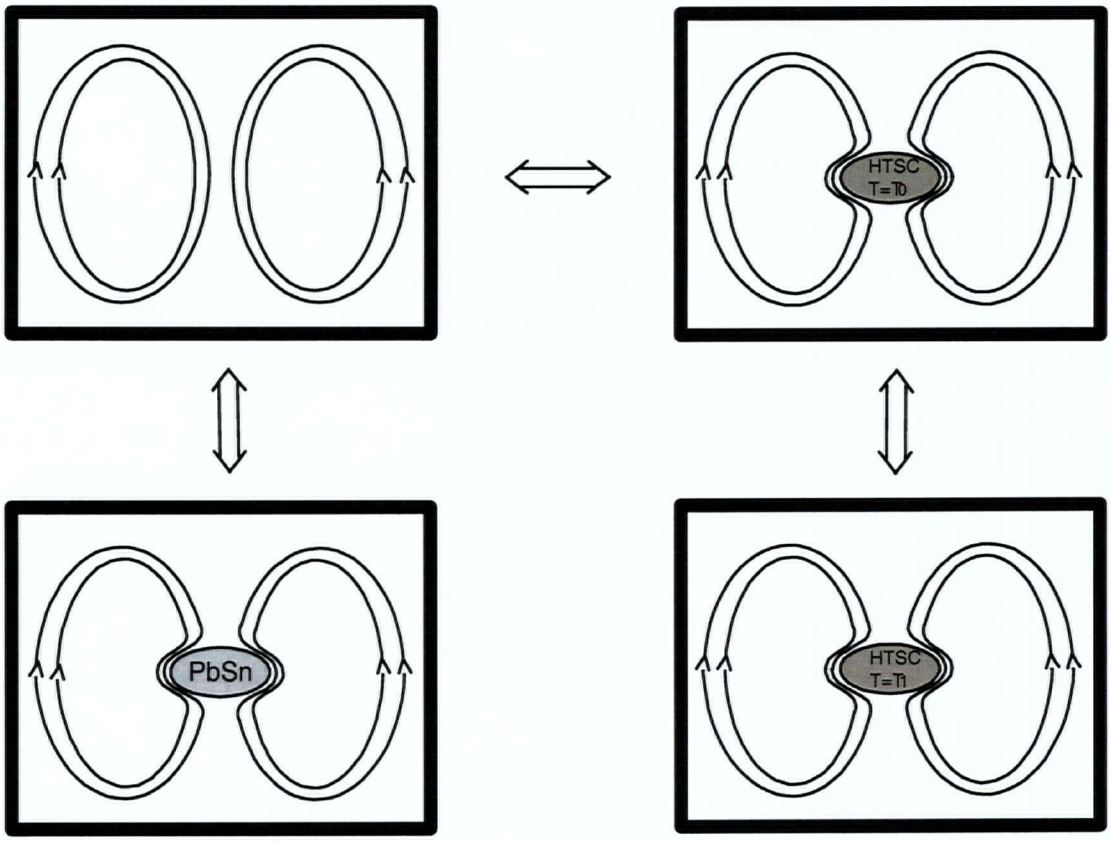

Figure 2.1: Cavity Perturbation Method: The response of the resonator is first measured without a sample. Subsequent measurements are taken with a sample placed in the cavity. The sample shown here is a high temperature superconductor, and it is initially at a base temperature T_0. The changes in surface impedance from the base temperature are easily measured by heating the sample to a higher temperature T_1, and measuring the new transmission characteristics of the resonator. The results are calibrated by comparing to a superconductor whose surface impedance is well known, here a sample of Pb-Sn.

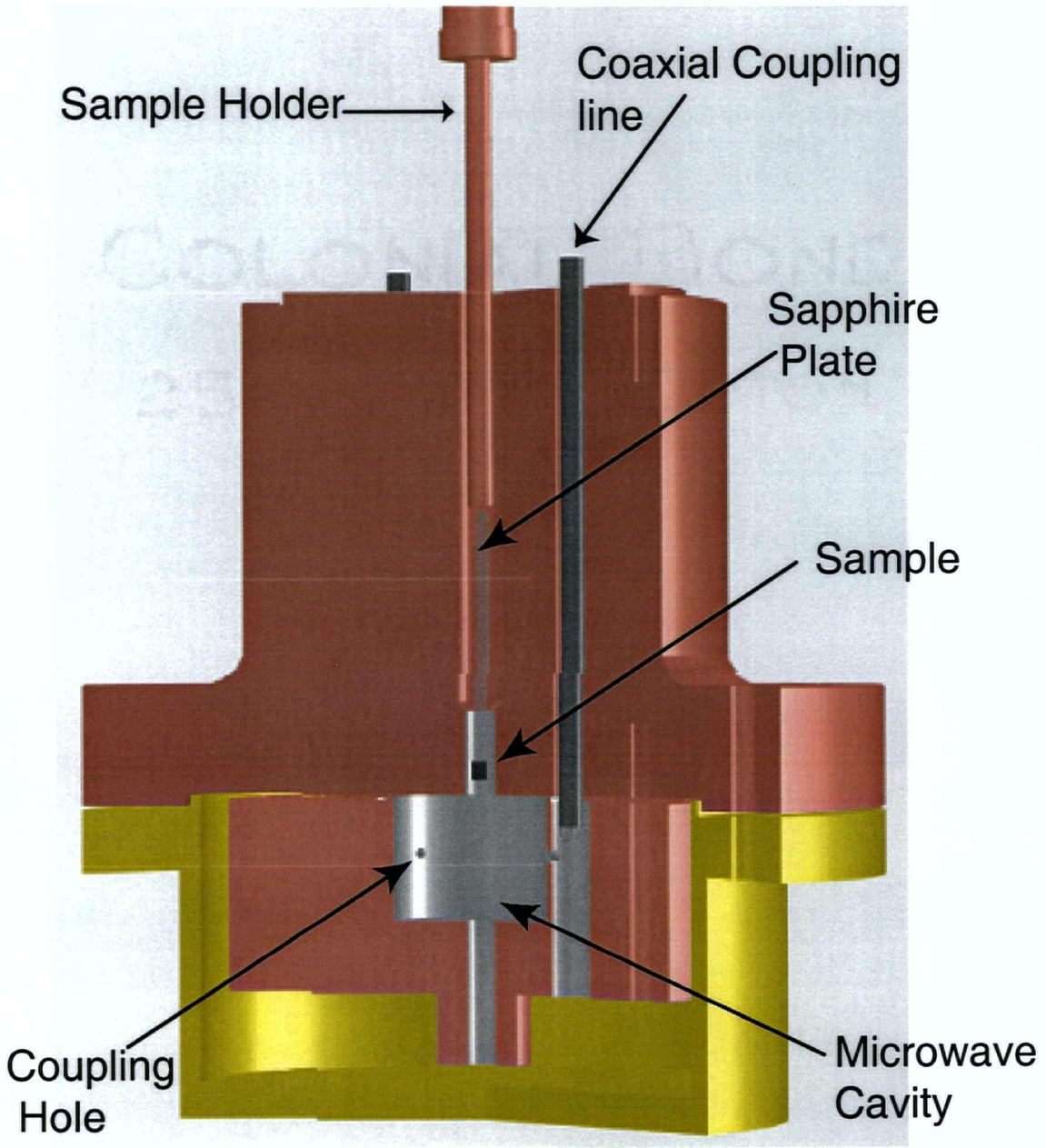

Figure 2.2: Schematic diagram of the 22.7 GHz Cavity.

interaction with the microwave fields of the cavity shows up as changes in the impulse response of the system.

Figure 2.1 illustrates the main idea behind the method. A key assumption of the technique is that the perturbation by the sample is weak enough that the field distribution does not change significantly elsewhere in the cavity (i.e no non-perturbative effect). This is most true when we consider perturbations from temperature changes of the sample. In this limit, the changes in surface impedance are easily related to changes in the centre frequency f_0, and quality factor Q, of the cavity. The cavity perturbation result (Appendix) then is given as

$$R_s(T) + \Delta X_S(T) = \Gamma \left[\Delta(1/Q(T)) + i\frac{2\Delta f(T)}{f_0} \right] \tag{2.5}$$

where $\Delta(1/Q(T)) = 1/Q_L(T) - 1/Q_U$, and $\Delta f(T) = f(T) - f(T_0)$. $\Delta f(T)$ represents the change in the centre frequency, of the cavity when the sample is heated from the base temperature T_0, to a temperature T. Q_L is the quality factor of the cavity while loaded with a sample at temperature T, and Q_U is the quality factor without the sample. The quantity $1/Q_U$ is equal to $1/Q_{walls} + 1/Q_{couplings}$, and contains losses from the walls of the cavity and the couplings. These are kept constant throughout the measurements by keeping the cavity at a fixed base temperature and keeping the coupling loops in a fixed position at all times while loading and unloading a sample. The loaded quantity $1/Q_L$ contains in addition to the wall and coupling losses, losses due to the sapphire plate $1/Q_{sapphire}$, the grease used to hold the sample $1/Q_{grease}$, and the quantity of interest $1/Q_{sample}$. Usually the experiments are carried out without a superconducting sample beforehand to get an estimate of the contributions from the sapphire and grease. We find that the magnitude of this background contribution is typically[1] $1/Q_{sapphire} \approx 1 \times 10^{-10}$ (nearly T-independent from 1.2 to 80 Kelvin), and $1/Q_{grease} \approx 3 \times 10^{-10}$ to 1×10^{-9} varying linearly from 1.2 to 80 Kelvin. In contrast the contribution from a typical sample of YBCO (0.7 mm^2) is $1/Q_{sample} \approx 3 \times 10^{-9}$

[1]The numbers given here are for the perturbation of the 22.7 GHz cavity in its TE_{011} mode.

at 1.2 Kelvin and strongly temperature dependent, so that the sapphire and grease losses although subtracted are negligible at high temperatures.

The calibration constant, Γ, is a geometric constant which can be calculated if one knows the field distribution in the cavity, and the size of the sample. This can be done for standard cavities, such as the cylindrical one to be discussed, provided there are no non-perturbative or demagnetization effects. For the measurements in this work, the field is almost always applied along the long faces of the samples ensuring negligible demagnetization factors.

In practice the calibration constant is more accurately determined using a calibration standard, usually a superconductor, whose resistivity is well known in the normal state. A lead-tin alloy was used to make calibration samples of the same size and shape as the superconductor being studied. The calibration sample's role is twofold. First through Eq. 2.3, the surface impedance of the reference is determined by its normal state resistivity which can be separately measured; this gives Γ once the bandwidth response is measured in the normal state. Secondly, at the base temperature of about 1.2 kelvin, the lead-tin reference being a BCS superconductor has nearly negligible absorbtion (compared to high temperature superconductors at the same temperature), and this means that its perturbation on the cavity Q can be judged as a measure of non-perturbative effects.

2.2 The cavity perturbation apparatus

The experiments at 22.7 GHz were performed using the cavity shown in Fig 2.2, with height dimension of 0.51" and a diameter of 0.74". The apparatus was designed in 1996, drawing on past experiences and difficulties of Kuan Zhang [38] and R. Knobel (1995) with the implementation of cylindrical cavities at 35 and 75 GHz. The frequency of 22.7 GHz was chosen to be low enough to be able to use coaxial lines, and thus avoid having to use rectangular waveguides as transmission lines to the

cavity. The coaxial lines were used to couple inductively through two small coupling holes present on either side of the cylindrical cavity, and are easily made to have adjustable coupling.

These cylindrical cavities are all operated in the TE_{011} mode, and have superconducting inner surfaces which yield high Q's. This is achieved by electroplating the inner walls of the copper pieces with an alloy of lead, which has 5 percent tin added. The tin keeps the lead from oxidizing, and prolongs the lifetime of the cavity before it needs to be replated.

The cavity is cooled to liquid helium temperature where the lead-tin alloy becomes superconducting. Further cooling from 4.2K to 1.2 K is achieved by pumping on the liquid helium bath which results in a further 20-80 fold increase in quality factor. Quality factors of the empty resonator as high as 320 million have been achieved in the 22.7 GHz TE_{011} mode.

The sample is introduced to the cavity by means of a slender sapphire plate, inserted along the central axis of the cavity. In the TE_{011} mode, the electric field has a node along this axis which greatly reduces the dielectric perturbation due to the sapphire plate. The sample is stuck on the plate with a small quantity of silicone grease, which has a relatively low dielectric loss, and bonds well at low temperatures. The sample is then moved to the center of the cavity, where the magnetic field magnitude is largest. This location produces the largest shifts seen in the frequency and quality factor as the temperature of the sample is varied. Sample temperatures in the range 1.2 to 250 Kelvin can be set by means of an external heater located at the base of the sapphire plate.

The measurements were performed with the cavity in transmission mode. A schematic view of the experimental arrangement is shown in Figure 2.3. The main goal is to obtain the most accurate value for the bandwidth and frequency of the resonator, since these are related to the surface resistance and reactance of the sample. In the simplest mode, the microwave synthesizer is swept in frequency through the

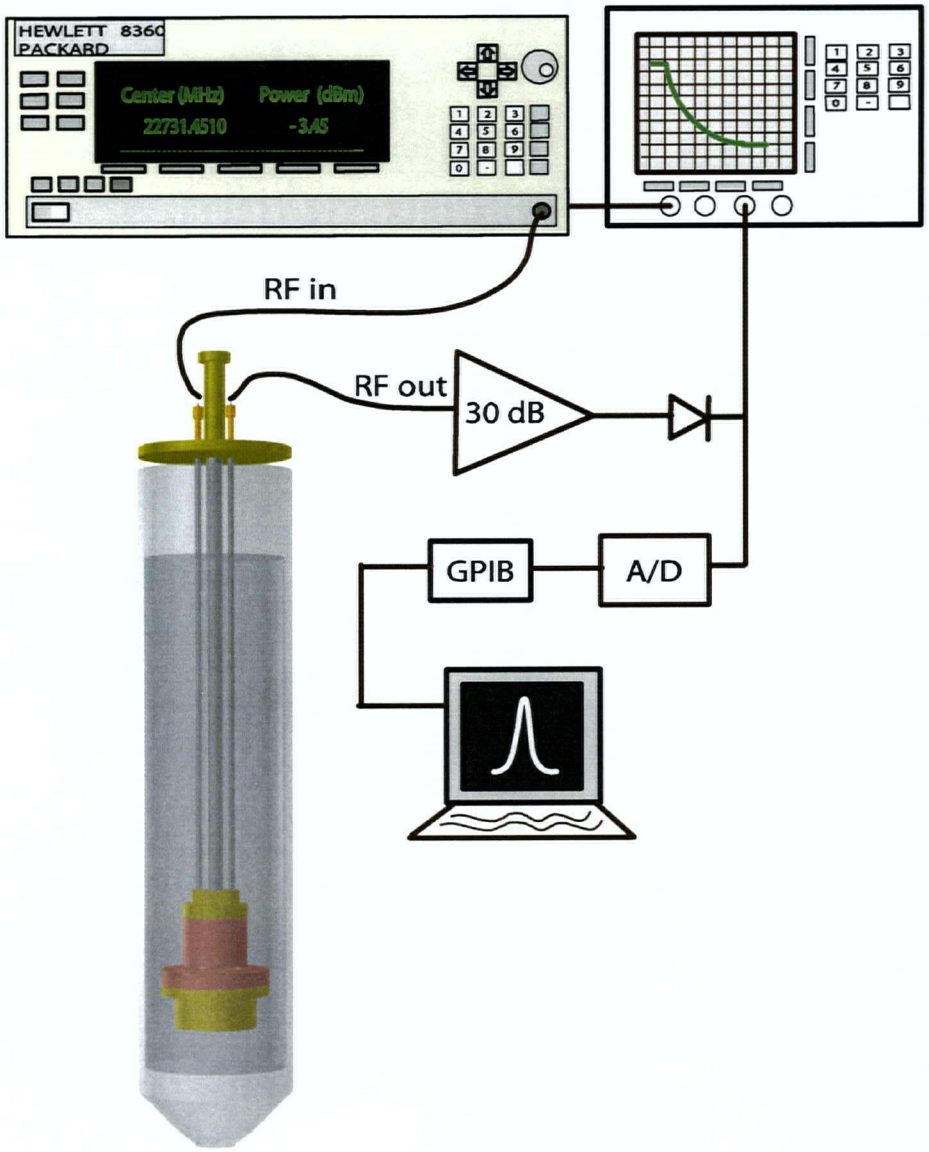

Figure 2.3: Schematic view of the microwave setup. The microwave synthesizer is either swept in frequency to obtain a frequency domain profile of the resonance, or pulsed at the centre frequency to obtain a time domain profile of the transmitted power through the cavity.

resonance window, and the transmitted microwave power is amplified by a Miteq 30dB amplifier, detected by an HP 8474C diode detector, digitized, and stored by computer. This works well when the samples are lossy and the resonator base quality factor is in the few million range. When well plated, the Q of the cavity exceeds 100 million, and small mechanical vibrations can have undesirable effects on the measurements. This is particularly true in our setup where we have a movable stage which loads and unloads the sapphire plate in-situ. Here, the frequency sweep technique is not so desirable, since the setup is prone to microphonics which causes the sapphire plate to vibrate in the cavity. This causes the narrow bandwidth response of the ultra high-Q cavity to move over several bandwidths during a measurement. In these instances, we have no accurate method to know the frequency well enough to calculate shifts as the sample temperature is varied. What can be measured with high accuracy, however, is the quality factor. The method adopted is to pulse the cavity with a short microwave pulse at around the centre frequency. The pulse has to be picked in such a way that its main power spectrum is wider than the range over which the resonance is moving, but long enough in time to channel sufficient energy into the cavity for detection. Values around 50 to 100 μs were used for the 22.7 GHz cavity. When the pulse is complete, the decay of transmitted power is registered on a fast digital scope. The time constant of this decay gives the Q factor accurately.

2.3 Sample Preparation for $\hat{c}$-axis Electrodynamics

The samples studied in the thesis have been placed in the axial field of the TE_{011} mode. The electromagnetic screening currents on the surface of the sample have to form loops that traverse two directions along the sample. As a consequence of the material anisotropy that there will be some screening and absorption from an unwanted face in the sample, usually the $\hat{c}$-axis of the crystal. For the work in chapters

4 and 5 however, we wanted to measure the $\hat{c}$-axis conductivity, and penetration depth. This has been done using a cleave technique or by polishing samples.

2.3.1 Cleaving Method

This technique relies on the fact that thin crystals of $YBa_2Cu_3O_{6.95}$ cleave very cleanly in the [100] and [010] directions. The method was pioneered by Kamal *et al.* in measuring the $\hat{c}$-axis magnetic penetration depth for crystals of $YBa_2Cu_3O_{7-\delta}$ in the doping range from $O_{6.6}$ to $O_{6.99}$. We have used it to measure the surface resistance of two samples of $YBa_2Cu_3O_{6.95}$ that were produced in yttria-stabilized zirconia crucibles. The details are covered in chapter 4.

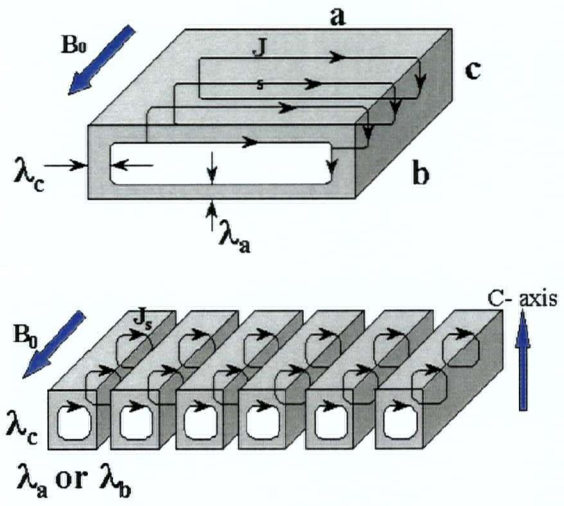

Figure 2.4: Sample before and after cleave. $\hat{c}$-axis contribution is increased with the cleave.

2.3.2 Polishing Method

This method will be shown to be useful in obtaining the $\hat{c}$-axis surface impedance of underdoped samples, and that of highly doped samples if care is taken to separate out the planar contributions. The method relies on reducing the planar contribution in

the geometry $\vec{H}_{AC} \perp \hat{c}$. Thick samples of $YBa_2Cu_3O_{7-\delta}$ have been carefully selected for the measurements. These crystals were typically 0.3-0.45 mm thick along the $\hat{c}$-axis and about 1 mm^2 in the plane. The steps taken to polish the samples have been developed over several years of trial polishing samples of YBCO.

Figure 2.5: Polishing station, and jig used to hold crystals.

In initial trials a diamond saw was used to cut away most of the crystal which would otherwise have to be polished away. Polishing blocks were designed out of cylindrical mild steel, about two inches in diameter and one inch in height. Varying height depressions were machined into one side for the sample to rest on. The sample would be attached by heating up the puck to 80 degrees and placing a small quantity of Crystal Bond (a commercial thermoplastic) at the centre of the puck. The sample would be moved over the melted Crystal Bond, and pushed lightly with a teflon tube to become level with the puck surface. When the puck was cooled to room temperature, the crystal bond hardened to keep the sample in place. Depending on the size of the depression, varying sample thicknesses could be achieved. The polishing was done on commercial diamond lapping pads stuck to glass for a level surface, using kerosene for lubrication. The grit sizes varied from 6 microns to start, to 1 micron and finally to 0.1 microns.

The samples were polished by moving the block in figure-eight patterns with care taken to avoid downward pressure. With the sample protruding from the block,

material would get removed very quickly on the $6\mu m$ pads, with several dozen turns removing tens of microns. When the sample would get to the level of the rim of the depression, the holder would have to get changed as further polishing would remove the rim of the block. This would show up as a black contaminant, which would risk scratching the crystal surface. When switching between pucks, and when going to finer grits, care was taken to wash the holders and the crystal in an ultrasonic heptane bath for a few minutes. Initially the sample was mirror smooth, but after the 6 micron polish, the sample would be visibly dull, with scratches clearly visible under 4 times magnification. Following the 1 micron polish, the sample was smooth to the eye, but scratches were still visible under the microscope. After the 0.1 micron stage, the sample was optically smooth, with a few unavoidable scratches due to contaminants. The final stage of polishing was given the most effort to ensure that enough material, typically 10 microns is removed, from the surface. This reduces deep dislocations which might have been introduced by the coarser grit sizes.

Evidence for possible surface damage was first noticed by examining the microwave properties of polished *ab*-plane faces of $YBa_2Cu_3O_{6.95}$ crystals whose intrinsic surface impedance were known [39]. The background absorption in such crystals were typically 3-10 times larger than intrinsic values found on as grown samples. Furthermore, the characteristic large peak present in the *ab*-plane surface resistance which is a sign of intrinsic behaviour, was diminished. To reverse the effects of polishing on the intrinsic microwave response, our samples were etched in a 0.5 percent solution of Bromine in Ethanol. The etch was seen to attack defect lines which would otherwise not be visible under a microscope. Studies were made for different etch periods, and it was found that a ten minute etch would almost recover the intrinsic behaviour seen prior to polishing.

More recent improvements to the polishing have included the purchase of an electric polishing station, with a variable speed rotating aluminum disc. Tests done by Jennifer Babiak have shown that a better polish is achieved using circular disks

of paper, which tend to create a softer bed for the crystal, and minimize the chance of breakage. Kerosene is used to attach the paper onto the rotating aluminum disk, and a small quantity of alumina grit is spread over the paper. Again, the polishing is done with several grit sizes, from 1 micron to 0.05 microns. The polishing jig which holds the crystal has also been modified by Dr D. Broun to have a spring loaded platform where the sample sits. This prevents excess pressure being applied to the sample while polishing.

Chapter 3

Microwave Spectroscopy of $YBa_2Cu_3O_{6.99}$

The in-plane microwave properties of YBCO have been extensively studied over the last decade. Early THz spectroscopy by Nuss *et al.*, Fig 3.1 [31], showed the appearance of a broad peak in the conductivity spectra below T_c and this was later seen as a broad peak in the surface resistance of optimally doped YBCO by Bonn *et al.* [40]. The broad peak seen in the conductivity was attributed to a competition between two temperature dependences: the overall decrease with temperature of the number of thermally excited quasiparticles competing with a rapid increase below T_c of their transport scattering time.

The rapid increase in the transport lifetime has been interpreted as a collapse of the inelastic scattering processes that are responsible for the large normal state resistivity of the high temperature superconductors. This effect has been observed in thermal conductivity measurements [23] as well as in other electromagnetic absorption measurements at microwave [24, 25, 26, 41, 27, 28, 42, 29], Far Infrared[30] and THz frequencies [31, 32, 33]. The rapid increase in quasiparticle scattering time has been well established by these measurements. However, obtaining a quantitative determination and the details of its temperature dependence has been limited by the need to use models to interpret single frequency microwave data.

In this chapter we present measurements at 5 microwave frequencies, which give us enough spectroscopic detail over a wide enough frequency range to produce a rather detailed picture of the evolution of $\sigma_1(\omega, T)$ in the superconducting state. These

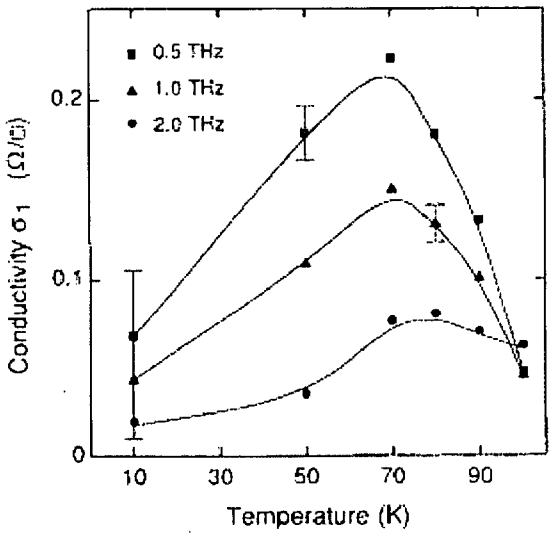

Figure 3.1: Early THz spectroscopy in YBCO.

results can be consistently understood within a Drude-like model for the thermally excited quasiparticle conductivity spectrum and now provide a much clearer measurement of the temperature dependence of the quasiparticle scattering rate below T_c.

3.1 The Measurement

The data shown in this chapter involve measurements with 5 resonators spanning a 1 to 75 GHz range and using a number of variations of the cavity perturbation method. The common feature is that all of the measurements were done on the same sample, a thin plate of $YBa_2Cu_3O_{6.99}$ oriented such that the microwave magnetic field of each cavity lay in the plane of the plate ($\vec{H}_{rf} \parallel \hat{b}$).

The sample used for the measurements was a single crystal of $YBa_2Cu_3O_{6.99}$ grown by a self-flux growth technique in $BaZrO_3$ crucibles [43]. The dimensions of the sample were initially $2 \times 1 \times 0.02$ mm^3 for the 1.14 GHz measurements, which have been reported elsewhere [44]. Subsequent measurements in the other resonators were

performed on smaller pieces cleaved from the original crystal, but measurements at 22.7 and 75.3 GHz were repeated on different pieces to ensure that the sample was uniform.

The measurements at 1.14 GHz were performed in a loop-gap resonator initially designed for measurement of $\lambda(T)$ [6]. Like the 22.7 GHz resonator already discussed, and most of the resonators used in our studies, the loop-gap is plated with a Pb:Sn alloy which is superconducting below 7 Kelvin and has very low microwave loss at 1.2 Kelvin. The 1.14 GHz loop-gap system is unique in that the sample is held fixed in the resonator, and cannot be removed from the resonator during the measurements. This is a necessary restriction for the high precision measurements of $\lambda(T)$ which rely on the sample being held rigidly in a position that does not vary when the temperature is changed. The value of $R_s(1.2\,K)$ at 1.14 GHz was estimated by comparing to separate experimental runs where the resonator is loaded with only the sapphire sample holder. The need to do this in two separate experimental runs gives the 1.14 GHz $R_s(T)$ measurements a relatively large uncertainty in the form of a temperature-independent background value ($\pm 0.7\mu\Omega$), although the resolution of the temperature dependence is much better than this. We do not attempt to extract $\lambda(1.2\,K)$ from the microwave measurements, but instead use values inferred from muon spin rotation, and far-infrared measurements [45, 46]. None of the analysis discussed here depends sensitively on this choice of $\lambda(1.2\,K)$.

The 2.25 GHz measurements have been performed in a Nb split-ring resonator described in more detail elsewhere [36]. Measurements at 13.4, 22.7, and 75.3 GHz were performed in the axial microwave magnetic fields of the TE_{011} modes of right-circular cylindrical cavities. In all of the measurements other than that at 1.14 GHz, the sample was moved in and out of the resonator in situ. This freedom made it difficult to measure $\lambda(T)$ at the higher frequencies, due to problems of controlling the motion of the sample as the temperature is changed. At 22.7 GHz, a modification was made later for a fixed loading design that enable us to measure the temperature

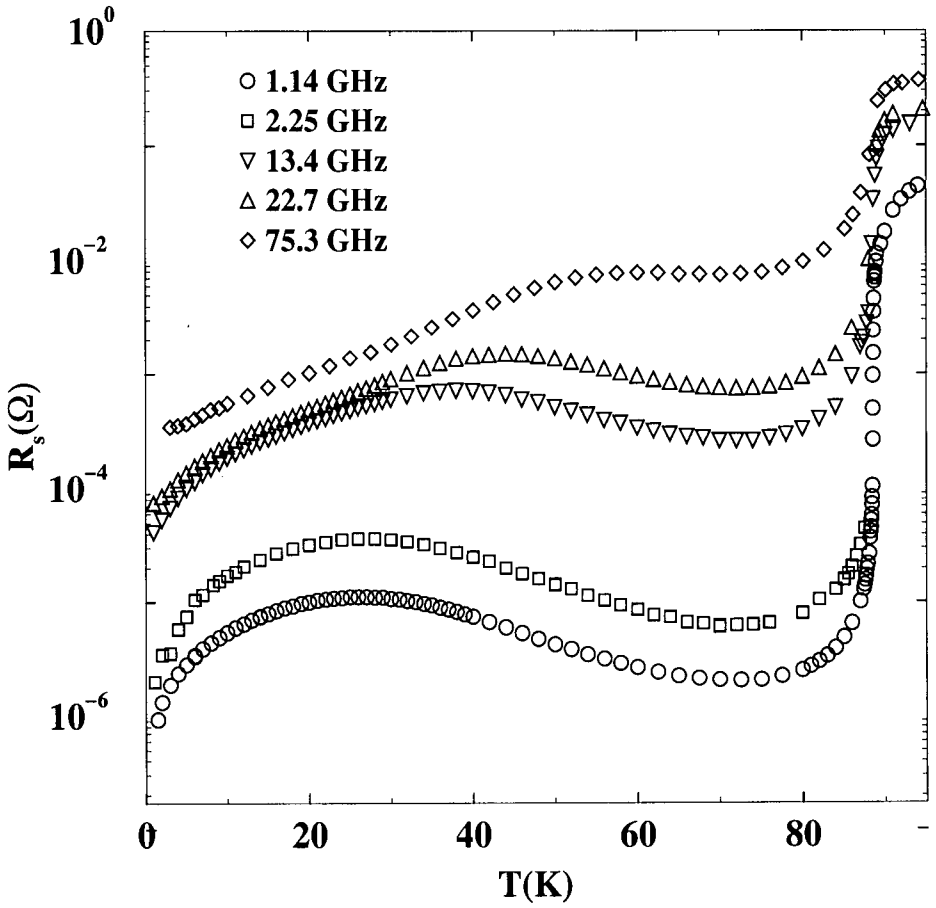

Figure 3.2: Log plot of the a-axis surface resistance of $YBa_2Cu_3O_{6.99}$.

dependence of the high frequency penetration depth.

The ability to pull the sample out in the 2.25, 13.4, 22.7 and 75.3 GHz measurements, made the background uncertainty in those data much less significant than it is in the 1.14 GHz data.

3.2 Experimental Results and Analysis

Fig. 3.2 shows the surface resistance of $YBa_2Cu_3O_{6.99}$ for currents running in the $\hat{a}$ direction. The rapid drop in $R_s(T)$ seen immediately below T_c is due to the onset of screening by the superfluid.

For comparison of the five data sets, it is convenient to plot the data in the superconducting state as R_s/ω^2 versus temperature, as shown in Fig. 3.3. This removes the frequency dependence from the surface resistance caused by imperfect screening by the superfluid. Above 65 K the loss scales as ω^2 to within $\pm 8\%$, a scaling that is expected if the microwave $\sigma_1(\omega)$ is frequency independent. This agreement lies within the estimated uncertainty in background and calibration constants, and provides a check on the degree to which one can compare the measurements at different frequencies.

The broad peak in $R_s(T)$ as mentioned is attributed to a quasiparticle scattering time τ that increases below T_c while competing with a decreasing density of thermally excited qusiparticles with temperature [40]. In the early measurements of Bonn *et al.* near 2 GHz it was found that the quasiparticle scattering time reaches a limiting value near 30 K, possibly due to impurity scattering, at which point the quasiparticle density takes over and causes $R_s(T)$ to fall again with further decreases in temperature [11]. The limiting behaviour brought about by the residual level of impurities present in those crystals were checked by studying samples doped with Ni and Zn [19]. These doping studies shown for zinc substitution in Fig 3.4, showed either a smaller peak shifted to higher temperature or no peak at all, consistent with the quasiparticle scattering rate running into an impurity limit at higher temperature, even when only 0.15% Zn was added to the sample. The new results shown for our high purity $BaZrO_3$ grown crystal confirms that it is the residual impurity scattering that limits the increase in quasiparticle lifetime, even in what were considered quite pure crystals. The low frequency surface resistance of the new crystal rises a factor of four above the minimum near 70 K, higher than the factor of two or less observed in earlier measurements of samples at 4 GHz [11]. These differences are consistent with a lower impurity scattering rate that is achieved at a lower temperature in $BaZrO_3$ grown samples rather than those grown in yttria-stabilized zirconia.

The frequency dependence of the peak in $R_s(T)$ provides further information

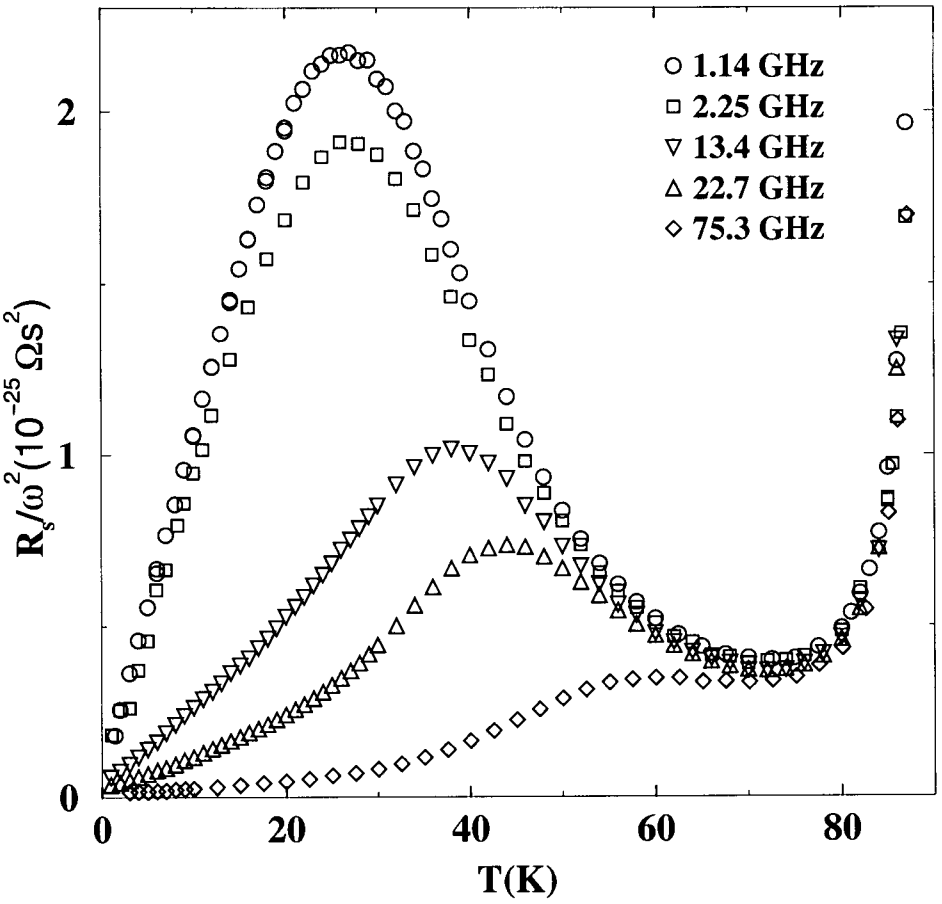

Figure 3.3: Surface resistance of $YBa_2Cu_3O_{6.99}$.

about the rapid increase in the quasiparticle lifetime. However it is more instructive to look at the microwave conductivity which can be extracted by knowing the surface resistance and the magnetic penetration depth. At 1.14 GHz both these quantities were measured and the magnetic penetration depth is shown in Fig 3.5 plotted as $\lambda^2(0)/\lambda^2(T)$. $\sigma_1(T)$ at this frequency was extracted numerically by inverting Eq. 2.2.

For the higher frequency data we were faced with the dilemma of knowing that due to the strong relaxation behaviour seen at lower temperatures in Fig 3.3, it was conceivable that the long lived normal fluid could oscillate with the driving electromagnetic fields before a scattering event, and do some screening of its own. This kind of screening has been observed directly in mm-wave measurements on

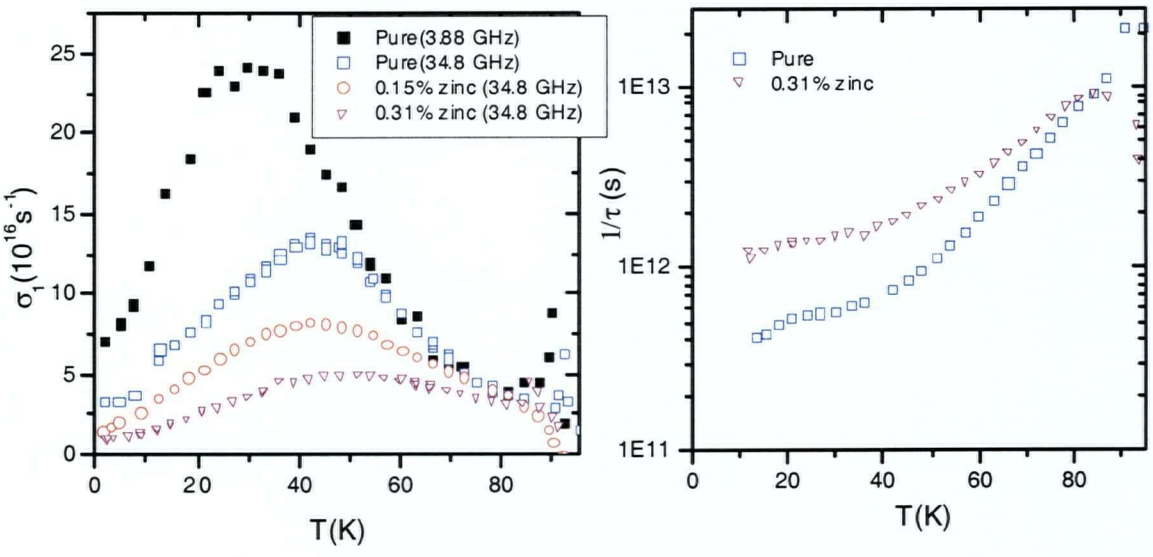

Figure 3.4: Conductivity in zinc doped YBCO samples [19].

high quality thin films [29], the effect of which is to add an imaginary conductivity to the total conductivity of the superconductor, and change the effective magnetic penetration depth.

We were able to get a handle on the size of the extra screening by assuming a Drude two fluid model for the conductivity that includes contributions to the real and imaginary part from both the superfluid and normal fluid. The 1.14 GHz $\sigma_1(T)$ that was obtained directly was used within this model to estimate the transport lifetime of the quasiparticle excitations, and from this the magnitude of the corrections [47]. It was found that the screening was only significant at the three highest frequencies, and at intermediate temperatures between 10 and 50 kelvin where the excitations are long lived and the normal fluid oscillator strength is not negligible.

To make absolutely sure however that the normal fluid screening was carefully accounted for, adaptations were made in the 22.7 GHz system at a later time to allow for careful measurements of the penetration depth at this frequency. Measurements were made on an optimally doped high purity sample at both 1.1 GHz and 22.7 GHz. Fig 3.6 shows the superfluid fraction, showing the deviation expected at temperatures below 50 K due to the normal fluid contribution to σ_2 at high frequencies. These re-

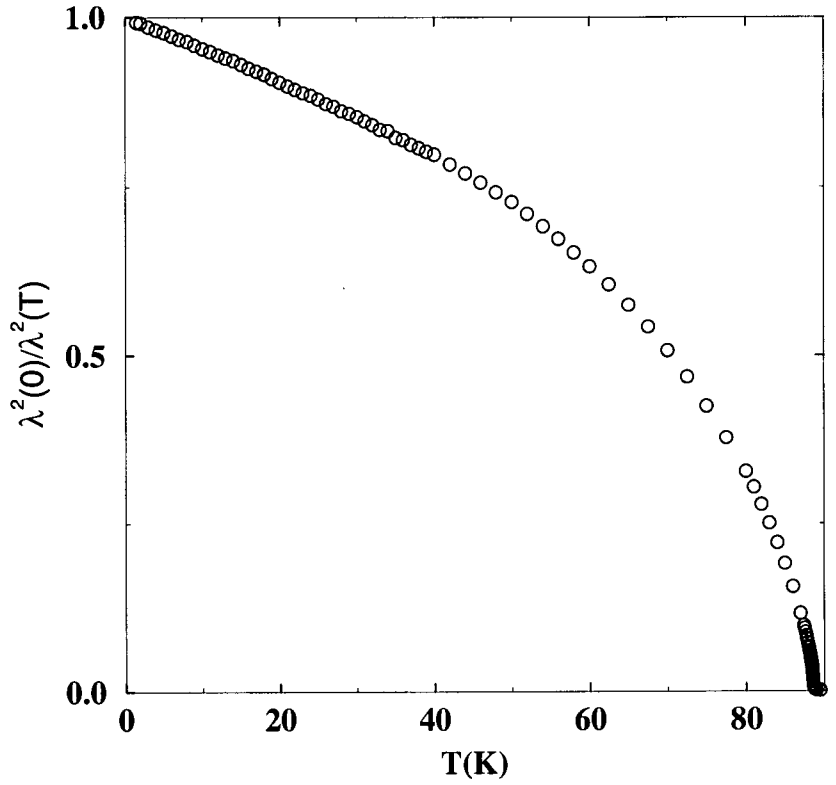

Figure 3.5: Normalized a-axis superfluid density in $YBa_2Cu_3O_{6.99}$.

sults were consistent with our 2-fluid model corrections to within 1%, lending support to our earlier analysis for the other frequencies.

Fig. 3.7 shows the conductivities extracted from the $R_s(T)$ data of Fig. 3.2, using the corrected penetration depths at each frequency. The sharp upturn at T_c marks the presence of superconducting fluctuations, which have been discussed in greater detail by Kamal *et al.*[48] and Anlage *et al.* [49] and are not the main focus of the work presented here.

The main feature observed in the conductivity is the large, broad peak rising to nearly 25 times the normal state conductivity. The peak rises a factor of two higher at 1 GHz compared to earlier generation studies, and it peaks at a lower temperature, 25 K instead of the 35 K turnover observed in lower purity crystals [19]. As mentioned above for the surface resistance, this is due to τ running into its impurity limit at

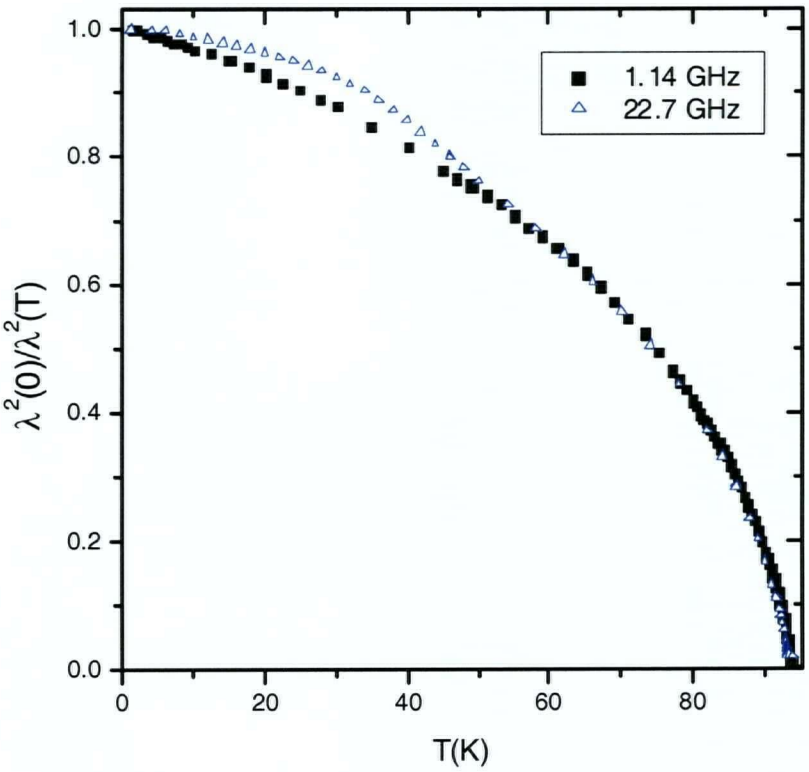

Figure 3.6: Enhanced high frequency screening by normal fluid in high purity $YBa_2Cu_3O_{6.95}$.

a somewhat lower temperature than it did in the earlier crystals and this impurity-limited scattering time is several times larger. An estimate of the increase can be made as follows. The penetration depth measurements indicate that more than 90% of the normal fluid density is gone at 25 K (see Fig. 3.5), so the 25-fold increase in σ_1 between T_c and 30 K implies an increase in τ by at least a factor of 250 over the scattering time just above T_c. This is actually an underestimate because not all of the far infrared oscillator strength in the normal state ends up condensed into the superfluid at low temperatures. Such a huge increase in lifetime is consistent with the relaxation effects observed in the data at 13 GHz and higher. As a rough illustration of this agreement, far infrared measurements indicate that $\omega\tau \sim 1$ at about 3000 GHz just above T_c, so a 300-fold increase in τ below T_c would mean $\omega\tau \sim 1$ at about 10 GHz, leading to the considerable frequency dependence in $\sigma_1(\omega)$ that is observed

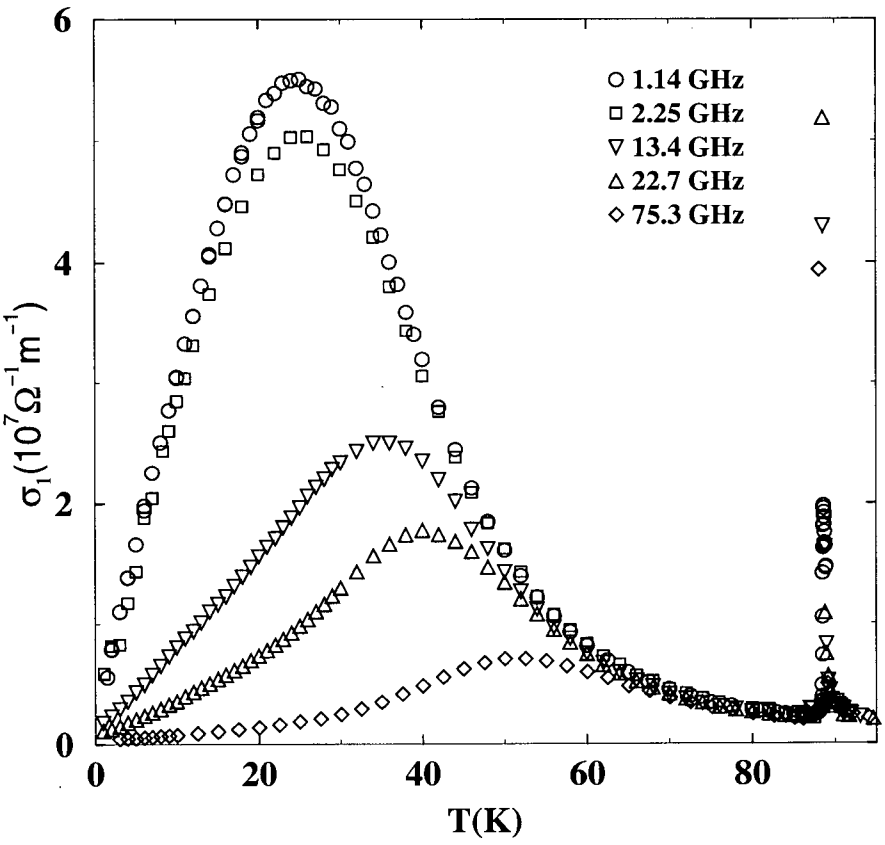

Figure 3.7: The temperature dependence of the $\hat{a}$-axis microwave conductivity of $YBa_2Cu_3O_{6.99}$ extracted from the R_s measurements of Fig 3.3.

in the microwave range.

3.3 Conductivity Spectra and Quasiparticle Lifetime

The evolution of the conductivity with temperature is better shown in Figs. 3.8 and 3.9 where we see the conductivity spectrum $\sigma_1(\omega)$ at several representative temperatures. Fig. 3.8 shows the conductivity spectrum at three temperatures below 25 K, the temperature range where we argue that the quasiparticles transport lifetime is dominated by residual impurity scattering. We will not concentrate here on the low-

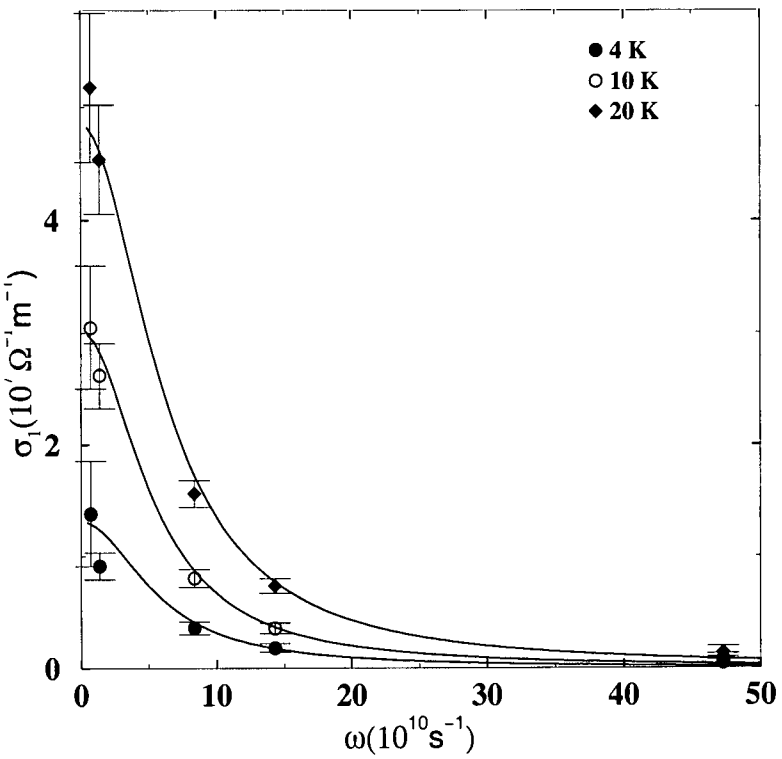

Figure 3.8: The conductivity spectrum at 4, 10 and 20 K.

est temperature data, where the loss becomes very small and difficult to measure accurately by most cavity perturbation techniques.

Fig. 3.8 shows that from 4 to 20 K, the conductivity consists of a very narrow peak whose width is largely temperature independent. The lines in the figure are weighted, least squares fits to a Lorentzian lineshape, demonstrating that the conductivity spectrum of the thermally excited quasiparticles is Drude-like. The main contributions to the error bars in these spectra are a combination of uncertainty in the individual measurements' calibration constants, plus a substantial uncertainty in the background loss in the 1.14 GHz measurements, and scatter in the 2.25 GHz measurements. Within these error estimates (mostly systematic error) there is very little clear deviation from a Drude lineshape when examining an individual spectrum at a particular temperature. The most noticeable deviation is in the spectrum at 4

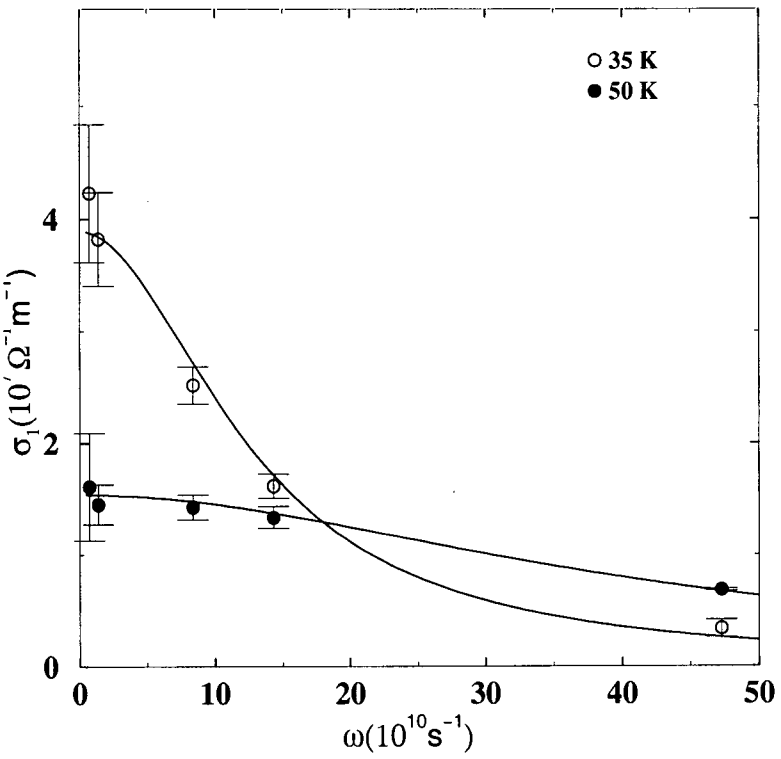

Figure 3.9: The conductivity spectrum at 2 temperatures above 20 K.

K, where the data may be taking on a slightly more cusp-like shape than the Drude curve. This region has been recently explored by a novel Bolometric method which is capable of measuring the frequency dependent conductivity (1 to 20 GHz) at temperatures below 9 Kelvin [50]. The lineshapes obtained at the lowest temperatures in overdoped YBCO are in fact more cusp shaped and do not fit a Lorentzian within experimental uncertainties.

An interesting cross-check of these fits to $\sigma_1(\omega)$ is to compare the oscillator strength in the normal fluid conductivity peak, which is given by the fit parameter $n_n e^2/m^*$, to the superfluid density $n_s e^2/m^* = (\mu_o \lambda^2)^{-1}$ extracted from the penetration depth measurements. If we assume that all of the oscillator strength ends up in the superfluid δ-function as T$\rightarrow$0, then the superfluid density is related to the normal fluid density via the relation $\frac{n_n e^2}{m^*}(T) + \frac{n_s e^2}{m^*}(T) = \frac{n_s e^2}{m^*}(T = 0)$. Fig. 3.10 shows a com-

parison between the normal fluid density inferred from the fits to the $\sigma_1(\omega)$ peaks and the normal fluid density inferred from the penetration depth. This figure shows that the normal fluid density does nearly track the decline of the superfluid density with increasing temperature, which indicates that our use of a two-fluid model to describe the screening is a reasonable procedure. The increasingly serious deviation between the curves above 40 K is an indication that the Drude lineshapes do not accurately keep track of all the oscillator strength at higher temperatures. There is also some deviation at low temperatures, taking the form of a normal fluid oscillator strength that is extrapolating linearly towards a non-zero value as T$\rightarrow$0. This is an indication that there is a residual conductivity in the low temperature, low frequency limit, and in fact not all the normal fluid oscillator strength goes into the delta function at zero frequency. This is to be expected for a d-wave superconductor [21].

The quality of the conductivity fits and the agreement in the oscillator strengths shown in Fig. 3.10 indicate that the Drude fits do provide a reasonable measure of the width of the peaks from 4 to 45 K. The temperature dependent width coming from these fits, which we interpret as the transport scattering rate of the thermally excited quasiparticles, is shown in Fig. 3.11. One of the key results of these measurements is that the width of the normal fluid peak is very small, 9$\pm$1 GHz, and it is nearly temperature-independent up to 20 K. The main change in the spectra in this temperature range is an increase in oscillator strength, due to the shift of spectral weight from the superfluid response (a δ-function at ω=0) to the microwave conductivity. The narrow width suggests a very long quasiparticle scattering time of $1.8(\pm 0.2) \times 10^{-11}$ s.

Fig. 3.9 shows that above 25 K the conductivity peak broadens rapidly and by 60 K the width becomes much greater than the frequency range of the microwave measurements, so we have no direct measure of the width and shape of $\sigma_1(\omega)$ above 60 K. The low level of defects in the $BaZrO_3$ grown crystal, coupled with the measurements at 5 microwave frequencies, allows us to determine the temperature de-

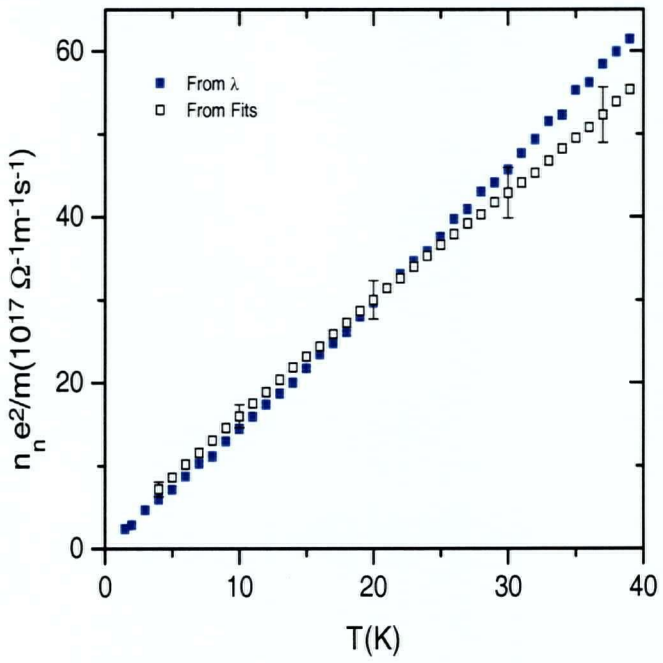

Figure 3.10: The normal fluid oscillator strength obtained from Drude fits to spectra, and from the disappearance of oscillator strength in the superfluid response.

pendence of the inelastic scattering rate over a fairly wide temperature range from 20 to 40 K. Qualitatively similar results have been obtained in measurements on thin films by high frequency microwave and THz techniques [31, 33]. However, the much higher level of defects in films limits the temperature range over which the evolution of the inelastic scattering rate can be observed. In the high purity crystals, the temperature dependent scattering can be tracked all the way down to 20 K. A fit to the form $1/\tau(T) = A + B(T/T_c)^y$ from 4 to 40 K yields an exponent $y = 4.2 \pm 0.1$, with coefficients $A = 5.2(\pm 0.4) \times 10^{10}\,\mathrm{s}^{-1}$ and $B = 4.6(\pm 0.9) \times 10^{12}\,\mathrm{s}^{-1}$, and is shown as the dotted dashed curve in Fig. 3.11. The uncertainty in the exponent indicates the maximum range that is consistent with the data to within

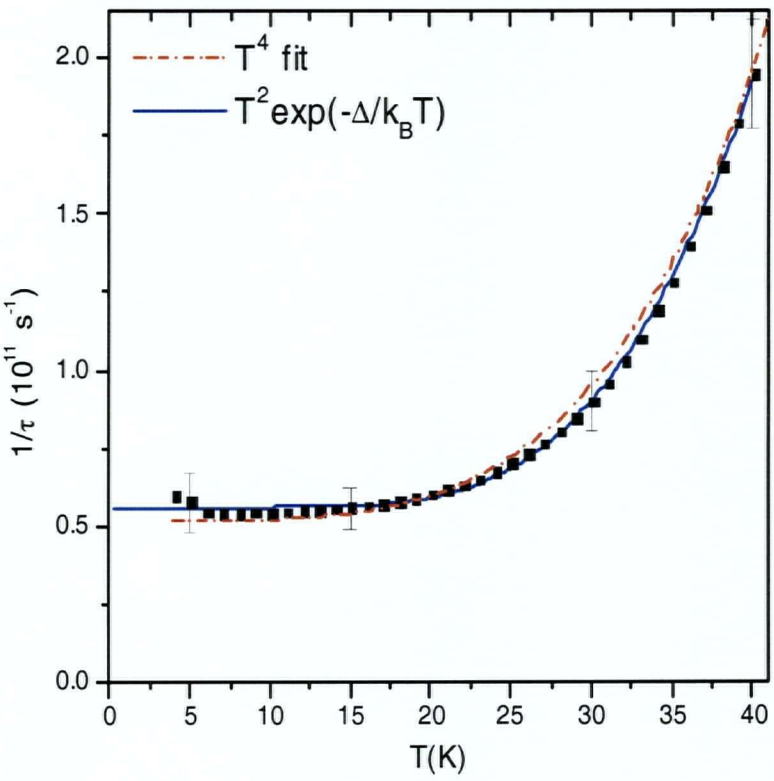

Figure 3.11: The scattering rate of thermally excited quasiparticles, as inferred from the width of Drude fits to the conductivity spectra.

the estimated errors shown in Fig. 3.11. Also shown (solid line) is a fit to the form $1/\tau(T) = A + BT^2 \exp(-\Delta_U/k_BT)$ with $A = 5.6 \times 10^{10}\mathrm{K}^{-2}\mathrm{s}^{-1}$, $B = 9.8 \times 10^{8}\mathrm{K}^{-2}\mathrm{s}^{-1}$, and $\Delta_U/k_B = 97$ K. This form fits the data a little better and comes from umklapp quasiparticle-quasiparticle scattering which will be discussed in the next section.

3.4 Discussion

To discuss the data further, we divide the conductivity spectra into two regimes. In the range below about 20 K where the width of the peak in $\sigma_1(\omega)$ is narrow and nearly temperature independent, studies of samples over a wide range of purities indicate that this regime is governed by scattering of quasiparticles by impurities or other defects [19, 51]. Within the 2-fluid model used, the half width of the lines is the

transport scattering rate, and is found to be constant. This rate would correspond to a long mean free path of 4 μm if one takes the Fermi velocity to be $v_F = 2 \times 10^7 cm/s$. In this particular two fluid model, the only source of temperature dependence in the low temperature microwave conductivity is the density of the thermally excited quasiparticles, which increases linearly with temperature.

Parameterizing the normal fluid response in this way, with a temperature dependent density and a scattering rate, has been partly justified by calculations of the microwave conductivity of a $d_{x^2-y^2}$ superconductor [12]. However as alluded to in chapter 1, it is not so obvious that a temperature independent scattering rate is expected for impurity scattering of these thermally excited quasiparticles near the nodes, since they differ from free carriers at an ungapped Fermi surface. Hirschfeld *et al.* point out that elastic impurity scattering in this situation should lead to a frequency and temperature dependent scattering rate because of the restricted phase space into which the quasiparticles at the nodes can scatter [12, 18]. With this conflict between theory and the phenomenological model in mind, we will make some more detailed comparisons between the microwave conductivity data and the recent theoretical situation.

The transport properties of a d-wave superconductor have been studied in some detail over the last few years [21, 12, 52, 18, 53, 54, 55]. At low temperatures the main physics is that of the interaction of quasiparticles with impurities, and this is particularly important for a d-wave state because the presence of impurities has a strong impact on the quasiparticle excitation spectrum near the nodes, particularly in the limit of unitary scattering. Impurities in a d-wave superconductor produce a band of impurity states with a width γ, thus giving the superconductor a non-zero density of states at the Fermi level. A consequence of these states is a conductivity limit at low frequency as $T \rightarrow 0$, first predicted by P.A. Lee [21]. This residual conductivity is independent of impurity concentration, and has been observed by Taillefer *et al.* in the electronic thermal conductivity as shown in Fig 1.9 [20]. Such

limiting behaviour has not been observed for the case of the microwave conductivity, and will not be our concern here. Instead, we are interested in the behaviour of this conductivity as temperature and frequency are increased, as this is what our cavity perturbation data covers.

A well studied problem is that of impurity scattering at temperatures and frequencies below the impurity bandwidth γ, in the unitary scattering limit (scattering phase shift $\rightarrow \pi/2$). In this limit the impurity bandwidth is given roughly by $\gamma \sim (\Gamma\Delta)^{1/2}$ where Δ is the magnitude of the gap and Γ is the elastic scattering rate that the impurities would contribute to the normal state resistivity. For $\omega, T < \gamma$, where the transport properties are dominated by this impurity band, it has been shown that both σ_1 and λ vary as T^2 [12, 52]. This quadratic behaviour has been seen in Zn-doped samples of $YBa_2Cu_3O_{6.95}$ [56, 19]. However, Zn substitution for planar Cu's is the only impurity that has been reported to lead to behaviour expected of unitary scattering. Ni substitution for Cu, Ca substitution for Y, and chain oxygen vacancies all have much weaker effects, even at defect levels of 1% or more [19]. The previous generation of YSZ-grown crystals showed very slight curvature in $\lambda(T)$ and $\sigma_1(T)$ below 4 Kelvin and our data on a higher purity crystal shows no hint of T^2 temperature dependence down to 1.2 Kelvin. The linear penetration depth seen down to the lowest temperature leads us to think of the opposite limit for the strength of the scattering present in the studied sample, namely the Born limit.

For impurity scattering in the Born limit, the crossover energy scale is exponentially small, so one does not expect to see localization effects and a limiting conductivity until well below 1 Kelvin. For the microwave measurements presented here we are also not necessarily at low enough *frequency* to observe any simple limiting behaviour. So, we compare our results qualitatively to numerical calculations performed in the Born limit by Hirschfeld *et al.* shown in Fig 3.12 [18].

The numerical results show that at very low frequency $\sigma_1(T)$ rises rapidly from the universal zero temperature limit to a much larger conductivity that depends upon

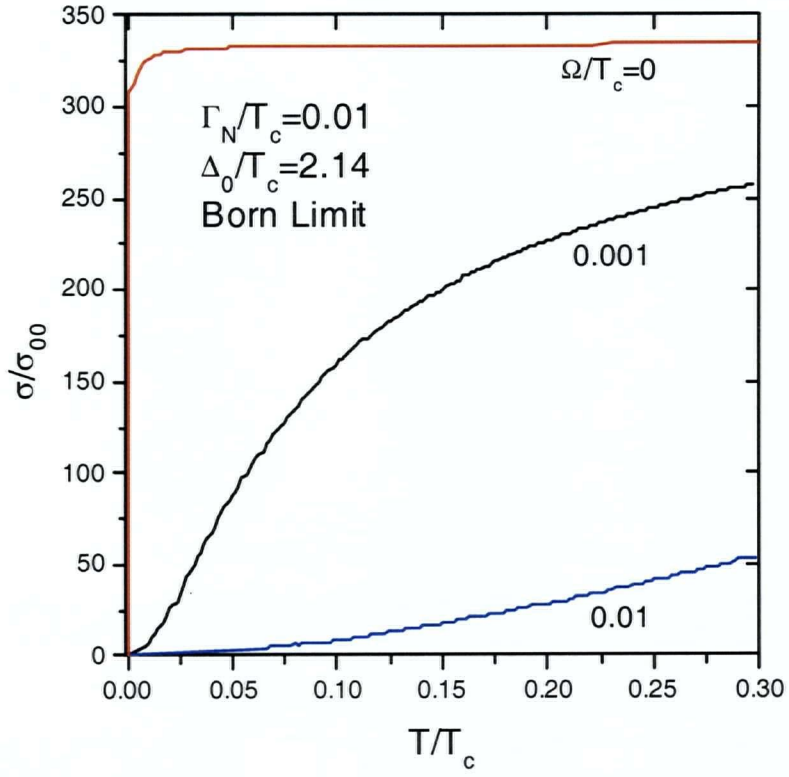

Figure 3.12: Numerical calculation of conductivity in the Born limit. σ_{00} is $\sigma_1(T \rightarrow 0)$, and Ω is the measurement frequency [18].

the impurity scattering rate. It remains fairly temperature independent until inelastic scattering processes become important. At higher frequencies $\sigma_1(T)$ becomes smaller and moves through a whole range of behaviours, varying from mostly sub-linear in T at low frequency, through a quasi-linear temperature dependence at intermediate frequencies, to a faster than linear temperature dependence at high frequencies. Figure 3.13 shows behaviour in the measured microwave conductivity that is similar to this Born limit result in some of its qualitative features.

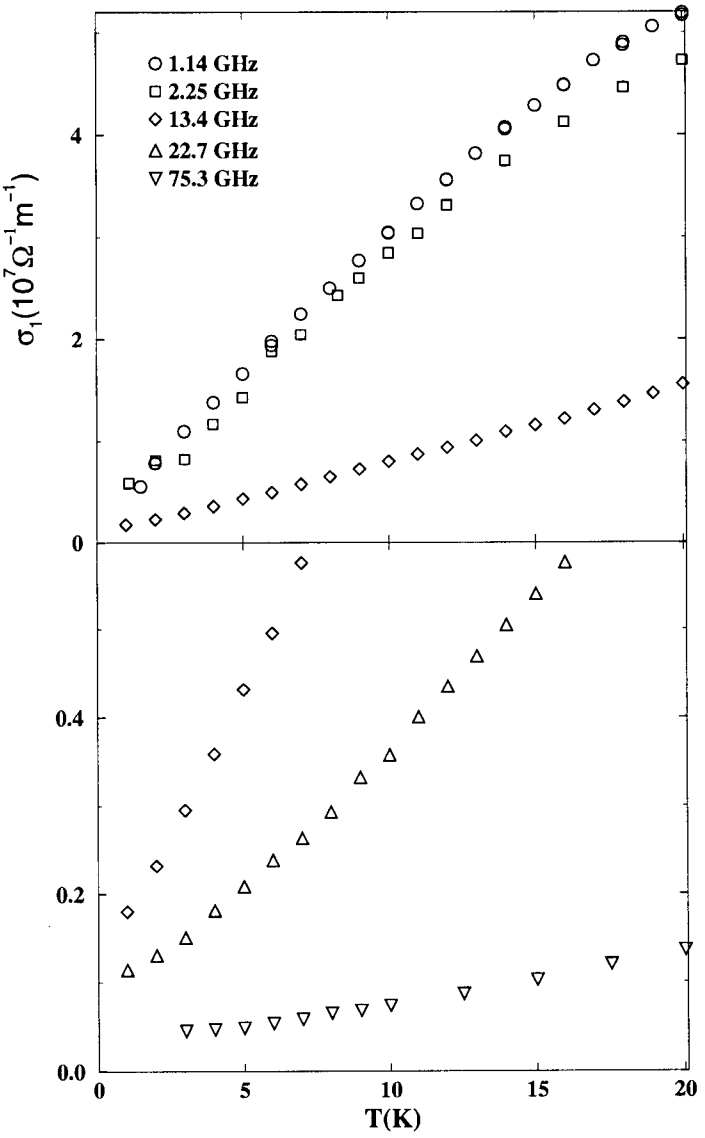

Figure 3.13: Expanded scale views of the temperature dependence of the measured microwave conductivity below 20 K.

Here we see clearly for the first time that the linear behaviour of $\sigma_1(T)$ is an intermediate behaviour, albeit one that survives over a substantial range of frequency and temperature. The evolution in the shape of $\sigma_1(T)$ at low T clearly falls outside of our phenomenological model, which would have predicted a linear temperature dependence at all of the frequencies shown in Fig. 3.13. That is, if $\sigma_1(\omega)$ were really Drude-shaped with a temperature independent width, then $\sigma_1(T)$ would exhibit

the same temperature dependence at all frequencies; namely, the linear temperature dependence of the normal fluid density.

At the lowest frequencies the data does indeed move towards sub-linear as expected in the Born limit. However, one perhaps important difference from Hirschfeld's calculations is that the trend does not continue below 2 GHz. The data stops evolving towards the expected low frequency behaviour, which is a rapid leap upwards to a constant value. The reason for this is not obvious but it does point to the possibility that the impurity scattering strength could be close to the Born limit, nevertheless not quite there and intermediate phase shift calculations are needed. So we are left for the moment with qualitative features that seem only weakly in accord with Born limit scattering. Other features of the data echo the expectations of a conductivity spectrum with a Drude-like lineshape that has a temperature independent width; namely, the similarity in the 1 and 2 GHz curves and the relatively large frequency and temperature range over which $\sigma_1(T)$ is nearly linear in T. It is the latter aspects of the data that lead to the Drude model being a fairly good description of the conductivity spectra.

Although the foregoing discussion indicates that the $\sigma_1(\omega)$ spectra cannot be perfectly Drude shaped, there is still a characteristic width to the peaks that is well parameterized by the Drude fits. Thus, the plot of scattering rates shown in Fig. 3.11 provides a reasonable measure of the narrowness of the peak at low temperature and its rapid broadening above 20 K. Just above 20 K, the initial onset of this increase in scattering appears to be at least as rapid as T^4 and must rise even more quickly at higher temperatures in order to meet the width observed in the normal state far infrared measurements. A rapid temperature dependence of the quasiparticle scattering time would be expected in a situation where the inelastic scattering comes from interactions that become gapped below T_c. Quinlan *et al.* have studied a model in which quasiparticle lifetimes are associated with spin fluctuation scattering with a gap in their spectrum [57]. They have found that at temperatures well

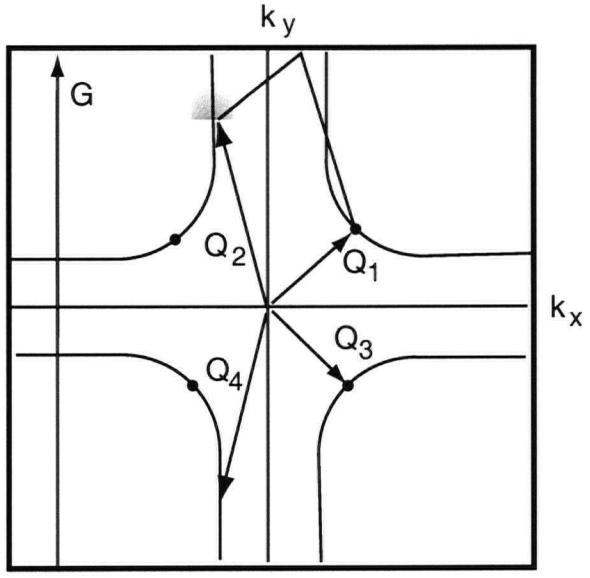

Figure 3.14: Fermi surface of a CuO_2 plane, showing initial wavevectors Q_1, Q_2, and scattered wavevectors Q_3, Q_4 associated with umklapp scattering.

below T_c, the quasiparticle lifetime increases as T^3 and even faster than this as T_c is approached. In a comparable temperature range, the transport scattering rate that we extract from the width of $\sigma_1(\omega)$ is closer to T^4. This is about one power of T faster than the lifetime calculations based on a gapping of the spin fluctuation spectrum. To understand the differences, we have to realize that the quasiparticle lifetime calculated by Quinlan *et al.* can in principle differ from the electrical transport lifetime. What is experimentally extracted through the microwave conductivity is the transport lifetime, which differs in the way it is weighted over the single-particle lifetime. In the latter, all scattering processes are equally weighted, but in the electrical transport lifetime backscattering has a much larger effect on the current than does small-angle scattering. These effects have been considered by Walker and Smith [58], for the transport lifetime arising from quasiparticle-quasiparticle scattering in a d-wave superconductor, assuming BCS-like quasiparticles[1]. They note that if spin fluctuation scattering is an important source of inelastic scattering at high tempera-

[1]the arguments given here follow closely those given in Walker and Smith [58]

tures, their influence should decrease in the superconducting state with the decrease in spin susceptibility which is expected below T_c. They argue that in a regime below T_c, quasiparticle-quasiparticle scattering should then become more important.

At temperatures which are small compared to the maximum gap, the thermally excited quasiparticles occupy states close to the $d_{x^2-y^2}$ gap nodes on the Fermi surface. In scattering events involving two such thermally excited nodal quasiparticles, the outgoing quasiparticles too have momentum vectors lying close to the gap nodes in order to conserve energy. From the geometry of the Fermi surface shown in Fig. 3.14, it is clear that these processes must have $G = (0, 0)$, and are *normal* processes. The current associated with nodal quasiparticles is proportional to the sum of all their momenta. For normal processes, the momentum sum is not affected, and therefore there is no contribution to the transport relaxation rate. Instead, the transport lifetime is determined by quasiparticle-quasiparticle umklapp processes which do change the total quasiparticle momentum. Umklapp processes are forbidden unless the energy of an incoming quasiparticle is greater than some threshold energy Δ_u, which is some fraction of the maximum gap. Fig. 3.14 shows schematically one such process. Q_1 is the momentum of a nodal quasiparticle whose relaxation rate is being considered, and Q_2 is the lowest energy quasiparticle that can enter a collision with the nodal qusiparticle in an umklapp process. Its energy is Δ_U. Momentum conservation requires $Q_1 + Q_2 = Q_3 + Q_4 + G$ where G is a non zero reciprocal lattice vector.

The umklapp process scattering rate is determined by the mean number of quasiparticles with momentum Q_2, i.e $\exp(-\Delta_U/k_BT)$ for $k_BT \ll \Delta_U$. Other quasiparticles in the neighborhood of Q_2 contribute too, as shown in the shaded area of Fig. 3.14, and when their contribution is included Walker and Smith obtain an expression of the form,

$$\frac{1}{\tau_{el}} = CT^2 \exp(-\Delta_U/k_BT) \tag{3.1}$$

where C is a constant, and the T^2 prefactor has been arrived at by the averaging

of contributions from quasiparticles in the vicinity of Q_2. A fit made to this form, where a constant elastic scattering rate has been added is shown in Fig. 3.11. With a value for the umklapp gap of $\Delta_U/k_B = 97$ K, it can be seen that within experimental error this model seems to capture the rapidly varying temperature dependence of the inelastic scattering contribution to $1/\tau$.

Chapter 4

$\hat{c}$-axis Electrodynamics of $YBa_2Cu_3O_{6.95}$

Studies of the $\hat{c}$-axis properties in the cuprates are of considerable importance in the quest to understand the mechanism of high-Tc superconductivity. The materials are highly anisotropic, and the degree of anisotropy varies significantly between different materials and with doping. The simplest measure of anisotropy, the DC resistivity, can be orders of magnitude higher along the $\hat{c}$ direction than it is within the planes, and displays a range of behaviour as a function of doping [15]. The measured magnitude of the normal state $\hat{c}$-axis conductivity is far smaller than band structure predictions for all cuprates, and it is likely that electron transport between layers is intrinsically incoherent [1]. Even in $YBa_2Cu_3O_7$, the $\hat{c}$-axis mean free path has been estimated to be less than the interlayer spacing, l_c, and it is difficult to think of coherent band like transport along the $\hat{c}$-axis [60].

A number of theories have tried to treat the incoherence, and these can be separated into Fermi liquid and non-Fermi liquid models. In the Fermi liquid scenarios, emphasis is placed on the dynamics of the quasiparticles, and different scattering dependencies across the fermi surface [61]. Among the non-Fermi liquid approaches has been the idea that transport could involve particles carrying unconventional spin and charge quantum numbers. Of particular interest has been Anderson's notion of spin charge separation in 2-dimensions which naturally explains the 'confinement' of single

[1] By this we mean a mean free path that is shorter than the interlayer spacing, a fact borne out by what is seen as a very broad $\hat{c}$-axis conductivity spectrum up to 800 cm^{-1} [59]

charge carriers to the planes in the normal state [2]. On entering the superconducting state, however, the pairing of carriers would allow for coherent pair tunnelling, and lower their energy. Anderson went one step further to propose that this 'interlayer tunnelling' model (ILT) is the mechanism which provides all the condensation energy responsible for high temperature superconductivity. Experimental work in Tl-2201, and Hg-1201 has now shown that interlayer tunnelling of *pairs* is two orders of magnitude too weak to account for the condensation energy of these materials [62, 63], and the observation of single particle confinement in the normal state is still an open question.

In this chapter we try to probe interlayer transport properties with our microwave techniques to better understand the evolution of charge transport on entering the superconducting state. We study $YBa_2Cu_3O_{6.95}$, which is one of the least anisotropic members of the family, and has a resistivity anisotropy less than a factor of 50 [64]. The small anisotropy and very thin crystals of this material have made electrodynamic measurements aimed at extracting $\hat{c}$-axis properties extremely difficult [42, 26]. In what follows we address the difficulties and present ways around them to get an accurate measure of the $\hat{c}$-axis microwave conductivity and penetration depth in optimally doped YBCO.

4.1 Experimental Issues

Surface impedance measurements involve placing a sample in microwave magnetic fields $\vec{H}_{AC}$, where the currents induced in the surface must form closed loops. In principle, by changing the geometry or orientation of the sample one can perform measurements that contain different admixtures of ab-plane and $\hat{c}$-axis currents and then extract the surface impedance in different directions. This can be achieved by rotating a sample or by measuring samples cut with different orientations. Measurements that involve rotating the sample [42, 26] can have severe problems due to

changing demagnetizing factors and changing current distributions. If one is working with thin rectangular samples, which is the most common situation with crystals of cuprate superconductors, there is a huge change in demagnetizing factors if the sample is rotated from $\vec{H}_{AC} \parallel \hat{c}$ (Fig. 4.1a, planar currents only) to $\vec{H}_{AC} \perp \hat{c}$ (Fig. 4.1b, combination of planar and $\hat{c}$-axis currents). Even if the sample is not very thin and the demagnetizing factors can be dealt with, changes in the ab-plane current distribution can bring poorly controlled uncertainties into such procedures for extracting the $\hat{c}$-axis electrodynamics.

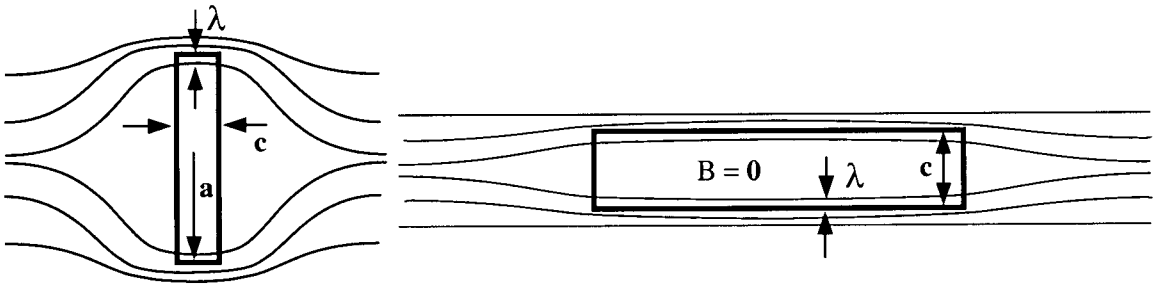

Figure 4.1: $\vec{H}_{AC} \parallel \hat{c}$ (left), $\vec{H}_{AC} \perp \hat{c}$ (right).

Our approach to obtaining the $\hat{c}$-axis surface impedance at optimal doping relies on the methods of cleaving and polishing samples. Each will be discussed separately, and then compared.

4.1.1 Cleave Method

For the cleaving technique we use the fact that thin crystals of $YBa_2Cu_3O_{6.95}$ cleave very cleanly in the [100] and [010] directions, Fig. 2.4. The surface resistance or penetration depth is initially measured with the microwave magnetic field lying in the plane of the thin slab, measuring with both $\vec{H}_{AC} \parallel \hat{b}$ ($\hat{a}, \hat{c}$ currents) and $\vec{H}_{AC} \parallel \hat{a}$ ($\hat{b}, \hat{c}$ currents). The contribution due to $\hat{c}$-axis currents is then increased by cleaving the slab into a set of narrow needles which is remeasured with $\vec{H}_{AC}$ lying along the axis of the needles. This technique is particularly reliable because it has no significant

change in demagnetizing factors, no change in the distribution of *ab*-plane currents, and there is no need to compare different samples. With this sequence of experiments and measurements of the sample's dimensions it is straightforward to extract the surface impedance. This is done by noting that the effective surface impedance is simply the weighted sum of the surface impedances;[2]

$$Z^s_{eff} = \frac{l_{ab} Z^s_{ab} + l_c Z^s_c}{l_{ab} + l_c} \tag{4.1}$$

where the lengths l_{ab} and l_c are that of the sides which are perpendicular to the applied field.

The $\hat{c}$-axis magnetic penetration depth was measured in this way by Saeid Kamal in a superconducting loop-gap resonator at 1.1 GHz [65, 66, 35]. The measurements of surface resistance in the $\hat{c}$-direction $R_{sc}(T)$ were done at 22.7 GHz. The samples used for cleaving were crystals of $YBa_2Cu_3O_{7-\delta}$ grown in yttria-stabilized zirconia crucibles, then detwinned and annealed to set the oxygen content [67].

4.1.2 $\hat{c}$-axis surface impedance of $YBa_2Cu_3O_{6.95}$ obtained by cleaving

Fig. 4.2 shows the temperature dependence of the penetration depth $\Delta\lambda_c(T) = \lambda_c(T) - \lambda_c(1.2K)$ extracted in the manner described above. Instead of the linear behaviour seen in both directions in the *ab*-plane, the temperature dependence is close to quadratic, with a power law of $\Delta\lambda(T) \propto T^{2.1}$ giving a good fit to the data up to about 40 K. These microwave results can be combined with far infrared measurements of $\lambda_c(0)$ [59, 46] to produce the superfluid fractions shown in Fig. 4.3. A key feature of this figure is that in all three directions, the behaviour near T_c is consistent with 3D XY-like critical fluctuations. However, at lower temperatures, the superfluid

[2]Strictly speaking this is valid in the limit where the sample is well outside the thin limit which happens to be true at all times in our studies in this chapter. For YBCO at optimal doping the normal state skin depth in the plane is $\sim$ 2 μm, and along the $\hat{c}$-axis it is $\sim$16 μm at 100 K.

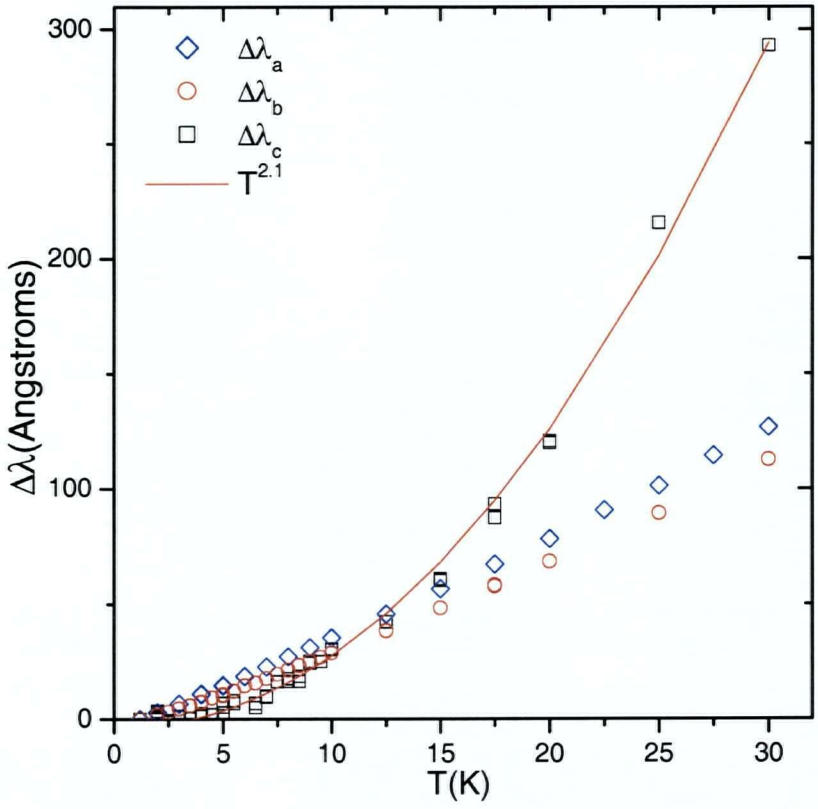

Figure 4.2: Anisotropic temperature dependence of the penetration depth in $YBa_2Cu_3O_{6.95}$ [68].

fraction in the $\hat{c}$-direction is very flat and shows no sign of the linear temperature dependence observed in the *ab*-plane. Furthermore, previous work has shown that this behaviour persists over a wide doping range, from underdoped ($\delta = 0.42$) to slightly overdoped ($\delta = 0.01$) [65]. This indicates that, despite the 3D XY critical behaviour near T_c, highly doped $YBa_2Cu_3O_{7-\delta}$ does not behave in the simplest manner one might expect for a *d*-wave pairing state in an anisotropic 3 dimensional metal with a superfluid stiffness[3] that is linear at low temperatures in all three directions [69, 70]. Strikingly similar behaviour has been reported by Shibauchi *et al.* for polished slabs

[3]Strictly speaking the superfluid density n_s is not measured directly by measurements of the penetration depth, rather it is tied to the effective mass m^* which is anisotropic in $YBa_2Cu_3O_{7-\delta}$. The term superfluid stiffness along different axes conveys this, however it is often customary to just talk about superfluid density where this distinction is implied.

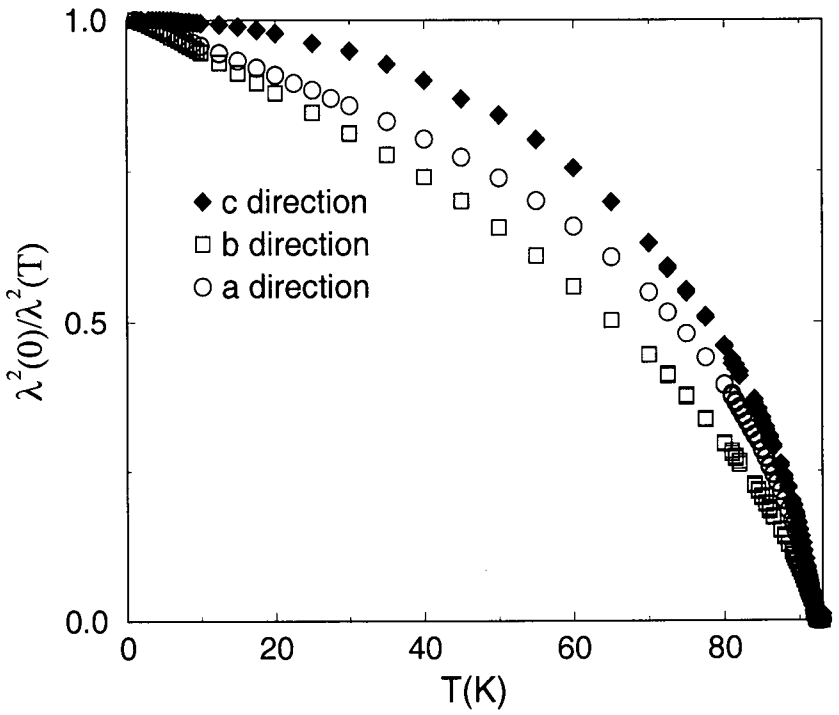

Figure 4.3: The superfluid fraction along the $\hat{c}$-axis of $YBa_2Cu_3O_{6.95}$ is qualitatively different from the behaviour seen in either direction in the *ab*-plane.

of $La_{1.85}Sr_{0.15}CuO_4$ [28], by Jacobs *et al.* for cleaved crystals of $Bi_2Sr_2CaCu_2O_{8+\delta}$ [71], and by Panagopoulos *et al.* for aligned powders of $HgBa_2Ca_2Cu_3O_{8+\delta}$ [72].

Fig. 4.4 shows measurements of $R_s(T)$ at 22.7 GHz performed on a thin plate with $\vec{H}_{AC} \parallel \hat{a}$. The dimensions of this crystal were (a,b,c) equal to 0.92mm, 0.88mm, and 18.5($\pm$1) μm. This orientation produces currents running across the face of the slab in the $\hat{b}$-direction, with a small contribution from currents running down the side of the slab in the $\hat{c}$-direction. The small change seen in $R_s(T)$ after cleaving the sample into three and then five needles is the increase in loss due to an increased $\hat{c}$-axis contribution. Except near T_c, the changes are extremely small which indicates that the surface resistance in the $\hat{c}$ direction $R_{sc}(T)$ is actually quite low. Since $R_s \propto \lambda^3(T)\sigma_1(\omega, T)$, we see that the increase in loss that might be expected from the much larger λ in the *c*-direction is in fact balanced by a rather low $\hat{c}$-axis conductivity.

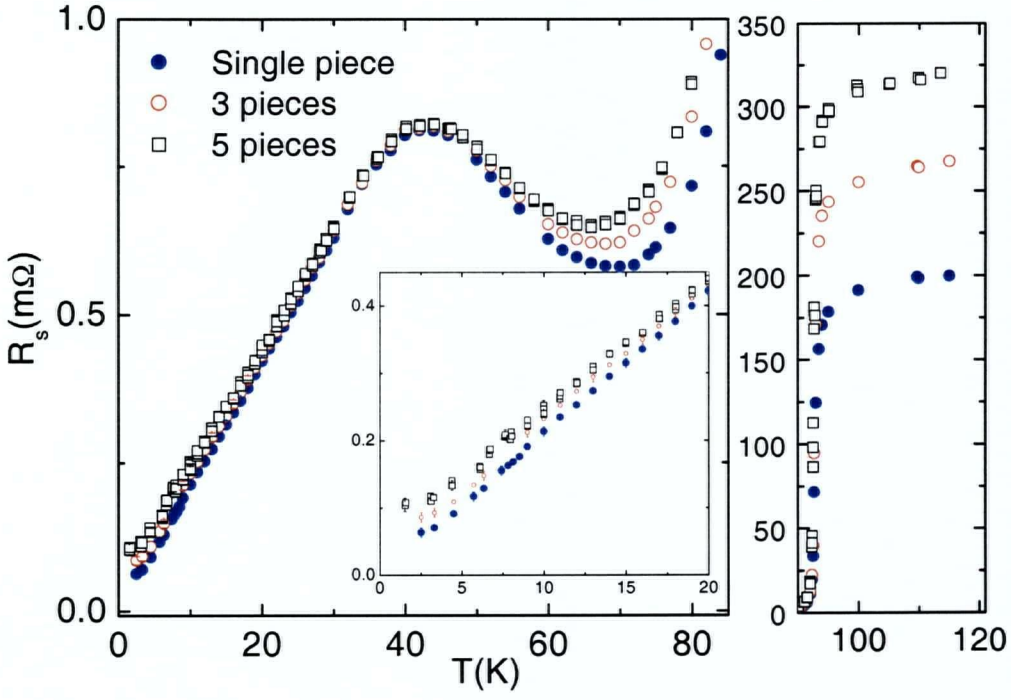

Figure 4.4: Surface resistance of $YBa_2Cu_3O_{6.95}$ sample along the b-direction after successive cleaves along the a-direction of the crystal. The extra loss is from an increased $\hat{c}$-axis contribution with successive cleaves.

The influence of $R_{sc}(T)$ is most clearly discernable above 60 K, and rather surprisingly there was some additional $\hat{c}$-axis loss appearing below 20 K. The small size of the effect observed here indicates that it would be difficult to unambiguously extract $R_{sc}(T)$ from the earlier techniques that involved changing the orientation of the sample [42, 26], since the effect of changes in current distribution can easily be larger than the change observed in this experiment.

Fig. 4.5 shows the surface resistance in all three directions (R_{sa}, R_{sb}, R_{sc}), extracted from the data in Fig. 4.4, plus a set of measurements to determine $R_{sa}(T)$. $R_{sc}(T)$ is very low and qualitatively different from that observed in either of the planar directions. The broad peak seen in the ab-plane R_s is caused by a very large peak in $\sigma_1(T)$ in both the $\hat{a}$ and $\hat{b}$ directions as already discussed in chapter 3. This increase in the ab-plane conductivity below T_c has been attributed to a rapid increase

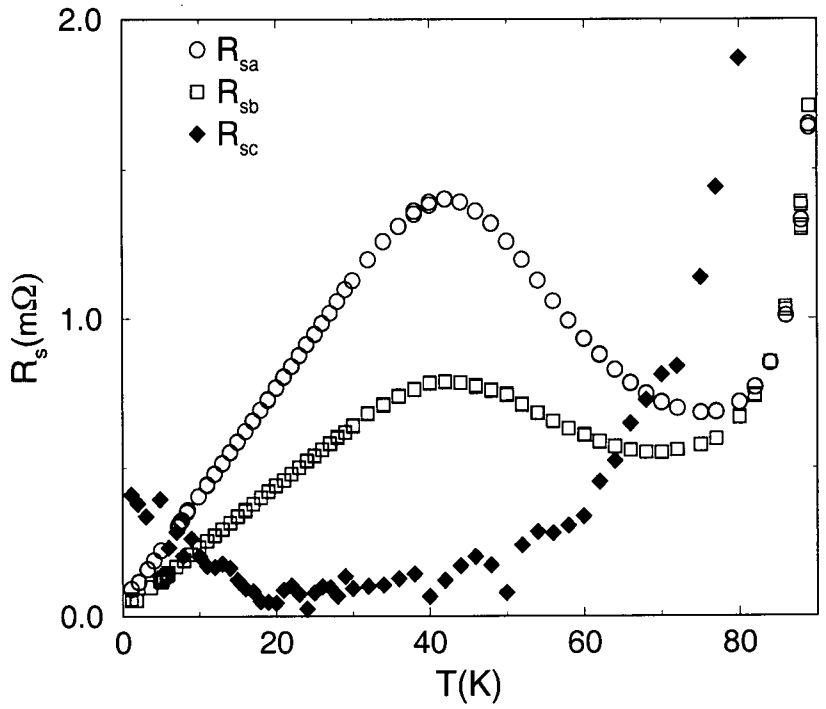

Figure 4.5: Surface resistance of $YBa_2Cu_3O_{6.99}$ along the three crystal directions.

in quasiparticle lifetime in the superconducting state [40], but the increase seems to be completely absent for carriers moving in the $\hat{c}$-direction. Instead, $R_{sc}(T)$ falls to low values below T_c.

Using the measurements of $\lambda_c(T)$, the $\hat{c}$-axis conductivity $\sigma_{1c}(T)$ can be extracted from this measurement of $R_{sc}(T)$. Because $R_{sc}(T)$ is so small, and rather surprising in shape, we repeated the measurements on a sample taken from a different crystal growth run and the conductivity from both sets of data is shown in Fig. 4.6.

In the normal state just above T_c, the $\hat{c}$-axis microwave conductivity of both crystals is about $6.3(\pm 2) \times 10^4\,\Omega^{-1}m^{-1}$, corresponding to a DC resistivity of $1.6\,m\Omega - cm$, which is in agreement with the lowest range of values reported for $YBa_2Cu_3O_{7-\delta}$ crystals in this range of oxygen doping [64]. The main uncertainty in this value comes from the uncertainty in the measured thicknesses of the samples, which were determined using an optical microscope. Below T_c, $\sigma_{1c}(T)$ falls rapidly, with no sign of the

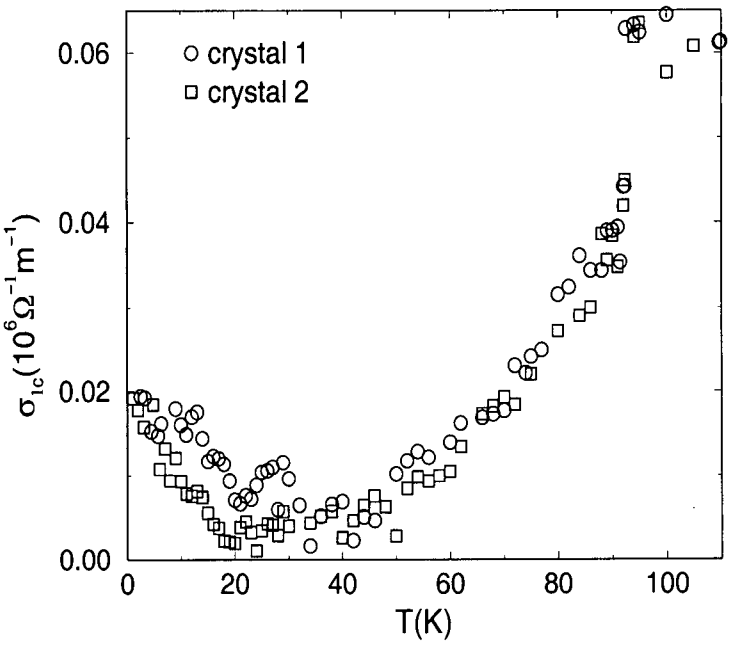

Figure 4.6: Microwave conductivity of two samples along the c-direction obtained using the cleave technique.

peak observed in the ab-plane. The qualitatively different temperature dependencies in the two directions leads to an anisotropy in the conductivity of almost 10^4 by 30 K! This is seen clearly in Fig. 4.7 where we have plotted the $\hat{a}$-axis conductivity together with the $\hat{c}$-axis conductivities obtained here and in the next section. From Fig. 4.4 we can see that the magnitude of the $\hat{c}$-axis contribution leading to the conductivity below 40 Kelvin is extremely small and the noise in the data makes the extraction difficult. However, the data seems to support the conclusion that the measured $\sigma_{1c}(T)$ in these two crystals drops monotonically below T_c and has a non zero low temperature limit. Thus the $\hat{c}$-axis never completely exhibits insulating behaviour. At 10 K the value of $\sigma_{1c}(T)$ at 22 GHz is $10^4\Omega^{-1}m^{-1}$, which is close to the residual conductivity of $\sigma_{1c}(T = 10\ K) \approx 5 \times 10^3\Omega^{-1}m^{-1}$ at 100 cm^{-1}, the low frequency limit of far infrared $\hat{c}$-axis measurements [59].

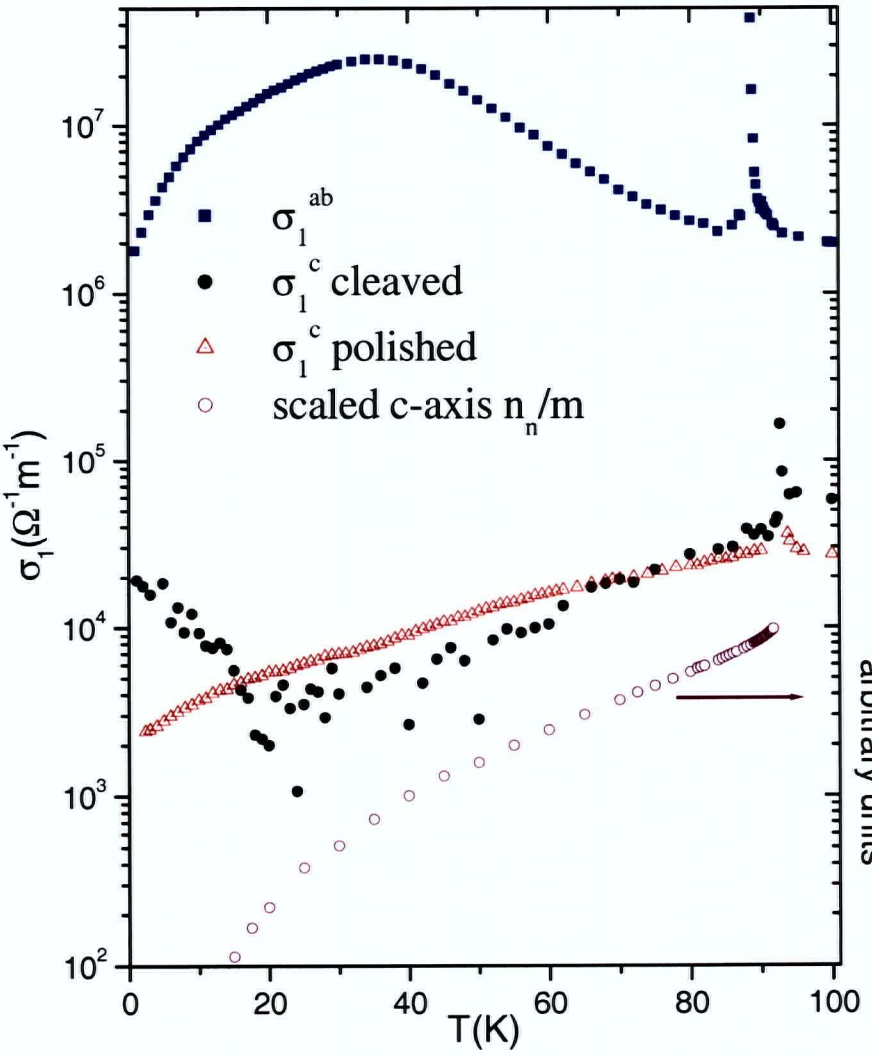

Figure 4.7: Semi-log plot of a, and $\hat{c}$-axis conductivities of $YBa_2Cu_3O_{6.95}$. Also plotted is the scaled normal fluid density obtained from the $\hat{c}$-axis penetration depth.

4.1.3 Polishing Method

The difficulties alluded to in the measurements above has lead us to approach the problem of measuring the $\hat{c}$-axis electrodynamics by using samples with larger $\hat{c}$-axis faces. Unfortunately the cleaving technique is not successful for crystals with thicknesses above 20 μm. The samples shatter during the attempt.

We have thus resorted to the method of polishing samples, which is schematically shown in Fig. 4.8. The polishing is done on one face containing the $\hat{c}$-axis of the crystal, and at the final stage before a measurement, the crystal is etched in 0.5 percent solution of Bromine in Ethanol [4]. As illustrated, polishing is able to reduce the contamination from the *ab*-plane and it is possible to get at the $\hat{c}$-axis properties. However, the results of the previous section, Fig. 4.5, show that even with polishing, the contribution to R^s_{eff} can be significant due to the much larger value of R_s in the planes at temperatures below 70 Kelvin. In an attempt to correct for the remaining planar contamination it is necessary to make at least two measurements, with varying lengths along the planar direction. This requires two steps of polishing, one to obtain a sample as shown in Fig. 4.8(b) and then a further polish to obtain a sample shown in Fig. 4.8(c).

The availability of crystals with large $\hat{c}$-axis faces is a major issue with this technique. The majority of the crystals that were worked with eventually disintegrated during the steps described in chapter two, largely due to stacking faults that are common to thick $\hat{c}$-axis samples of YBCO. With persistence, an optimally doped crystal was prepared for the measurements to be described. It was grown in a barium zirconate crucible, and under polarized light no evidence was seen of stacking

[4]This removes dislocations which might have been introduced during the polish, and mostly restores the intrinsic microwave response [39]. For the $\hat{c}$-axis this is even more true than for the *ab*-plane response due to the penetration depth being over 1 micron for optimally doped YBCO. For $\hat{c}$-axis studies on underdoped samples, to be discussed in the next chapter, the penetration depth exceeds tens of microns, and the polishing is not a concern.

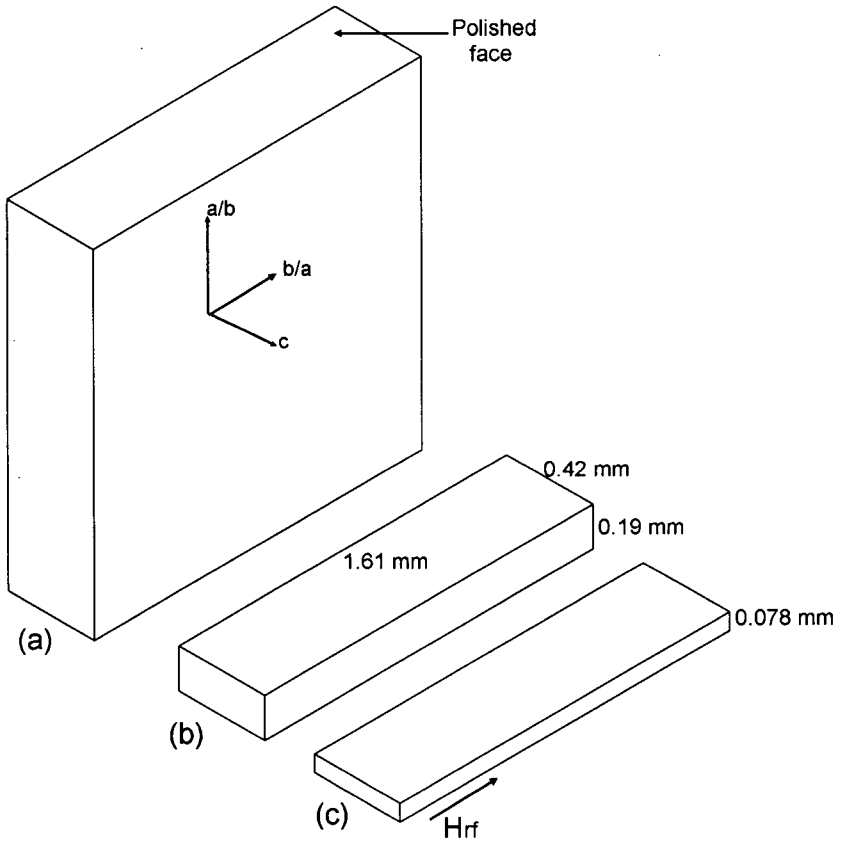

Figure 4.8: 2-stage polishing sample to remove large planar contribution to microwave measurements.

faults. One face was used for the polishing during two steps of thinning. It measured 1.61×0.42×0.193 millimeters after the first stage, and 1.61×0.42×0.078 millimeters after the second. A photograph of the crystal taken during the polishing is shown in Fig. 4.9.

The crystal was studied using our 22.7 GHz cavity, and the raw measurements for the field applied along the long planar direction are shown in Fig. 4.10. From these two measurements we can clearly see the effect of the large *ab* plane surface resistance in the data. To extract the surface impedance along the $\hat{c}$-axis, the difference in these two curves should give us a measure of the planar contribution, and hence be subtracted from the data. Before this can be done, it should be noted that the aspect ratios of

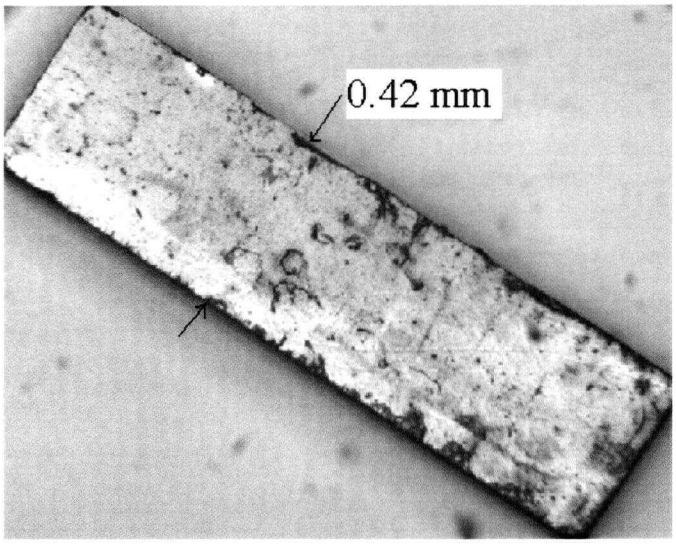

Figure 4.9: ac face of sample used to measure $\hat{c}$-axis properties.

the crystal were such that it can be important to consider demagnetization effects on the faces parallel to the applied field. The reason this was considered is that the magnitude of the changes in $1/Q$ of the cavity is proportional to the loss per cycle of the sample, and this is proportional to the surface resistance and the squared current density. An enhanced parallel component of the field, given by $H_p = H_{appied}/(1-N)$, where N is the demagnetization factor, leads to a larger apparent $\Delta(1/Q)$ by a factor of $1/(1-N)^2$. This could be different between the two different aspect ratios in the measurements above, and we will estimate this now.

For rectangular shapes in an applied magnetic field, London's equations cannot be solved analytically, and we resort to using known solutions for an oblate ellipsoid [73]. Although our samples were rod like, we'll assume they are ellipsoidal, with semi-major and minor axes given by the dimensions of the crystal. For the applied field along the long direction, which was our 1.61 mm planar direction, the demagnetization factor was calculated as $N = 0.045$ and $N = 0.020$, for the sample being 0.19 mm and 0.078 mm thick respectively. These are very small demagnetization factors, which is what was expected after measurements on a Pb-Sn sample were made of similar aspect

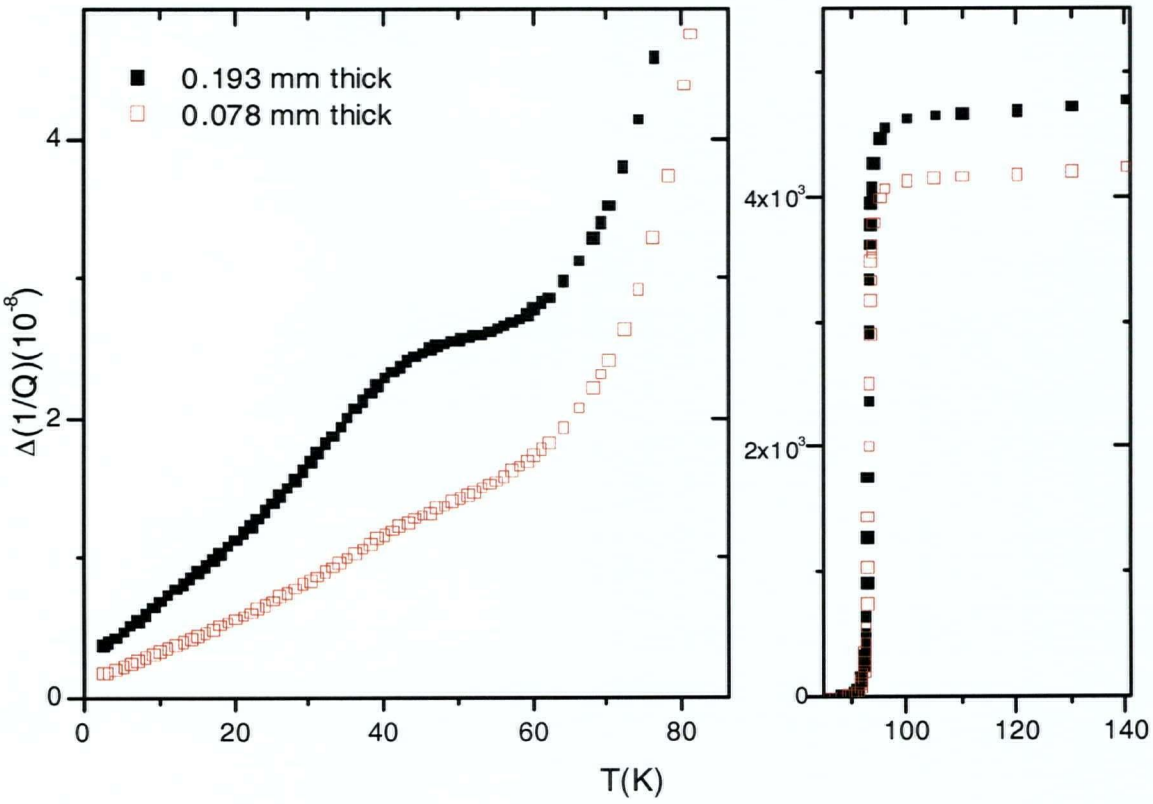

Figure 4.10: Raw data on optimally doped sample after two rounds of polishing.

ratio. However between the two measurements a 5 % factor can be present due to the differences in demagnetization, so we have performed the extraction calculation with and without this correction.

4.1.4 $\hat{c}$-axis surface resistance and conductivity of $YBa_2Cu_3O_{6.95}$ obtained by polishing

The raw data in the previous section was analyzed using equation 4.1, to obtain the surface resistance along the $\hat{c}$-axis. This is shown below in Fig. 4.11, where we have both included and ignored demagnetization effects. It is clear from the figure that these effects were minimal, and there is little appreciable difference in the overall shape of R_{sc}. The surface resistance obtained in this way agrees well with the mea-

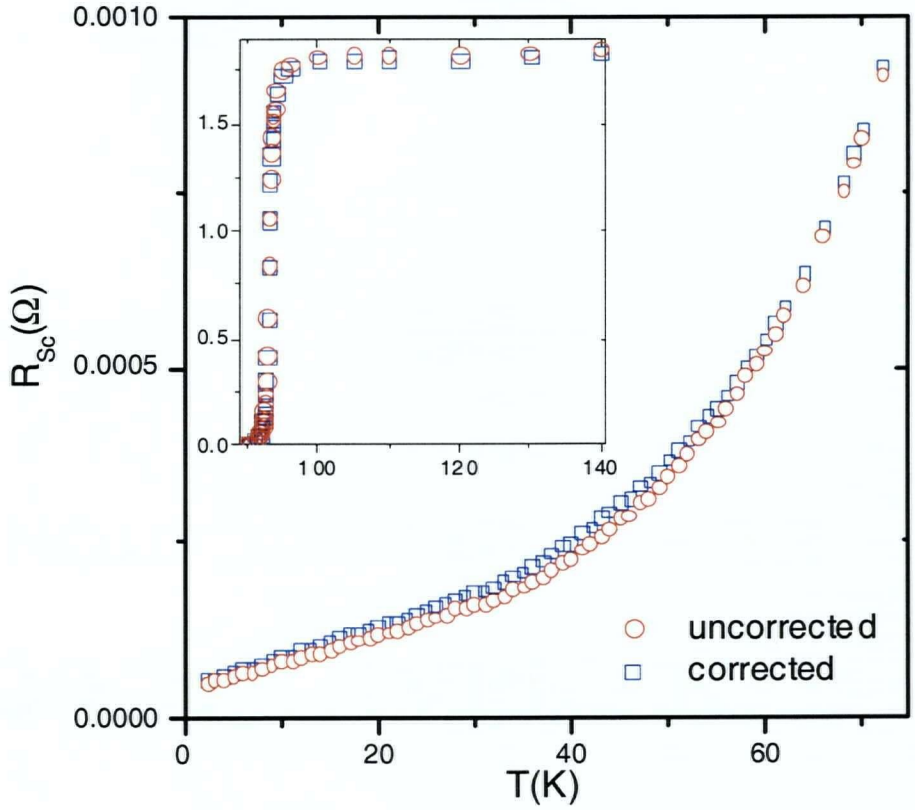

Figure 4.11: $\hat{c}$-axis surface resistance obtained by polishing.

surements of the previous section in that the $\hat{c}$-axis surface resistance drops rapidly below T_c and shows no sign of an underlying conductivity peak which gives the in-plane surface resistance its distinct shape, Fig. 4.5. To extract the conductivity we need measurements of the surface reactance, which was not measured accurately at low temperatures using our experimental setup at the time. The frequency instability was simply too much below T_c to get an accurate temperature dependence. Near the transition, however, the data agreed with earlier $\hat{c}$-axis penetration depth measurements and this earlier data set was used to calculate the conductivity [35].

The $\hat{c}$-axis conductivity extracted from these measurements is shown in Fig. 4.12. $\lambda_c(0)$ was taken as 11000 $\mathring{A}$. The data again is insensitive to the subtraction and shows a monotonic T-dependence up to T_c. The value of the conductivity at 100 K is about $2.7(\pm 0.3) \times 10^4\,\Omega^{-1}m^{-1}$ which is in very good agreement with literature values

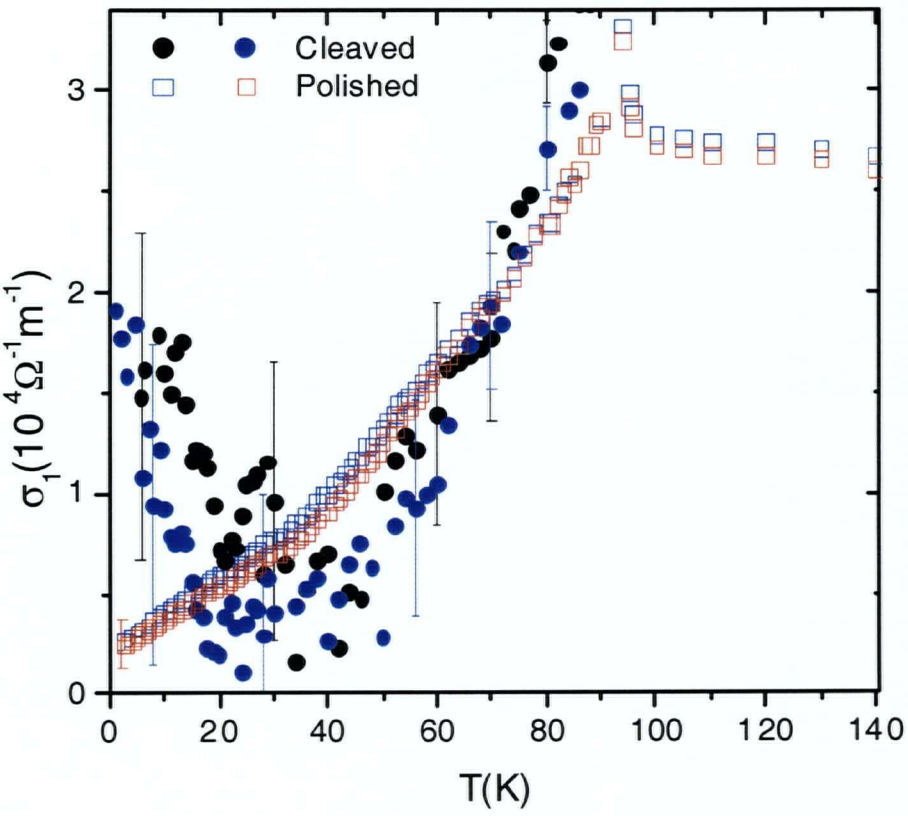

Figure 4.12: $\hat{c}$-axis conductivity of $YBa_2Cu_3O_{6.95}$, obtained by polishing method.

for optimally doped YBCO [64]. Also plotted is the conductivity of the two crystals measured by cleaving, showing the large uncertainties associated with subtracting very small differences. The new data set shows no hint of an upturn in the conductivity below 20 K, but still appears to show a finite residual conductivity. This data does support our earlier observation that the electrical conductivity remains very small out of the planes while entering the superconducting state.

4.2 Discussion

To discuss the data we will focus on the superfluid behaviour first. The $\hat{c}$-axis superfluid response has been the subject of recent theoretical study by Xiang and Wheatley [74, 75], and by Radtke *et al.* [69]. For an anisotropic 3D metal with a weak momen-

tum dependence of the interlayer hopping integral, the superfluid density should have a similar form to that in the planes. For the $d_{x^2-y^2}$ state, this means a linear low temperature dependence. This is in contrast to our observation of a near T^2 behaviour in $YBa_2Cu_3O_{6.95}$ for temperatures up to 40 K. Early work by Jacobs *et al.* [71] on $Bi_2Sr_2CaCu_2O_8$ showed a strong linear term in $\Delta\lambda_c$ at low temperature, in contrast to more recent work by Broun *et al.* [76] on the same material. The earlier work failed to take account of finite size effects, which is the probable cause of discrepancy. The published data on other cuprate systems have been reviewed by Xiang *et al.* [75], and they find the polynomial behaviour of the low temperature $\hat{c}$-axis superfluid density to be common in the cuprates. In fact the temperature dependence of the superfluid density looks very similar in $YBa_2Cu_3O_{7-\delta}$ [65], $Bi_2Sr_2CaCu_2O_{8+\delta}$ [76], $La_{1.85}Sr_{0.15}CuO_4$ [28] and $HgBa_2Ca_2Cu_2O_{8+\delta}$ [72], despite substantial structural variations. This temperature dependence seems largely independent of wide variations in the degree of anisotropy, as measured by either the normal state transport anisotropy or the wide variation in $\lambda_c(0)$ across this set of materials. This argues against models of layered superconductors where the degree of anisotropy and structural details are correlated with the temperature dependence of the $\hat{c}$-axis superfluid density.

To understand the behaviour seen in the superfluid density Xiang and Wheatley [74] have pointed out the importance of the interplay between the d-wave order parameter symmetry, and the underlying Cu 3d-orbital based electronic structure. They note that the transfer of holes from plane to plane has to involve the Cu-4s orbitals shown in Fig. 4.13, and these overlap with the O-2p in the planes with a $d_{x^2-y^2}$ symmetry. A result of this is that the interlayer hopping matrix element $t_\perp$ will become dependent on the direction of the in-plane momentum $k_\parallel$, and take the form $t_\perp \propto (\cos k_x - \cos k_y)^2$ in a purely tetragonal system. In their model they assume BCS like quasiparticles and weak dispersion along the $\hat{c}$-axis. There is no scattering of the quasiparticle wavevector upon moving to the next layer, and coherence is inherently implied. The paramagnetic contribution to the superfluid tensor which

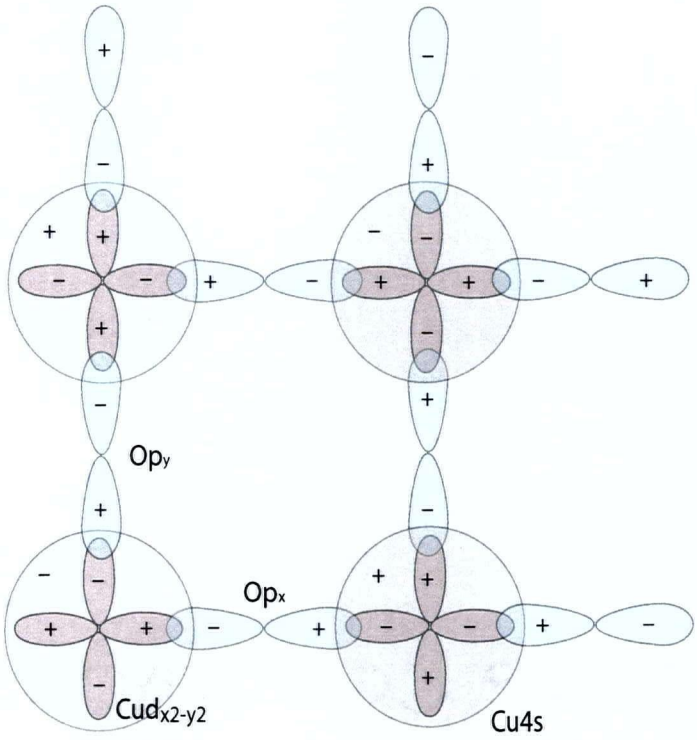

Figure 4.13: Cu-$3d_{x^2-y^2}$ and $4s$, and O-$2p_x$, O-$2p_y$ orbitals on each CuO plane.

is strongly temperature dependent in the ab-plane is weakened by the anisotropic hopping integral. For the case of perfect tetragonal symmetry where the gap nodes perfectly coincide with the zero's of $t_\perp$, the superfluid density takes on a T^5 low temperature behaviour. This has only been seen in the single layer mercury compound Hg1201 [77], and is expected in pure materials with low anisotropy so that coherent-interlayer hopping of electrons is the main contribution to the superfluid density. In the YBCO system, however, the presence of chains leads to the breaking of tetragonal symmetry, and it is has been suggested [75] that there will be finite matrix elements connecting different layers for quasiparticles at the nodes. This changes the low temperature dependence of the superfluid density to around $T^{2.5\pm0.5}$, in agreement with data in $YBa_2Cu_3O_{6.95}$ and $YBa_2Cu_3O_{6.99}$. For highly anisotropic systems, like $Bi_2Sr_2CaCu_2O_{8+\delta}$, or highly underdoped YBCO to be discussed in the next chapter, the coherent tunnelling component of the supercurrent along the $\hat{c}$-axis gets reduced

due to weaker coupling and it is likely that incoherent tunnelling [5] could dominate the low temperature behaviour of the superfluid density. This has been modelled by Radtke *et al.* [69] where they consider both direct hopping and assisted hopping by impurities, or some boson in the system. For example, this could be a phonon which would scatter electrons from one layer onto the next. The direct hopping contribution is highly unlikely, and leads to a linear T-dependence at odds with experiment. The assisted mechanism worked out numerically has a low temperature behaviour in the range T^2 to T^3 again in agreement with experiments. The data presented in this chapter cannot distinguish these models, and it is likely that a combination of mostly coherent and some incoherent (i.e diffuse) transport is present at high dopings.

We now turn to the ĉ-axis conductivity. The magnitude of $\sigma_{1c}(T)$ and its drop in the superconducting state suggest that single particle transfer between planes is weak and remains so even below T_c in $YBa_2Cu_3O_{6.95}$. These results resolve a conflict presented by earlier surface impedance measurements that showed a broad peak in $\sigma_{1c}(T)$ for highly doped YBCO, similar to the one observed in the *ab*-plane conductivity [42, 26]. Our results are also consistent with work done on optimally doped $Bi_2Sr_2CaCu_2O_{8+\delta}$ where the normal state anisotropy is several orders larger than in YBCO [78], and $\sigma_{1c}(T)$ is two orders of magnitude smaller in the superconducting state. Similar measurements have been done in $Tl_2Ba_2CaCu_2O_8$ and $Tl_2Ba_2CuO_6$ showing a drop in the ĉ-axis conductivity below T_c [79]. The absence of a peak in these data indicates that charge transfer between planes is not influenced by the development of the long transport lifetimes seen in *ab*-plane measurements below T_c, and is suppressed in materials with highly different anisotropies. As mentioned in the introduction, the low value's for the ĉ-axis conductivity in the normal and superconducting states could be due to a non-Fermi liquid ground state [2] where calculations have mainly been limited to normal state properties. We will thus have to consider a Fermi liquid description, and draw attention to the cold spot model of Ioffe and Millis

[5] here we mean that the tunnelling is diffuse, and the $k_{\|}$ is not conserved

[61]. In this phenomenological model which is partly supported by ARPES experiments, quasiparticle lifetimes have a strong dependence on their in-plane momentum $k_{\|}$ along the 2D Fermi surface, namely

$$\Gamma(k_{\|}) = \frac{\Gamma_0}{4}\sin^2(2\theta) + \frac{1}{\tau} \tag{4.2}$$

where θ is the angle of $k_{\|}$ relative to the nodal direction, and $1/\tau \propto T^2$. For the in-plane behaviour this model fits optical spectra well [79], and has a generic property that the effective scattering rate $1/\tau* \equiv \omega\sigma_1/\sigma_2$ is linear in energy if Γ_0 is temperature independent. The small ĉ-axis conductivity can be explained if we note that the interlayer hopping amplitude, $t_{\perp}$, is proportional to $(\cos k_x - \cos k_y)^2$, so that the conductivity is determined by those quasiparticles which are closer to the anti-nodal directions. These quasiparticles experience a very large scattering rate $\hbar\Gamma$ (since $k_{\|}$ is large, ~1 eV), and the ĉ-axis conductivity would be well into the dirty limit [80]. This model has been taken further by Xiang and Hardy [81] where they calculate the ĉ-axis conductivity based on this anomalous scattering across the Fermi surface and $k_{\|}$ dependent hopping. At temperatures above $T_c/2$ they find that the conductivity has a dominant T^3 term, and our data taken using the cleave method shown in Fig. 4.6 does fit this power law well. However, our newer measurements taken on polished samples show a different temperature dependence, Fig. 4.12, and it is likely that this mechanism alone is not sufficient to explain the data. This is certainly true for $Bi_2Sr_2CaCu_2O_8$ where coherent interlayer hopping which is a generic feature of this model is unlikely to be significant, nevertheless the ĉ-axis conductivity is very similar in shape to that of $YBa_2Cu_3O_{6.95}$.

Chapter 5

$\hat{c}$-axis penetration depth in $YBa_2Cu_3O_{6.35}$

Recent work by Liang *et al.* at UBC has resulted in the ability to dope YBCO to a level very close to the antiferromagnetic-superconductor (AFM-SC) boundary, ($\sim O_{6.35}$). The materials at this doping level are of particular interest, and provide a means to study superconductivity as it emerges from the antiferromagnet, where many theories make definitive predictions. The AFM-SC region has however been a difficult region to study, mainly due to the difficulty of preparing chemically homogeneous single crystals at low dopings, a requirement in resolving the intrinsic physics. Any inhomogeneity can produce spatially varying carrier doping and superconducting properties, which would hamper the efforts.

If the earlier studies presented in this work are any indication, YBCO is best suited for study in this region, due to the stoichiometric cation composition and high quality crystals available here at UBC. Because of the high mobility of the chain oxygen ion compared to cations such as Sr^{2+} (in $La_{1.85}Sr_{0.15}CuO_4$), YBCO is, in principle, *more* easily made homogeneous compared to other high Tc cuprates. It has the further advantage that the doping can be manipulated by simple and reversible changes in the annealing conditions following crystal growth. However, the annealing steps can present a number of difficulties. The crystals are vulnerable to the coexistence of multiple phases, and several such phases have been seen to exist in the vicinity of the AFM-SC boundary [82, 83]. With care and much tweaking of the annealing conditions, it is possible to prepare samples with a reasonably sharp transition width

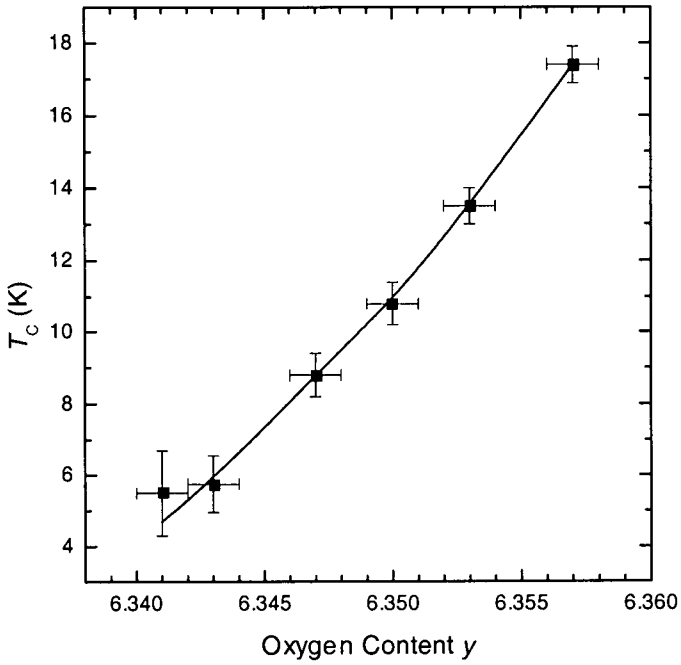

Figure 5.1: Transition temperature of samples after annealing at 23C for several weeks.

of under 2 kelvin. This has been achieved in several steps by Dr Liang. First the crystals have to be set to an oxygen content of around 6.35 by annealing together with YBCO ceramic under pure oxygen flow at around 900 C for a week. These are then quenched rapidly to room temperature. The inhomogeneity that this step can introduce is reduced by sealing the crystals with the ceramic into a quartz tube, and annealing at 570 C for 2 weeks. This is followed by a rapid quench into a beaker of ice cold water.

Samples prepared in this region with an oxygen content of $O_{6.35\pm0.01}$ are orthorhombic at room temperature, and undergo an orthorhombic to tetragonal transition around 140 C, observed optically during detwinning of the crystals. They have the remarkable property that after the quenching step from 570 C, they are not superconducting. The nice feature of the crystals is that due to the very high purity of the material, the chain oxygens are mobile at room temperature, and they are

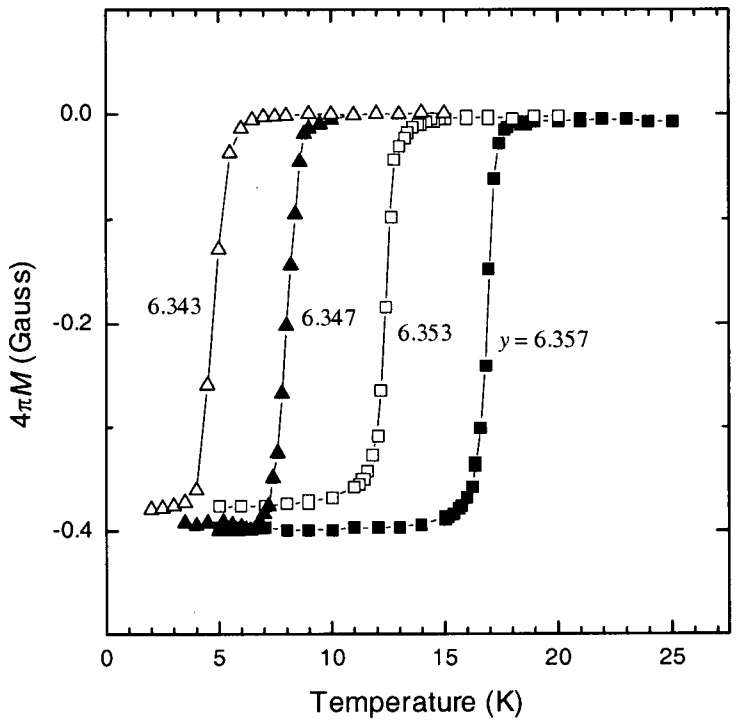

Figure 5.2: Field cooled Magnetization after annealing at 23 degrees. Data was taken for an applied field of 1 Oe parallel to the $\hat{c}$-axis of the crystals [83].

energetically driven to form longer chains. Lone oxygens do not have the ability to remove enough electrons from the CuO_2 planes, but given time, the formation of longer chains produces enough holes in the planes to drive the samples to superconduct. Hence by leaving the samples to anneal at room temperature over a span of weeks, the samples reach a maximum T_c determined by their oxygen content. This is shown in Fig. 5.1. This phenomenon is probably the closest thing to having tunable hole doping in a HTSC system, other than photodoping and field effect doping which has received much attention over the last few years [84]. We can see that the maximum T_c is very sensitive to the oxygen content, changing by 0.8 Kelvin for a 0.001 change in the oxygen content. This corresponds to a change of 1 degree during the initial anneal at 900 C, giving an indication of the care needed in preparing such samples.

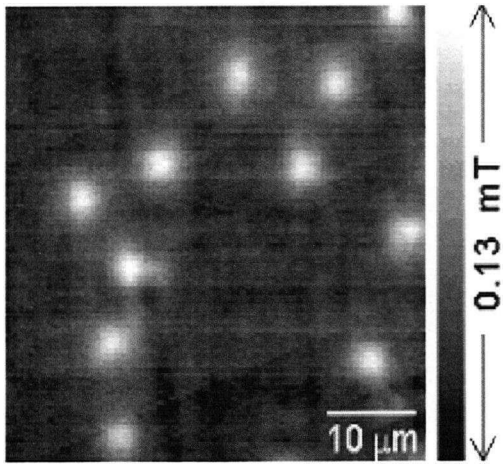

Figure 5.3: Image of vortices in a 0.1 Oe field cooled sample at 3K [85].

The samples were further characterized by Dr. Liang using a SQUID magnetometer. The magnetization is shown in Fig. 5.2 for field cooling in a 1Oe field parallel to the $\hat{c}$-axis of the crystals. The crystals show a sharp transition width (10% to 90%) of 1 Kelvin for samples with $T_c > 10K$, increasing slightly with lower T_c to 1.6K width. The rapidly varying transition temperature with oxygen content, shown in Fig. 5.1, indicates that such transition widths are those of homogeneously doped samples.

Further studies have been made on these samples at Stanford University by examining vortices using scanning hall probes [85]. Fig. 5.3 shows vortices in a sample with a T_c of 12K [85]. The sample has been cooled to 3K in a field of 0.1 Oe. The spatial resolution of the probe is about 2 microns, and the degree of uniformity of the size of the vortices indicate that the sample is homogeneous over such length scales.

5.1 Electrodynamics of low T_c samples

The study of the electrodynamics of low doped samples is complicated by the weak $\hat{c}$-axis coupling. Early work in YBCO has shown that the magnitude of the $\hat{c}$-axis penetration depth can reach 7 microns in samples doped to $O_{6.6}$. Such high values along the $\hat{c}$-axis can dwarf all other penetration from the planar currents, but opens the possibility of applying our cavity perturbation technique to measurements of the $\hat{c}$-axis penetration depth.

In measurements of the planar penetration depth on optimally doped YBCO, only changes in the temperature dependence are discernable, and no attempt is made to obtain the absolute value, which is left to other techniques such as infrared spectroscopy or μSR. This is because the zero temperature penetration depth is typically 1/100 of the thickness (for a 10 micron sample), and to know it better than 10% we would need to know the thickness to better than 1 part in 1000. For low dopings however, as will be shown, the penetration depth along the $\hat{c}$-axis exceeds 30 microns, and this *can* be measured in samples that are several hundred microns thick.

5.1.1 Sample Preparation

The planar penetration depth in highly underdoped samples has been reported to be as high as a few microns at a few Kelvin using scanning Hall measurements on vortices [85]. This is considerably smaller than along the $\hat{c}$-axis which has zero temperature penetration depths exceeding 30 microns, a fact we will show in the next section. To minimize the contribution from the planes to a level where we can safely ignore it, we chose to polish thick samples into slabs with a major $\hat{c}$-axis face. This presents a number of difficulties. First, the number of samples which grow to thicknesses over 0.35 mm along the $\hat{c}$-axis are relatively rare in a growth run. Second, most thick samples usually have macroscopic structural defects, which show up during polishing. As a result, crystals more often than not break into pieces during the polishing, and

the time taken to produce crystals worthy of microwave measurements is long.

Despite these difficulties, two crystals were picked for detailed study. They were from different batches grown in Barium Zirconate crucibles, and both samples were annealed to $O_{6.35}$ using an initial anneal at around 900 C, followed by a 570 C anneal to homogenize the oxygen content.

The samples were cut using a wire saw, and then polished using the methods described in chapter 2. After polishing they measured a=1.33(3), b=0.245(3), c=0.372(3) mm for the first sample, and a=1.803(3), b=0.203(3),c=0.391(3) mm for the second sample. The crystals were both fully twinned, and the use of the labels a, and b are just to separate the two planar directions in the crystals. The samples were inserted into the TE_{011} mode of the 22.7 GHz cavity, with $\vec{H}_{AC}$ along the long direction of the crystal to induce mainly ĉ-axis currents.

During the preparation, it was necessary that the samples be heated up in air to temperatures of about 80 C, for gluing with crystal bond to the polishing holder. This meant that at the start of the measurements on both samples, the crystals would have spent a few days at room temperature and self annealed. As a result, the samples had a T_c of about 9 K to start, and with further time at room temperature they annealed to a higher T_c. After the initial set of measurements, an attempt was made to disorder the oxygen content by raising the sample temperature in a sealed quartz tube. Temperatures of 100 C, 250 C, 350 C, and 450 C were attempted and measurements made after each disordering attempt. These trials were not successful in that the T_c of the sample was broadened and another phase was found to be present. This was seen in our measurements as an early buildup of the superfluid density around 30-50 K shown in Fig. 5.6. To overcome the oxygen inhomogeneity problem, the oxygen content of one crystal was reset at 900 C, followed by a 570 C anneal. The oxygen content was increased over the previous value (previously doped to have a maximum T_c of 13 K), and the final T_c of the sample was measured as 19.4 K after a week at room temperature.

5.2 Experimental Results and analysis

The raw measurements on one crystal are shown in Fig. 5.4, and are representative of measurements on the second sample studied. The frequency shifts have been plotted relative to their value in the normal state when the sample goes thin, and all the field has penetrated the sample. The first noticeable effect is the change in T_c of the sample when it was allowed to anneal at room temperature between each measurement. The figure also illustrates the sensitivity of the method to measurements of the $\hat{c}$-axis penetration depth. The magnitude of the shift from 1.2 Kelvin through the transition is proportional to the field volume that is excluded by the sample. The data indicates that the zero temperature penetration depth gets larger for lower T_c values, and the field volume which is excluded gets smaller.

To quantify the raw measurements we have to address several issues. First we will assume that by having reshaped the crystals, most of the field penetration is associated with currents running along the $\hat{c}$-axis of the crystals. This is a valid assumption in the highly underdoped regime where we know that the zero temperature $\hat{c}$-axis penetration depth is larger than 30 μm, and that in the planes is less than a couple of microns. The maximum contribution to the signal is at the 5% level from the planes, and we expect it to decrease at higher temperatures, since the $\hat{c}$-axis penetration rises much faster in absolute units of microns per Kelvin, than along the planes. An anisotropic electrodynamic model which would otherwise be needed can thus be simplified to the case of a 1-D model for fields penetrating from one direction.

In the situation where the penetration depth is getting comparable to the thickness of the sample, finite size effects are important and the surface impedance that is measured experimentally is given by the usual expression,

$$Z_S^{eff} = R_S^{eff} + i(X_S^0 + \Delta X_S^{eff}) = \Gamma(\Delta(1/Q_0) + 2i\Delta f_0/f_0) \tag{5.1}$$

with the only caveat that this is an effective surface impedance, Z_S^{eff}, different from the true surface impedance. Γ is the calibration constant that is determined from

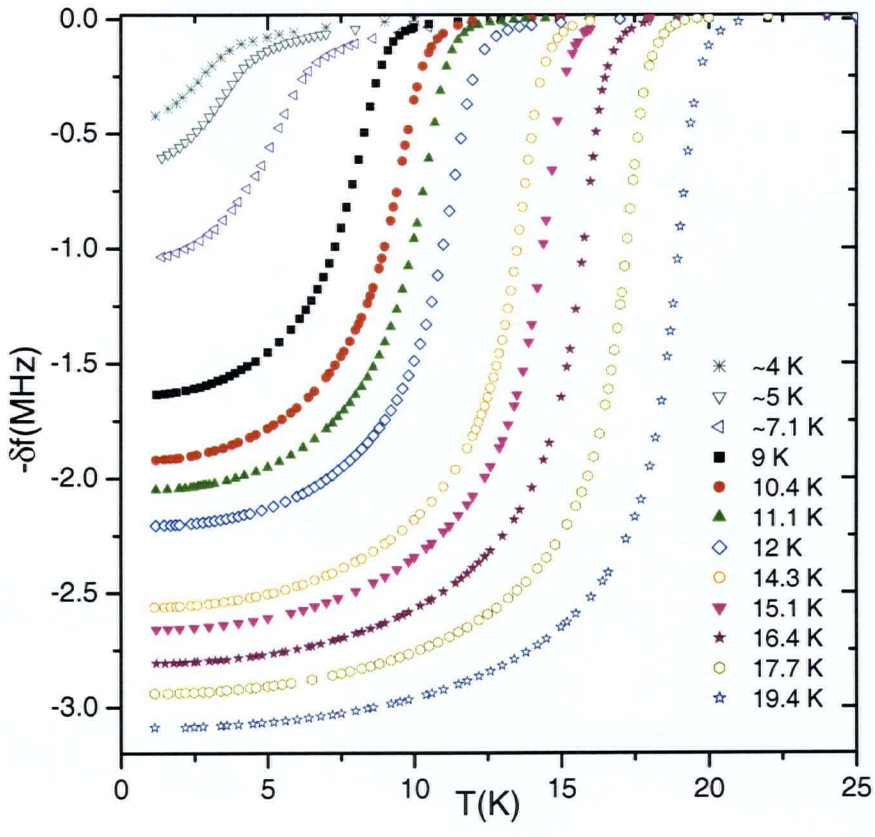

Figure 5.4: Raw data obtained from successive measurements on underdoped sample. Sample was allowed to anneal to a higher T_c between each dataset.

measurements on a Pb-Sn calibration sample. The value X_S^0 is the zero temperature surface reactance offset determined from the normal state where the sample is completely in the thin limit. Here all the field has penetrated into the sample and we observe no further shifts with increasing temperature. The effective surface impedance is related to the true surface impedance, Z_S, by

$$Z_S^{eff} = Z_S \tanh(\frac{i\mu_0\omega t}{2Z_S}) \tag{5.2}$$

where t is the thickness of the sample. This is true in all limits where if the thickness t is several times the penetration depth, the tanh term is one and $Z_S^{eff} = Z_S$. A simple inversion of this equation yields the surface impedance. Included in the analysis to extract the microwave conductivity is the fact that the charge conductivity and

the electrical displacement current enter the surface impedance formula, Eq. 2.2, on the same footing. Usually this is ignored for highly doped samples due to the large conductivity, but at low doping the conductivity is very small and the displacement current contributes to the measured penetration depth. The dielectric constant along the c-direction is taken as $\epsilon_r = 20$ from infrared measurements on underdoped YBCO [59].

5.2.1 $\hat{c}$-axis superfluid density

The surface impedance was extracted using the model described above. A nice feature of the measurements is that the $\hat{c}$-axis superfluid density comes out naturally from the data. Figure 5.5 shows the superfluid density extracted from measurements on the crystals, plotted as the imaginary part of the conductivity, $\sigma_2 = \frac{n_s e^2}{m^* \omega}$.

The data reveals the rapid buildup of superfluid density below the transition, although we see some rounding at T_c. This is due to the fact that at low doping, the transition temperature varies quickly with hole concentration, and the samples cannot be made to the same level of homogeneity we can achieve at optimal doping. The data at the lower hole dopings (where $T_c < 8$ K) had to be obtained by disordering the oxygen content of the crystals to reduce the T_c to zero. This was tried by annealing at several temperatures from 100 C to 450 C and always resulted in some inhomogeneity in the sample, seen as an early buildup of the superfluid density shown in Fig. 5.6. The onset temperature of this kind of disorder was reduced by heating to higher temperatures in a sealed quartz tube, but it could not be heat treated further due to the risk of losing some chain oxygen. The final solution was to reset the oxygen content at 900 C and then anneal at 570 C with sealed ceramic to homogenize the sample again. The data taken for T_c's in the range 14 to 19.4 K are on this reannealed sample with a slightly higher oxygen content.

An interesting observation is seen immediately if we look at the magnitude of the superfluid density as $T \rightarrow 0$, which is related to the zero temperature $\hat{c}$-axis

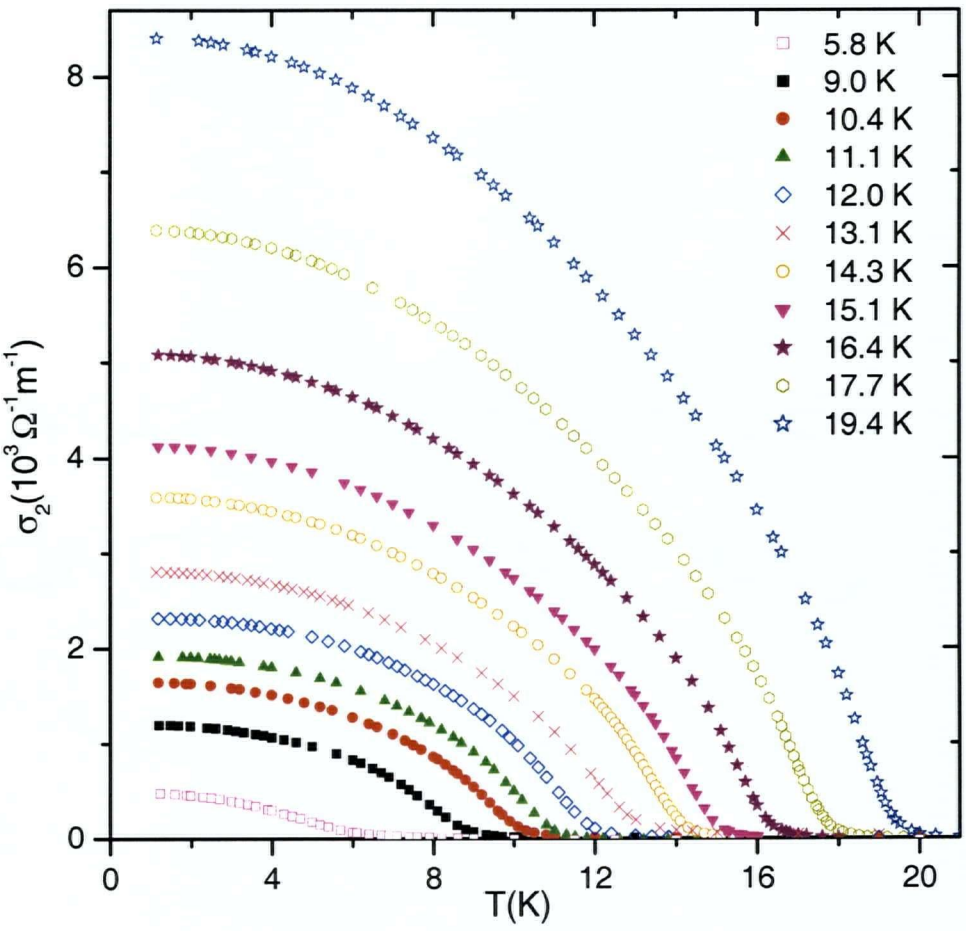

Figure 5.5: $\hat{c}$-axis superfluid density in underdoped YBCO.

penetration depth. This is shown for data on both crystals in Fig. 5.7. The lower T_c data taken after one additional anneal at 450 C is also shown, although we note that there was an early buildup of superfluid density at higher temperatures, as shown in Fig. 5.6. The magnitude of this buildup is however small, and likely not to bother the zero temperature penetration depth value as evidenced by the two data sets with similar T_c's plotted in Fig. 5.6. We have thus included the low T_c data in Fig. 5.7, and the horizontal error bars indicate the T_c uncertainty, about ± 0.5 K. Also plotted is a $T_c^{2.4}$ line showing good agreement with the data. This temperature dependence is faster by at least one power of T_c from that seen in the *ab*-plane where Uemura has seen a different scaling law in the underdoped regime of the cuprates [86], that

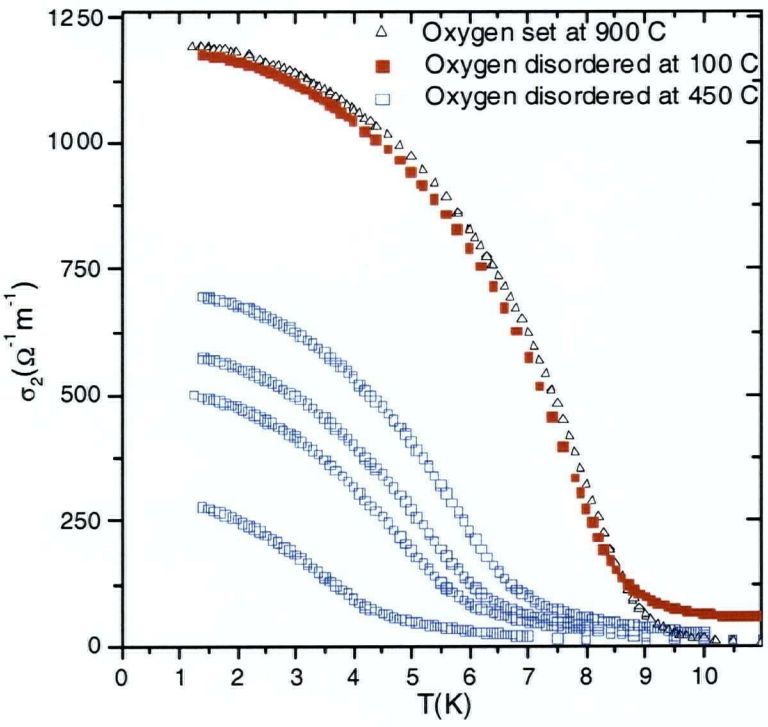

Figure 5.6: Early buildup of superfluid density observed when sample annealed at 100, and 450 C.

is n_s varying linearly with T_c. It is important here to note that the magnitude of the $\hat{c}$-axis penetration depth is not very sensitive to the chain oxygen content, and even quite reproducible between crystals which were produced in different growth runs.

Another feature of the superfluid density is seen by normalizing to its value at zero temperature, and by T_c. We find that in the range of T_c's between 9 and 19 K, the temperature dependence is *almost* independent of doping, Fig. 5.8. For the data taken initially on the sample whose T_c maximized at $13K$ there was perfect scaling. However, when the oxygen content was set to a higher level, around 6.36, corresponding to a T_c^{max} of 19.4 K, in detail there was a slight change in shape at intermediate temperatures between the data sets. Part of this is likely due to the different chain oxygen content as evidenced by the slight variation shown in Fig. 5.8. Part of the variation could also be due to a slightly varying demagnetization factor

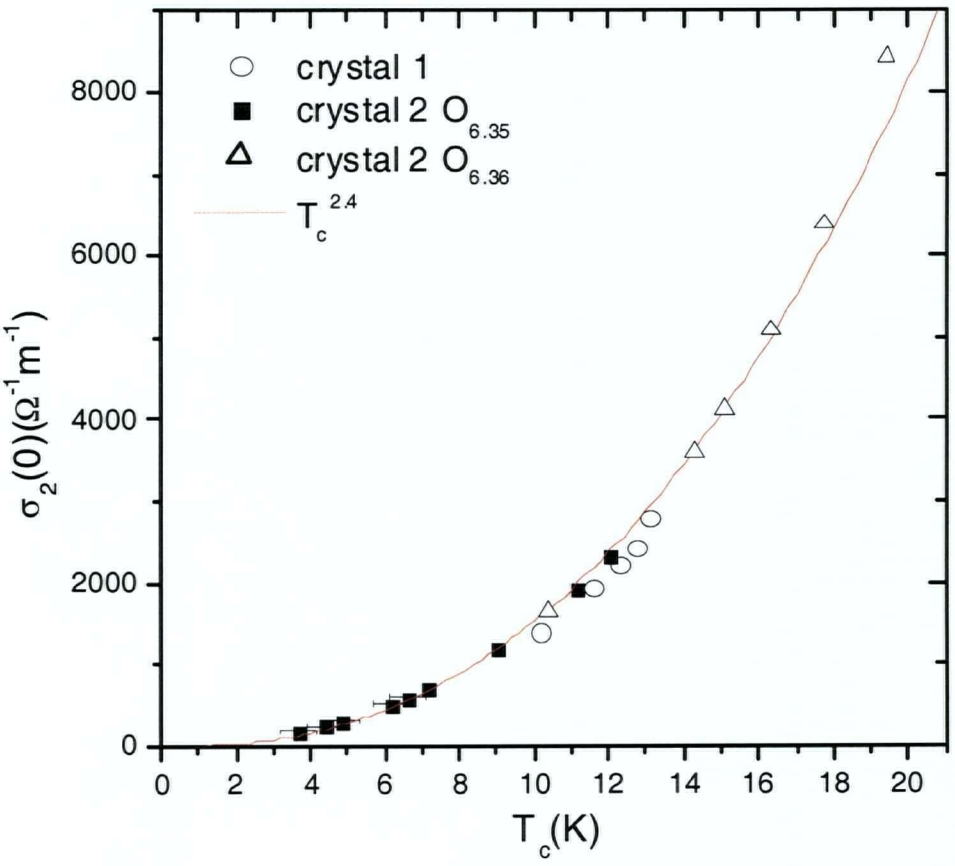

Figure 5.7: Plot of $\sigma_2(0)$ as a function of T_c.

which we believe is present at the higher doping levels, where the penetration depth becomes small (less than 30 microns at 19 K). At the present time we cannot correct for a temperature dependent calibration constant, but it is a small correction of the order of a few percent. Nevertheless small shape variations could come from this, as well as a slight overestimate of the zero temperature superfluid density at higher dopings.

To compare this data with other YBCO data, we have plotted the $\hat{c}$-axis superfluid fraction for $YBa_2Cu_3O_{6.6}$ and $YBa_2Cu_3O_{6.95}$, taken by Saeid Kamal [35]. The scaling with our newer data on the highly underdoped crystal does not hold at higher temperatures, although the low temperature dependence is similar in the different data sets. At optimal doping this dependence is closer to T^2 up to $0.4T_c$, whereas in

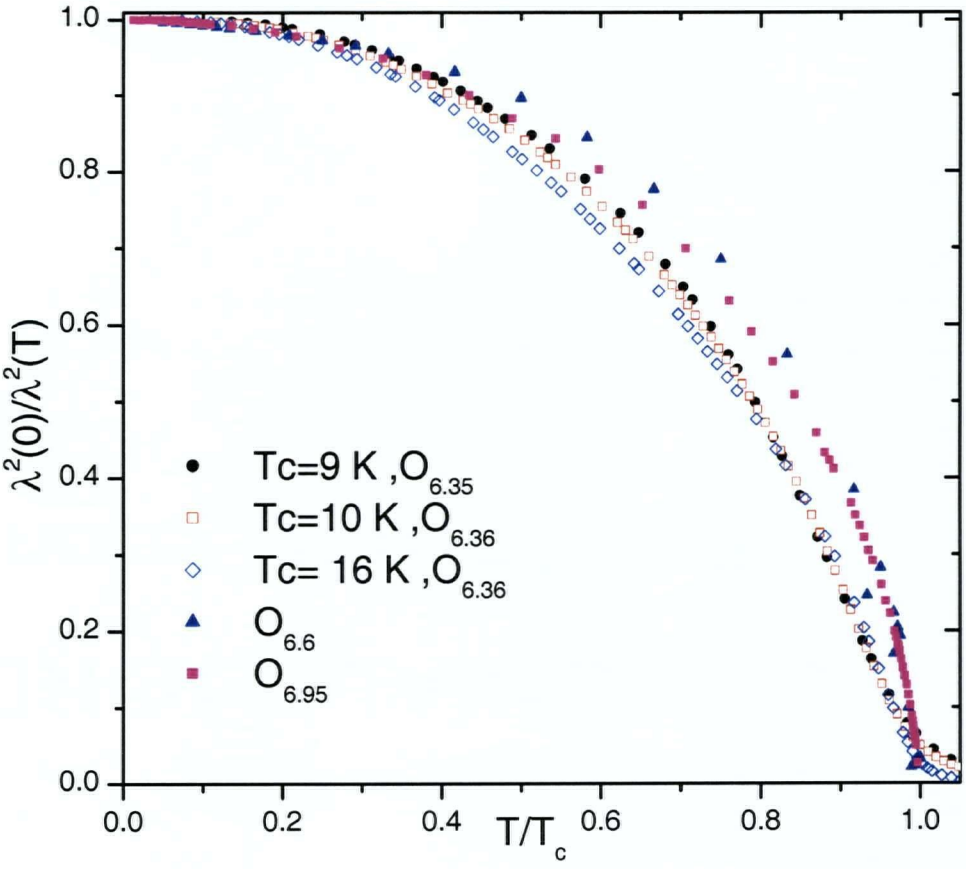

Figure 5.8: Plot of superfluid fraction versus reduced temperature for samples with T_c's in the range 9 to 19 K.

the highly underdoped samples a better fit is obtained to $T^{2.5}$ over this range. As mentioned partly in the discussion in chapter 4, this temperature dependence can come from several models. At the lower dopings it is likely that a tunnelling model [69] should be more appropriate than a coherent hopping model proposed by Xiang *et al.* [74]. Coherent band like transport is unlikely given the lack of a Drude peak in $\sigma_1(\omega)$ of underdoped cuprates.

In the tunnelling model, the system is assumed to consist of layered SIS junctions, where $1/\lambda^2$ is determined by the critical current through the junctions. For the case of specular transmission, the critical current has the Ambegaokor-Baratof form, i.e $\lambda^2(0)/\lambda^2(T) = \left\langle \frac{\Delta_k}{\Delta_0} \tanh(\Delta_k/2T) \right\rangle_k$. This behaves as T^2 at low temperatures. We

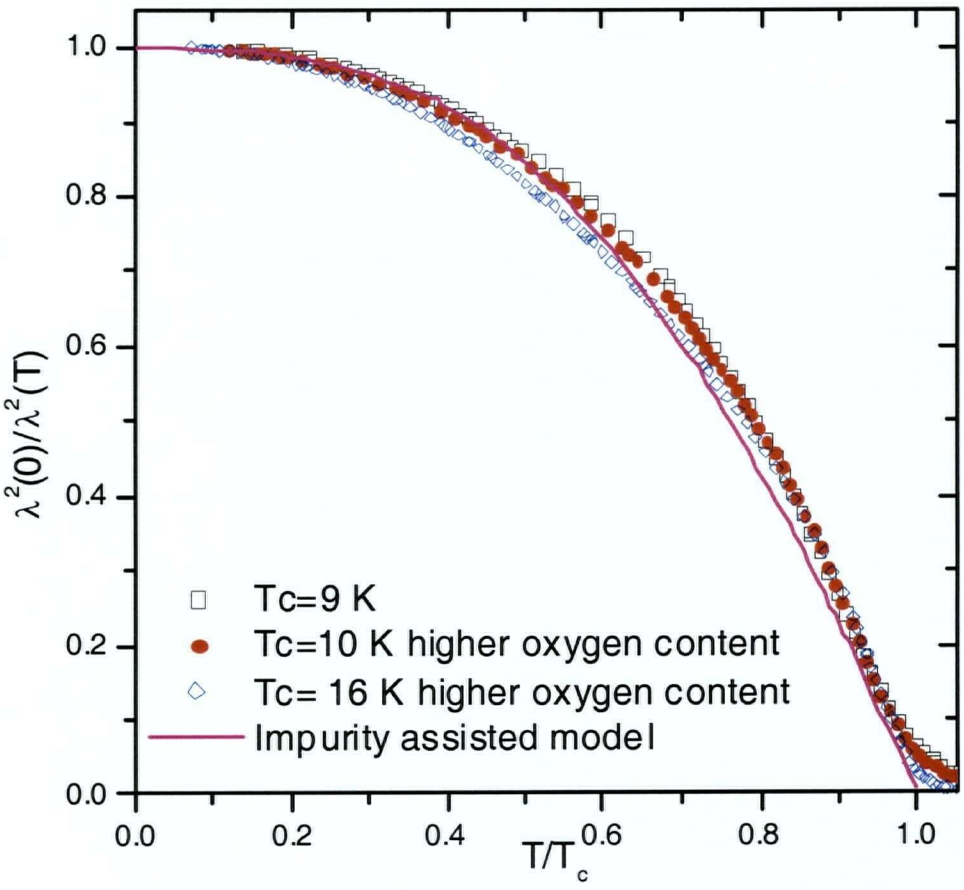

Figure 5.9: Comparison of superfluid fraction to model of Radtke *et al.* [69].

compare the temperature dependence of our data to that obtained numerically by Radtke *et al.* for the case of both specular, and partly diffuse transmission. The scaled temperature dependence of the superfluid density does not vary in the model for the two cases, however the magnitude of the superfluid density is strongly dependent on the diffusivity of the tunnelling. We show the scaled temperature dependence in Fig. 5.9. The agreement in the shape of the superfluid density is quite good at low temperatures, and even holds quite well up to T_c. The fact that our data on two samples with several annealings gives consistently similar values for the zero temperature superfluid density indicates that the $\hat{c}$-axis penetration depth is not very sensitive to chain disorder at the lowest dopings.

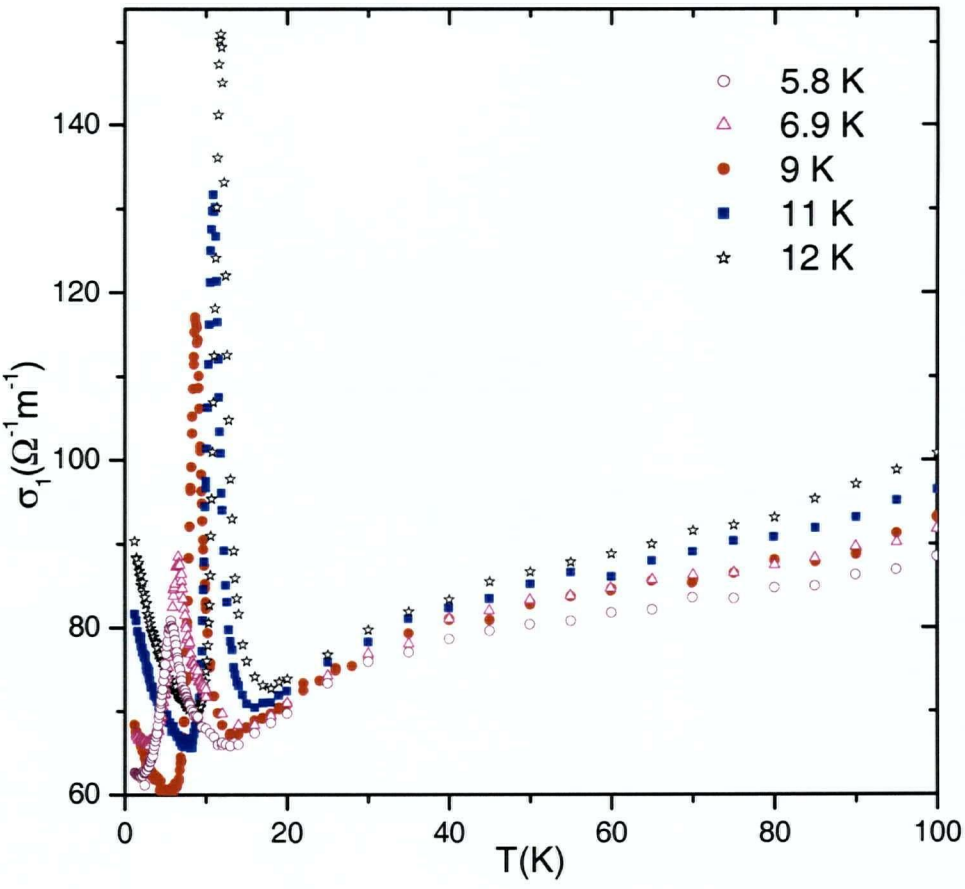

Figure 5.10: Plot of $\hat{c}$-axis conductivity in underdoped YBCO.

5.2.2 $\hat{c}$-axis conductivity

The imaginary part of the conductivity which represents the superfluid response was shown in the previous section. The real part was obtained in the analysis simultaneously and is shown in Fig 5.10. Above T_c we observe a non-metallic resistivity ($\rho = 1/\sigma_1$, with $d\rho_c/dT < 0$) up to 160 K, which is the high range of our measurements. At the transition, the conductivity shows a large peak whose width is between 2 and 5 Kelvin. This is usually seen in *ab*-plane measurements, although much narrower and is associated with superconducting fluctuations. Below T_c the conductivity stays finite down to the lowest temperatures and is rising in the superconducting state. This feature cannot be attributed to the $\hat{c}$-axis alone, and it

is likely that the ĉ-axis conductivity extracted here is contaminated by the *ab*-plane conductivity that is much larger. Without further thinning the crystal it would be difficult to unambiguously separate them. In the superconducting state, the analysis for the superfluid density is not sensitive to this and our conclusions in the previous section are not affected. As a result of these difficulties we cannot make many statements regarding the doping dependence of the conductivity. What is certain from the data however, is the fact that the conductivity in the superconducting state is rising with higher hole doping. The values obtained here are smaller by two orders of magnitude than the ĉ-axis conductivity seen in the superconducting state of optimally doped YBCO, indicating that this uptrend in the conductivity will continue across the phase diagram. This is expected and parallels the rising normal state conductivity seen in dc-measurements on the cuprates. The value for the normal state conductivity obtained here does not show much variation immediately above T_c, again possibly due to a much larger *ab*-plane conductivity that is masking the intrinsic ĉ-axis behaviour. Future measurements are needed to study dc-transport in these crystals, as well as microwave measurements aimed at *ab*-plane behaviour.

Chapter 6

Conclusions

The work described in this dissertation has been a detailed study of the anisotropic microwave electrodynamics of YBCO. Although the subject has been extensively studied over recent years, we have been able to make headway in some aspects of understanding the electrodynamics both in the copper oxygen planes, and transport along the $\hat{c}$-axis.

In-plane electrodynamics of $YBa_2Cu_3O_{6.99}$

The work on the $\hat{a}$-axis properties is one of the more complete microwave measurements obtained on a crystal of a high temperature superconductor, and would have not been achieved without the common goal of several students, ready to tackle the problem with their separate experiments. The data obtained by five cavity perturbation measurements reveal more detail regarding the conductivity spectrum $\sigma_1(\omega)$ of the thermally excited quasiparticles in the superconducting state than earlier work on this material [11]. The conductivity is found to be well described by a Drude-like lineshape, although in detail there were deviations from this shape at the lowest temperatures. This has been more recently confirmed using bolometric measurements at 1.2 K [50]. The Drude lineshape widths nevertheless can be associated with a transport scattering rate of quasiparticles, and below T_c this width collapses rapidly and it becomes easily discernible in the microwave spectral range at temperatures below 55 K. Between 20 K and 45 K we find that the collapse of the inelastic transport scattering rate varies at least as fast as T^4. The rapid collapse of the scattering rate in this regime is found to fit well to an umklapp scattering model of nodal quasiparticles. Below 20 K the width becomes extremely narrow and nearly temperature

independent. This narrow width of only 9 GHz corresponds to a mean free path as long as 4 μm if we interpret the width as being a direct measure of the elastic scattering rate due to impurities. Some features of $\sigma_1(\omega, T)$ below 20 K are in accord with quasiparticle scattering in the Born limit for a $d_{x^2-y^2}$ superconductor, in particular a gradual evolution of the shape of $\sigma_1(T)$ from a sublinear T dependence at low ω, to a quasilinear and then superlinear one at higher ω.

$\hat{c}$-axis electrodynamics of $YBa_2Cu_3O_{7-\delta}$

Interlayer coupling in the cuprates has been known from transport measurements to be an incoherent process above T_c, and our microwave measurements have extended this into the superconducting state. The work on the $\hat{c}$-axis electrodynamics has only been possible as a culmination of several years of experience studying the in-plane electrodynamics of YBCO, and carefully isolating the out of plane response.

The electrodynamics has been investigated for samples at optimal doping, as well as at the low doping level of $\sim O_{6.35}$. The measurements in the underdoped regime are the earliest studies of the superconducting state near the AFM-SC boundary, and the extreme anisotropy accompanying this level of underdoping has limited the work to $\hat{c}$-axis properties.

The superfluid density is found to be different for transport out of the CuO_2 planes, where a linear low-T dependence is observed. Instead the low temperature dependence in all our studies is between T^2 and T^3, consistent with the $\hat{c}$-axis behaviour of other cuprates, and with several models of $\hat{c}$-axis transport [74, 69]. These measurements indicate that we are not simply dealing with a highly anisotropic 3-D metallic state, and that the complex electronic structure plays a role in the out of plane response. These measurements also revealed the doping dependence of the $\hat{c}$-axis superfluid density. We observe that this superfluid density scales quite well in the underdoped regime for samples with T_c's in the range 9 to 19 Kelvin, and at low temperatures below $0.5T_c$ with highly doped samples. The zero temperature superfluid density is also found to scale with $T_c^{2.4\pm0.1}$ in the underdoped regime. The

magnitude of the penetration depth extracted from our measurements starts at about 30 microns for a 19 K sample, and increases to hundreds of microns at lower dopings. These values indicate that the $\hat{c}$-axis coupling in underdoped YBCO is very weak, and similar to optimally doped BSSCO.

For the conductivity we find, contrary to earlier studies [42, 26], that charge transfer between planes is not influenced by the development of long transport lifetimes seen in *ab*-plane measurements below T_c, and is perhaps suppressed by the same mechanism responsible for the very low $\hat{c}$-axis conductivity in the normal state. Unfortunately there is no consensus over what limits the $\hat{c}$-axis conductivity, even in optimally doped YBCO which is one of the least anisotropic members of the cuprates. In the most anisotropic member, $Bi_2Sr_2CaCu_2O_{8+\delta}$, similar behaviour has been reported in the superconducting state [78], even though $\sigma_{1c}(T)$ is found to be two orders of magnitude smaller that for optimally doped YBCO. The resemblance between these two materials with vastly varying anisotropies indicates that interlayer single particle transfer is intrinsically incoherent in the cuprates, even through the superconducting transition. In the highly underdoped regime of YBCO, the extracted conductivities also show values much smaller than those found at optimal doping by two orders of magnitude, showing that poor charge transport remains throughout the doping phase diagram of YBCO.

Bibliography

[1] G. Bednorz and K. A. Müller. *Z. Phys. B: Condens Matter*, 64:189, 1986.

[2] P. W. Anderson and Z. Zou. *Phys Rev Lett.*, 60:132, 1988.

[3] A. B. Pippard. *Proc. Roy. Soc.*, A216:547, 1954.

[4] R.E. Glover and M. Tinkham. *Phys. Rev.*, 108:243, 1957.

[5] M.A. Biondi, A.T. Forester, and M.P. Garfunkel. *Phys. Rev.*, 108:497, 1957.

[6] W.N. Hardy, D.A. Bonn, D.C. Morgan, Ruixing Liang, and Kuan Zhang. *Phys. Rev. Lett.*, 70:3999, 1993.

[7] W. H. Keeson and A. J. Kok. *Commun. Phys. Lab*, 221e, 1932.

[8] W. Meissner and R. Ochsenfeld. *Naturwissenshaften*, 21:787, 1933.

[9] F. London and H. London. *Proc. R. Soc*, A 149:71, 1935.

[10] Ioan Kosztin and Anthony J. Leggett. *Phys. Rev. Lett.*, 79:135, 1997.

[11] D.A. Bonn, Kuan Zhang, Ruixing Liang, D.J. Baar, D.C. Morgan, P. Dosanjh, T.L. Duty, A. MacFarlane, G.D. Morris, J.H. Brewer, W.N. Hardy, C. Kallin, and A.J. Berlinsky. *Phys. Rev. B*, 47:11314, 1993.

[12] P.J. Hirschfeld, W.O. Puttika, and D.J. Scalapino. *Phys. Rev. Lett.*, 71:3705, 1993.

[13] J. Rossat-Mignod, L. P. Regnault, M. J. Jurgens, C. Vettier, P. Burlet, J. Y. Henry, and G. Lapertot. *Physica B*, 163:4, 1990.

[14] S. Tajima, J. Schutzmann, S. Miyamoto, I. Terasaki, Y. Sato, and R. Hauff. *Phys. Rev. B*, 55:6051, 1997.

[15] D.A. Bonn and W.N. Hardy. *Physical Properties of High Temperature Superconductors.* World Scientific,Singapore, 1996.

[16] C. C. Tsuei, J. R. Kirtley, C. C. Chi, Lock See Yu-Jahnes, A. Gupta, T. Shaw, J. Z. Sun, and M. B. Ketchen. *Phys. Rev. Lett.*, 73:593, 1994.

[17] J. R. Kirtley, C. C. Tsuei, M. Rupp, J. Z. Sun, L. S. Yu-Jahnes, A. Gupta, M. B. Ketchen, K. A. Moler, and M. Bhushan. *Phys. Rev. Lett.*, 76:1336, 1996.

[18] P.J. Hirschfeld, W.O. Puttika, and D.J. Scalapino. *Phys. Rev. B*, 50:10250, 1994.

[19] D.A. Bonn, S. Kamal, Kuan Zhang, Ruixing Liang, D.J. Baar, and W.N. Hardy. *Phys. Rev. B*, 50:4051, 1994.

[20] Louis Taillefer, Benoit Lussier, Robert Gagnon, Kamran Behnia, and Herve Aubin. *Phys. Rev. Lett.*, 79:483, 1997.

[21] P.A. Lee. *Phys. Rev. Lett.*, 71:1887, 1993.

[22] A. C. Durst and P. A. Lee. *Phys. Rev. B*, 62:1270, 2000.

[23] R.C. Yu, M.B. Salamon, J.P. Lu, and W.C. Lee. *Phys. Rev. Lett.*, 69:1431, 1992.

[24] D.M. Broun, D.C. Morgan, R.J. Ormeno, S.F. Lee, A.W. Tyler, A.P. MacKenzie, and J.R. Waldram. *Phys. Rev. Lett.*, 56:11443, 1997.

[25] T. Shibauchi, A. Maeda, H. Kitano, T. Honda, and K. Uchimokura. *Physica C*, 203:315, 1992.

[26] Jian Mao, D.H. Wu, J.L. Peng, R.L. Greene, and Steven M. Anlage. *Phys. Rev. B*, 51:3316, 1995.

[27] Steven M, Anlage, Dong-Ho Wu, J. Mao, X.X. Xi, T. Venkatesan, J.L. Peng, and R.L. Greene. *Phys. Rev. B*, 50:523, 1994.

[28] T. Shibauchi, H. Kitano, K. Uchinokura, A. Maeda, T. Kimura, and K. Kishio. *Phys. Rev. Lett.*, 72:2263, 1994.

[29] U. Dahne, Y. Goncharov, N. Klein, N. Tellmann, G. Kozlov, and K. Urban. *J. Supercond*, 8:129, 1995.

[30] D.B. Romero, C.D. Porter, D.B. Tanner, L. Forro, D. Mandrus, L. Mihaly, G.L. Carr, and G.P. Williams. *Phys. Rev. Lett.*, 68:1590, 1992.

[31] Martin C. Nuss, P.M. Mankiewich, M.L. O'Malley, E.H. Westerwick, and Peter B. Littlewood. *Phys. Rev. Lett.*, 66:3305, 1991.

[32] S. Spielman, Beth Parks, J. Orenstein, D.T. Nemeth, John Clarke, Paul Merchant, and D.J. Lew. *Phys. Rev. Lett.*, 73:1538, 1994.

[33] A. Pimenov, A. Loidl, G. Jakob, and H. Adrian. *Phys. Rev. B*, 51:7039, 2000.

[34] Ahmad Reza Hosseini-Gheinani. A probe to study the microwave surface resistance of crystals, of the high temperature superconductor YBCO. Master's thesis, University of British Columbia, 1997.

[35] Saeid Kamal. *Precision measurements of the magnetic penetration depth in* $YBa_2Cu_3O_{7-\delta}$. PhD thesis, University of British Columbia, 2002.

[36] Pinder Dosanjh. Microwave surface resistance measurements of $YBa_2Cu_3O_{7-\delta}$ single crystals and melt textured slabs employing a niobium double split-ring resonator. Master's thesis, University of British Columbia, 1999.

[37] Richard Harris. Measurement and analysis of the in-plane electrodynamics of $YBa_2Cu_3O_{6.99}$ at microwave frequencies. Master's thesis, University of British Columbia, 1999.

[38] Kuan Zhang. *Studies of the microwave surface resistance of pure, zinc, and nickel doped YBCO crystals.* PhD thesis, University of British Columbia, 1995.

[39] Emile Hoskins. Effects of polishing on the microwave properties of $YBa_2Cu_3O_{7-\delta}$. Technical report, University of British Columbia, 1999.

[40] D.A. Bonn, P. Dosanjh, R. Liang, and W.N. Hardy. *Phys. Rev. Lett.*, 68:2390, 1992.

[41] Kuan Zhang, D.A. Bonn, Ruixing Liang, D.J. Baar, W.N. Hardy, D. Basov, and T. Timusk. *Phys. Rev. Lett.*, 73:2484, 1994.

[42] H. Kitano, T. Shibauchi, K. Uchinokura, A. Maeda, H. Asaoka, and H. Takei. *Phys. Rev. B*, 51:1401, 1995.

[43] Ruixing Liang, D.A. Bonn, and W.N. Hardy. *Physica C*, 304:105, 1998.

[44] S.Kamal, Ruixing Liang, A. Hosseini, D.A. Bonn, and W.N. Hardy. *Phys. Rev. B*, 58:8933, 1998.

[45] J.L. Tallon, C. Bernhard, U. Binninger, A. Hofer, G.V.M. Williams, E.J. Ansaldo, J.I. Budnick, and Ch. Niedermayer. *Phys. Rev. Lett.*, 74:1008, 1995.

[46] D. N. Basov, R. Liang, B. Dabrowski, D. A. Bonn, W. N. Hardy, and T. Timusk. *Phys. Rev. Lett*, 77:4090, 1996.

[47] A. Hosseini, Richard Harris, Saeid Kamal, Pinder Dosanjh, J. Preston, Ruixing Liang, W.N. Hardy, and D.A. Bonn. *Phys. Rev. B.*, 60:1349, 1999.

[48] S. Kamal, D.A. Bonn, Nigel Goldenfeld, and P.J. Hirschfeld. *Phys. Rev. Lett.*, 73:1845, 1994.

[49] M.S. Pambianchi, S.N. Mao, and S.M. Anlage. *Phys. Rev. B*, 53:4477, 1995.

[50] Patrick Turner. A bolometric technique for broadband measurement of surface resistance and application to single crystal $YBa_2Cu_3O_{6.99}$. Master's thesis, University of British Columbia, 1999.

[51] Kuan Zhang, D.A. Bonn, Ruixing Liang, D.J. Baar, and W.N. Hardy. *Appl. Phys. Lett.*, 62:3019, 1993.

[52] Peter J. Hirschfeld and Nigel Goldenfeld. *Phys. Rev. B*, 48:4219, 1993.

[53] D. Xu, S.K. Yip, and J.A. Sauls. *Phys. Rev. B*, 51:16233, 1995.

[54] S. Hensen, G. Muller, C.T. Rieck, and K. Scharnberg. *Phys. Rev. B*, 56:6237, 1997.

[55] A. J. Berlinsky, D. A. Bonn, R. Harris, and C. Kallin. *Phys. Rev. B*, 61:9088, 2000.

[56] D. Achkir, M. Poirier, D.A. Bonn, Ruixing Liang, and W.N. Hardy. *Phys. Rev. B*, 48:13184, 1993.

[57] S.M. Quinlan, D.J. Scalapino, and N. Bulut. *Phys. Rev. B*, 49:1470, 1994.

[58] M. B. Walker and M. F. Smith. *Phys. Rev. B*, 61:11285, 2000.

[59] C. C. Homes, T. Timusk, D. A. Bonn, Ruixing. Liang, and W. N. Hardy. *Physica C*, 254:265, 1995.

[60] L. Forro, V. Ilakovac, J.R. Cooper, C. Ayache, and J.Y. Henry. *Phys. Rev. B*, 46:6626, 1992.

[61] L. B. Ioffe and A. J. Millis. *Phys. Rev. B.*, 58:11631, 1998.

[62] K. A. Moler, J. R. Kirtley, D. G. Hinks, T. W. Li, and Ming Xu. *Science*, 279:1193, 1998.

[63] J. R. Kirtley, K. A. Moler, G. Villard, and A. Maignan. *Phys. Rev. Lett.*, 81:2140, 1998.

[64] T. A. Friedmann, M. W. Rabin, J. Giapintzakis, J. P. Rice, and D. M. Ginsberg. *Phys. Rev. B*, 42:6217, 1990.

[65] D. A. Bonn et al. In *Proceedings of the 21st International Conference on Low Temperature Physics.* Czechoslovak Journal of Physics, 1996.

[66] W.N. Hardy, Saeid Kamal, Ruixing Liang, D. A. Bonn, C. C. Homes, D. N. Basov, and T. Timisk. Microwave measurements of the penetration depth in htsc single crystals. In B. Batlogg, C. W. Chu, W. K. Chu, D. U. Gubser, and K. A. Muller, editors, *Proceedings of the 10th Anniversary HTS Workshop.* World Scientific, 1996.

[67] Ruixing Liang. *Physica C*, 195:51, 1992.

[68] A. Hosseini, Saeid Kamal, D.A. Bonn, Ruixing Liang, and W.N. Hardy. *Phys. Rev. Lett.*, 81:1298, 1998.

[69] R. J. Radtke, V. N. Kostur, and K. Levin. *Phys. Rev. B*, 53:522, 1996.

[70] T. Xiang and J. M. Wheatley. *Phys. Rev. Lett*, 76:134, 1996.

[71] T. Jacobs, S. Sridhar, Qiang Li, G.D. Gu, and N. Koshizuka. *Phys. Rev. Lett.*, 75:4516, 1995.

[72] C. Panagopoulos, J. R. Cooper, G. B. Peacock, I. Gameson, P. P. Edwards, W. Schmidbauer, and J. W. Hodby. *Phys. Rev. B*, 53:R2999, 1996.

[73] J. A. Osborn. *Phys. Rev.*, 67:351, 1945.

[74] T. Xiang and J. M. Wheatley. *Phys. Rev. Lett*, 77:4632, 1996.

[75] T. Xiang, C. Panagopoulos, and J. R. Cooper. *INT J MOD PHYS B*, 12(10):1007, 1998.

[76] David Broun. *The microwave electrodynamics of unconventional superconductors.* PhD thesis, University of Cambridge, 2000.

[77] C. Panagopoulos, J. R. Cooper, T. Xiang, G. B. Peacock, I. Gameson, and P. P. Edwards. *Phys. Rev. Lett*, 79:2320, 1997.

[78] H. Kitano, T. Hanaguri, and A. Maeda. *Phys. Rev. B*, 57(17):10946, 1998.

[79] D. Dulic, D. van der Marel, A. A. Tsvetkov, W. N. Hardy, Z. F. Ren, J. H. Wang, and B. A. Willemsen. *Phys. Rev. B*, 60:R15051, 1999.

[80] D VanDerMarel. *Phys. Rev. B.*, 60:R765, 1999.

[81] T. Xiang and W. N. Hardy. *Phys. Rev. B*, 63:024506, 2000.

[82] D. J. Werder, C. H. Chen, R. J. Cava, and B. Batlogg. *Phys. Rev. B*, 38:5130, 1988.

[83] Ruixing Liang, D. A. Bonn, W. N. Hardy, Janice C. Wynn, K. A. Moler, L. Lu, S. Larochelle, L. Zhou, M. Greven, L. Lurio, and S. G. J. Mochrie. *cond-mat/0111379*, 2002.

[84] Schon J. H, Kloc C, Hwang H. Y, and Batlogg B. *Science*, 292:252, 2001.

[85] J. C. Wynn, D. A. Bonn, B. W. Gardner, Y. J. Lin, R. Liang, W. N. Hardy, J. R. Kirtley, and K. A. Moler. *Phys. Rev. Lett*, 87:197002, 2001.

[86] Y. J. Uemura, G. M. Luke, B. J. Sternlieb, J. H. Brewer, J. F. Carolan, W. N. Hardy, R. Kadono, J. R. Kempton, R. F. Kiefl, S. R. Kreitzman, P. Mulhern, T. M. Riseman, D. Ll. Williams, B. X. Yang, S. Uchida, H. Takagi, J. Gopalakrishnan, A. W. Sleight, M. A. Subramanian, C. L. Chien, M. Z. Cieplak, Gang

Xiao, V. Y. Lee, B. W. Statt, C. E. Stronach, W. J. Kossler, and X. H. Yu. *Phys. Rev. Lett.*, 62:2319, 1989.

[87] Tobias Jacobs. *Hochfrequenzeigenschaften geschichteter Supraleiter.* PhD thesis, Northeastern University, 1996.

[88] SK. A. Waldron. *Theory of Guided Electromagnetic Waves.* Van Norsrand Reinhold Company, 1970.

Appendix A

Cavity Perturbation approximation

The cavity perturbation result which forms the basis of all the measurements described in this thesis will be derived here. We will restrict the discussion to the main ideas[1].

The cavity perturbation approximation assumes that we can describe the field configuration of a cavity oscillating in one of its normal modes by

$$\vec{H}(\vec{r},t) = \vec{H}_0(\vec{r})e^{i\omega_0 t}, \vec{E}(\vec{r},t) = \vec{E}_0(\vec{r})e^{i\omega_0 t} \tag{A.1}$$

where $\vec{H}_0(\vec{r})$ and $\vec{E}_0(\vec{r})$ are the maximum field strengths at the position $\vec{r}$ in the cavity and ω_0 is the unperturbed resonance frequency. We will also take the cavity to be ideal so that it's walls have zero surface impedance. This has no effect on the outcome of the result, and we will come back to the real cavity case at the end.

By loading the sample into the resonator, we can assume that the new field configuration is the sum of the unperturbed fields, $\vec{H}_0$, $\vec{E}_0$, and the additional fields $\vec{H}_1$, $\vec{E}_1$, while allowing a complex change in frequency $\delta\tilde{\omega}$.

$$\vec{H} = (\vec{H}_0 + \vec{H}_1)e^{i(\omega_0+\delta\tilde{\omega})t}, \vec{E} = (\vec{E}_0 + \vec{E}_1)e^{i(\omega_0+\delta\tilde{\omega})t} \tag{A.2}$$

The fields outside the perturbed volume are $\vec{B} = \mu_0\vec{H}$ and $\vec{D} = \epsilon_0\vec{E}$ like for the unloaded cavity. Maxwell's equations can be written as,

$$\nabla \times \vec{H}_0 = i\omega\vec{D}_0, \nabla \times \vec{E}_0 = -i\omega\vec{B}_0 \tag{A.3}$$

$$\nabla \times (\vec{H}_0 + \vec{H}_1) = i(\omega + \delta\tilde{\omega})(\vec{D}_0 + \vec{D}_1)$$

$$\nabla \times (\vec{E}_0 + \vec{E}_1) = -i(\omega_0 + \delta\tilde{\omega})(\vec{B}_0 + \vec{B}_1)$$

[1]The derivation here follows that given in several theses and details can be found in these works [76, 87]

These relations can be manipulated into the form below by using vector identities,

$$i\omega[\vec{E}_0 \cdot \vec{D}_1 - \vec{E}_1 \cdot \vec{D}_0 + \vec{H}_1 \cdot \vec{B}_0 - \vec{H}_0 \cdot \vec{B}_1] + \nabla \cdot (\vec{E}_0 \times \vec{H}_1 + \vec{H}_0 \times \vec{E}_1) \qquad (A.4)$$
$$= -i\delta\tilde{\omega}[\vec{E}_0 \cdot \vec{D}_o - \vec{H}_0 \cdot \vec{B}_0 + \vec{E}_0 \cdot \vec{D}_1 - \vec{H}_0 \cdot \vec{B}_1]$$

the point being that we can integrate this expression over the volume $V_c - V_s$, where V_c, and V_s are the volumes of the cavity and sample respectively. The first four terms in square brackets cancel if we assume that the field distribution has not changed appreciably in the volume outside the sample, and that the perturbed H and E are still in quadrature. This yields for the complex frequency shift,

$$\delta\tilde{\omega} = \frac{-i \oint_s (\vec{E}_0 \times \vec{H}_1 + \vec{H}_0 \times \vec{E}_1) \cdot (-\hat{n}) dS}{\int_{V_c - V_s} (\vec{E}_0 \cdot \vec{D}_o - \vec{H}_0 \cdot \vec{B}_0 + \vec{E}_0 \cdot \vec{D}_1 - \vec{H}_0 \cdot \vec{B}_1) dV} \qquad (A.5)$$

The denominator of A.5 is identified as $4\langle U \rangle$, where $\langle U \rangle$ is the energy stored in the field volume. To simplify the numerator we will use the fact that our sample sits in an electric field node of a TE_{011} cavity and we can take $E_0 \approx 0$. The quantity $(\vec{E}_1 \times \vec{H}_0)$ is twice the poynting vector,$\vec{p}$, and the definition of the cavity quality factor is 2π times the ratio of the time averaged energy stored in the cavity to the energy loss per cycle. i.e $Q = \omega\langle U \rangle / \Re\langle P \rangle$. The time averaged poynting vector and the complex power flow into the sample are given by:

$$\langle \vec{p}(t) \rangle = \langle (\vec{E}(t) \times \vec{H}(t) \rangle = \frac{1}{2} \vec{E}_1 \times \vec{H}_{\parallel} \qquad (A.6)$$
$$\langle P \rangle = \oint \langle \vec{p} \rangle \cdot (-\hat{n}) dS$$

where $H_{\parallel}$ is the maximum field in one period of oscillation parallel to the surface. The surface impedance is also defined from Eq. 2.2, to be related to this complex power flow via $Z_s = 2\langle P \rangle / (H_{\parallel}^2 A)$, leading to the result,

$$\delta\tilde{\omega} = \frac{i Z_s H_{\parallel}^2 A}{4\langle U \rangle} = \delta\omega + i\frac{\omega_0}{2Q} \qquad (A.7)$$

where A is the area of the sample, Q is the quality factor of the ideal cavity with a sample, and $\Delta\omega$ is the shift in the center frequency after the sample is loaded. The surface impedance can be written in the more familiar form

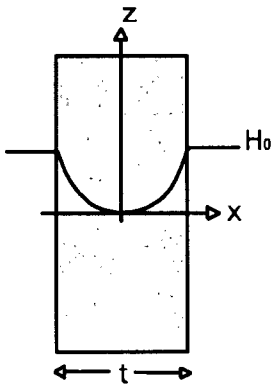

Figure A.1: Field decay inside a thin sample.

$$Z_s = \Gamma\,(1/Q - 2i\delta\omega/\omega_0) \tag{A.8}$$

where $\Gamma = \frac{2\omega_0\langle U\rangle}{H_{\parallel}^2 A}$, is the calibration constant that is usually found experimentally using a Pb-Sn calibration sample. In the derivation we have assumed that the cavity is ideal with zero surface impedance. However the treatment can be done in the same way to make the perturbation be that of the finite conductivity of the walls instead of a sample. This leads to a similar expression which represents the surface impedance of the walls, as shifts relative to the ideal cavity. In practice we are only after the perturbation by the sample and its surface impedance is measured relative to the non-ideal cavity which has base quality factor Q_U, and center frequency $\omega_U \approx \omega_0$. The quantities $1/Q$ and $\delta\omega$ in A.8 have to be replaced with $1/Q_L - 1/Q_U$ and $\omega_L - \omega_U$.

A.1 Finite size electrodynamic model in the TE_{011} cylindrical cavity

Equation A.5 can be explicitly calculated for the TE_{011} mode of the cylindrical cavity (radius a and height l), with a sample (area A, thickness t) placed at its centre. The numerator of the expression is the important quantity which has to be calculated,

and done so by using the divergence theorem to get a volume integral over the sample volume. Eq. A.5 can then be written as

$$\delta\tilde{\omega} = \frac{\omega \int_{V_s}(\vec{H}_1 \cdot \vec{B}_0)dV}{4\langle U\rangle} \tag{A.9}$$

We will take the applied field to be constant just outside the sample, with magnitude H_0 and inside the magnetic field strength is $H_0 + H_1$ which decays with a characteristic length $1/\Re[\gamma]$, where γ is the propagation constant of the material ($\gamma = \sqrt{i\mu_o\omega\sigma}$). It is easy to show the following form, $H_0 + H_1 = \frac{H_0\cosh(\gamma x)}{\cosh(\gamma t/2)}$. This can be used to integrate $\vec{H}_1 \cdot \vec{B}_0$, with the final result,

$$\frac{\delta\tilde{\omega}}{\omega_0} = \frac{\mu_0 H_0^2 V_s}{4\langle U\rangle}\left[1 - \frac{\tanh(\gamma t/2)}{\gamma t/2}\right] \tag{A.10}$$

The energy stored in this mode has been found by R. A. Waldron [88] as

$$\langle U\rangle = \frac{\mu_0}{4z} H_0^2 V_c \tag{A.11}$$

where $z^{-1} = J_0^2(\chi_{01}^{'})\left[1 + \left(\frac{\pi a}{\chi_{01}^{'} l}\right)^2\right]$, and $\chi_{01}^{'} = 3.8317$, is the first root of $J_0^{'}$.

Together with A.10 this yields a simple relation

$$\frac{\delta f}{f} + \frac{i}{2}\delta(\frac{1}{Q}) = \frac{zV_s}{V_c}\left[1 - \frac{\tanh(\gamma t/2)}{\gamma t/2}\right] \tag{A.12}$$

between the cavity response and the propagation constant γ which is used to get the surface impedance.